Title	Dust in the centres of galaxies : observations and modelling of dust in the nucleus of NGC1068 and in the galactic centre
Author	Mason, Rachel
Qualification	PhD
Year	2003

Dust in the Centres of Galaxies: Observations and Modelling of Dust in the Nucleus of NGC1068 and in the Galactic Centre.

RACHEL MASON

Institute for Astronomy

School of Physics

A thesis submitted to the University of Edinburgh

for the degree of Doctor of Philosophy

2003

Declaration

I hereby declare that this thesis entitled *Dust in the Centres of Galaxies: Observations and Modelling of Dust in the Nucleus of NGC1068 and in the Galactic Centre* is not substantially the same as any that I have submitted for a degree or diploma or other qualification at any other University. I further state that no part of my thesis has already been or is being concurrently submitted for any such degree, diploma or other qualification.

This thesis is the outcome of my own work except where specifically indicated in the text.

Rachel Mason
Edinburgh,
August 2003.

Acknowledgments

Thanks to Gillian Wright, Peter Brand, Andy Adamson and Yvonne Pendleton, for getting me started and keeping me right. I would never have got this far without moral and financial support from my family — Mum, Dad, Ossie and Jackie, stand up and take a bow. Thanks also to the students at the ROE and my friends from The Outside, for alternately driving me mad and keeping me sane (you know who did what). And thankyou Matt, for understanding.

Abstract

As the "archetypal" Seyfert II galaxy, NGC1068 is one of the best-studied dusty objects in the sky. Yet — in common with Seyfert galaxies in general — the properties of its dust are not at all well-known. To remedy this situation I have modelled the IR polarisation and 3.4μm dust absorption feature observed in the nucleus of NGC1068 and compared the results with new and existing spectroscopy and polarimetry. I find that to reproduce the observed polarisation, the aligned dust grains in this AGN must be larger than those seen in the Galactic diffuse ISM and molecular clouds. I am also led to conclude that the polarising grains in NGC1068 do not take the form of silicate cores with organic mantles, a model which has been widely used to describe dust in the diffuse ISM of our Galaxy. The organic fraction of the dust instead exists as some form of small, nonpolarising grain, and its 3.4μm feature shows that it is chemically very similar to carbonaceous dust in other, very different environments. The interpretation of this is not yet clear, but it is consistent with a common formation site and mechanism for the carrier of the band seen in many environments, which is then resistant to processing in the ISM. I have also applied these models to a Galactic centre line of sight, again finding that the core-mantle dust grain model is unlikely to be a valid representation of this dust.

Contents

1 Introduction 1

1.1 Dust and the interstellar medium . . . 2

1.2 Models of interstellar dust . . . 5

1.2.1 Separate population models . . . 8

1.2.2 Porous aggregates . . . 9

1.2.3 Biological organisms . . . 10

1.2.4 Core-mantle models . . . 11

1.3 Dust in other galaxies . . . 12

1.4 The carbonaceous component of dust . . . 17

2 Spectropolarimetry of NGC1068 21

2.1 Spectropolarimetry and the core-mantle dust model . . . 21

2.2 NGC1068 . . . 25

2.3 Polarised light . . . 28

2.3.1 The Stokes parameters 30
2.4 The L-band polarisation of NGC1068 31
2.4.1 Dual-beam polarimetry: CGS4+IRPOL2 31
2.4.2 Observations and data reduction 34
2.4.3 Constructing the polarisation spectrum of NGC1068 37
2.4.4 The position angle of polarisation of NGC1068 44
2.4.5 Comparisons with existing observations 46
2.5 The N-band polarisation of NGC1068 46
2.5.1 Single-beam polarimetry: Michelle 46
2.5.2 Observations and data reduction 47
2.5.3 The N-band polarisation of NGC1068 50
2.5.4 Comparisons with existing observations 56
2.6 Flux and optical depth spectra of NGC1068 57
2.6.1 CGS4+IRPOL L-band spectrum 57
2.6.2 UIST L-band spectrum 58
2.6.3 The N-band flux spectrum of NGC1068 62
2.6.4 Comparisons with existing observations 65

3 Modelling Extinction and Polarisation 67

3.1 The near-IR polarisation of NGC1068 68

3.2 Calculating extinction and polarisation 76

3.2.1 The Discrete Dipole Approximation 76

3.2.2 Applicability and use of DDSCAT5a.10 78

3.3 Parameters describing the dust grains 83

3.3.1 Optical constants 83

3.3.2 Grain shape 86

3.3.3 Size distribution of the cores and mantles 87

3.3.4 Grain alignment 89

3.4 First steps: testing DDSCAT 91

3.5 Polarisation and extinction of dust grain ensembles 94

3.5.1 Standard "Galactic" size distributions 95

3.5.2 Changing grain size 98

4 The Aligned Grains in NGC1068 and GCIRS 7 101

4.1 The size of the polarising grains in NGC1068 102

4.1.1 Useful data 102

4.1.2 Sizes appropriate to the Galactic diffuse ISM 104

4.1.3 Larger grains 106

4.2 The structure of the grains in NGC1068 110

4.2.1 3-4μm polarisation of larger grains 111

4.2.2 Constraints from column densities 112

4.2.3 Large grains and the 3.4μm feature 113

4.3 Aliphatic hydrocarbons in NGC1068 116

4.3.1 The contribution of the carrier of the 3.4μm band to the extinction . . . 116

4.3.2 Comparisons with the 3.4μm band in other environments 117

4.4 Silicates in NGC1068 122

4.5 GCIRS 7 revisited 124

5 Conclusions 127

5.1 Grain growth in NGC1068 128

5.2 Suggestions for future work 129

5.2.1 Large grains, small grains and the extinction curve 129

5.2.2 The 3.4μm band in other galaxies 131

5.2.3 Further tests of the core-mantle dust model 132

5.3 Summary 133

List of Figures

1.1 Schematic drawing of the phases of the interstellar medium. 3

1.2 Some of the key events in the lifecycle of dust and the ISM. 5

1.3 Cartoon of an AGN according to the unification hypothesis. 13

1.4 Orbital hybridisation. 18

2.1 The central few arcseconds of NGC1068 26

2.2 The polarisation ellipse for right-handed elliptical light. 29

2.3 Steps in the reduction of the L-band polarimetry data of NGC1068 36

2.4 Instrumental absorption and waveplate ripple 38

2.5 Steps in the removal of the instrumental polarisation 39

2.6 The effect on the polarisation of NGC1068 of using different fits to the instrumental polarisation. 40

2.7 The L-band polarisation spectrum of NGC1068. 43

2.8 The position angle of polarisation of NGC1068. 45

2.9 Choosing which N-band data to keep/reject. 50

2.10 Raw N-band polarisation spectra of NGC1068, Rigel and the BN object. 51

2.11 Correcting the N-band polarisation spectrum for instrumental polarisation. . . . 52

2.12 NGC1068's N-band polarisation spectrum after correction for statistical bias. . 53

2.13 The N-band position angle spectra of NGC1068, Rigel and the BN object. . . . 54

2.14 The position angle of NGC1068, calibrated with reference to the BN object. . . 55

2.15 Flux spectrum of NGC1068 showing the fitted continuum and the good cancellation of the atmospheric absorption lines. 59

2.16 UIST flux and optical depth spectra of the 3.4μm band, taken without IRPOL in the beam. 61

2.17 Comparison of optical depth spectra of the 3.4μm feature in NGC1068 as obtained by CGS4+IRPOL and UIST. 63

2.18 N-band flux and optical depth spectra of NGC1068. 64

3.1 Angular scattering and scattering vs absorption efficiencies for spheres small compared with the wavelength. 69

3.2 The percentage polarisation and position angle of polarisation of NGC1068, from the UV to the IR. 70

3.3 The 1-5μm polarisation of NGC1068, corrected for dilution by unpolarised starlight. 74

3.4 A sample DDSCAT input file. 80

3.5 Description of target orientation in DDSCAT. 82

3.6 Optical constants for astronomical silicate and Li and Greenberg's organic material. 85

3.7 Orientation of a 2:1:1 prolate and a 2:2:1 oblate spheroid in the perfect spinning alignment approximation. 92

3.8 Tests of DDSCAT. 93

3.9 Polarisation calculated for models using "standard" Galactic parameters. 96

3.10 The effect of grain size on polarisation. 100

4.1 NGC1068 and polarisation from Galactic dust size distributions. 104

4.2 Polarisation from size distributions which predict the correct slope through the L-band spectropolarimetry of NGC1068. 107

4.3 Number of grains vs grain radius for the size distributions considered in this chapter. 109

4.4 Polarisation from small separate silicate and carbonaceous dust grains 110

4.5 The observed and calculated 3-4μm polarisation of NGC1068. 112

4.6 The 3.4μm feature of larger grains. 114

4.7 Extinction efficiencies of various sizes of core-mantle grains. 115

4.8 Comparison of the 3.4μm feature in NGC1068 with that observed in GCIRS 6E and GCIRS 7. 119

4.9 Comparison of the 3.4μm feature in NGC1068 with that observed in IRAS08572 and CRL618. 120

5.1 Comparison of extinction cross-sections calculated for grains in different environments. 131

List of Tables

2.1 Comparison of some properties of the circumnuclear environment of NGC1068 with two Galactic environments. 27

2.2 The 10μm polarisation of NGC1068. 56

3.1 Percentage of the light from NGC1068 which comes from a nonstellar source. . 73

3.2 Values of the size parameters used by L&G in fitting polarisation and extinction data, and mantle volume fractions which have been suggested to apply to core-mantle grains. 95

4.1 The values of the size parameters characterising the grain size distributions investigated in this chapter. 106

CHAPTER 1

Introduction

> *Let me say at first, rather naïvely, how struck I am by the delicate symbiosis that exists between the stars and the interstellar medium, how each is nourished by the other, and how the Galaxy as we know it is entirely a consequence of that balance and interplay. It is interesting to speculate how, if one were able to tinker with just one parameter of this beautiful machinery, the whole ecosystem . . . might find a new balance point and become unrecognisable to us.*
>
> Herbig 1977

Despite making up only around 1% of the mass of the interstellar medium of a typical spiral galaxy, interstellar dust can contribute as much as 50% of its total luminosity, by absorbing ultraviolet and visible radiation and reradiating it in the infrared (Popescu and Tuffs, 2002). This phenomenon is by no means confined to the local universe; large masses of dust are observed in quasars at $z > 4$ (Omont et al., 2001; Priddey and McMahon, 2001). In addition to simply being widespread, dust is known to have a profound effect on light passing through it. For instance, visible light leaving the Galactic centre experiences about 30 magnitudes of dimming before arriving at the Earth (Glass, 1999): most of this is due to dust. Add to all this the fact that extinction by dust is strongly wavelength-dependent, and it is clear that some understanding of dust is vital if astronomical observations are to be interpreted correctly.

The effect of dust on our observations is only the beginning of the story, however. Over the years it has become clear that dust has an important rôle to play in its own right. For instance, molecules such as H_2, CH_4 and CH_3OH can be plentiful in the interstellar medium, yet at such low temperatures and densities the gas phase reactions leading to their production are hopelessly inefficient. The surfaces of dust grains can catalyse these reactions, vastly increasing the rate of reaction and explaining the observed abundance of these molecules. And dust grains and the molecules whose formation they catalyse are crucial regulators of star formation.

Although we are by no means short of observations of dust, and laboratory measurements of candidate materials, there remains some uncertainty in the details of what dust is actually composed of. The relationship between the various classes of material known to exist in dust grains is a particular problem, and much of this thesis has been aimed at addressing that issue.

The structure and composition of dust is a consequence of the environments in which it has existed. It is a clue to the whole lifecycle of interstellar material, from its birth in evolved stars and supernovae to its incorporation in a new generation of stellar systems. A key question is, then, does this lifecycle differ from galaxy to galaxy? Under the extreme conditions of, say, an active galactic nucleus, what resemblance does the dust bear to that in our own galaxy? Whilst much work has been done on the properties of dust in our galaxy, extragalactic dust has not been widely investigated. A second subject dealt with in this thesis, then, is the nature of the dust grains in nearby galaxies, with particular reference to the dust surrounding the supermassive black hole thought to lurk in the centre of the Seyfert II galaxy, NGC1068.

1.1 Dust and the interstellar medium

It is now over 150 years since Wilhelm Struve first controversially proposed that starlight is absorbed by interstellar matter, and more than 70 since R. J. Trumpler's work confirming this hypothesis (Struve, 1847; Trumpler, 1930). Further studies on the reddening of stars showed that the absorption is due to solid particles with a size comparable to the wavelength of light: interstellar dust. The dust grains are well mixed with the gas which permeates the Galaxy, but we now know that interstellar extinction is considerably more complicated than the simple

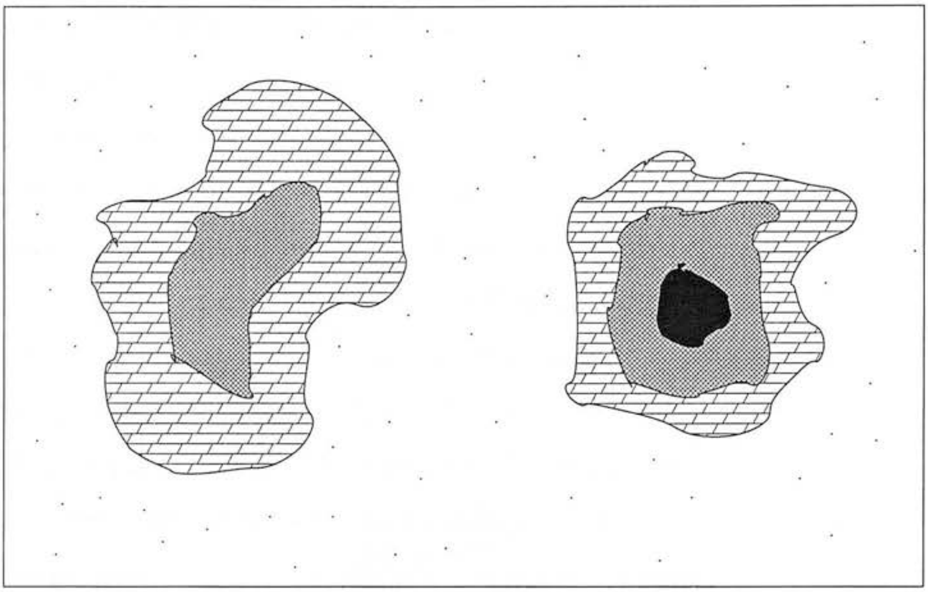

Figure 1.1: Schematic drawing of the phases of the interstellar medium. The darkest area of the dense molecular cloud (right) represents cold molecular material which is surrounded in turn by cool atomic and warm, partially ionised gas. The diffuse cloud (left) lacks a cold molecular core. The clouds are bathed in the hot, tenuous intercloud medium; gas and dust are well-mixed throughout. Adapted from Whittet (1992).

uniform absorption envisaged by some of the early researchers. We can now classify the interstellar medium (ISM) into a number of distinct regions with characteristic properties (Fig. 1.1).

The popular idea that space is a vacuum is not quite correct, but it is a fair approximation. Hot, ionised, and with an HII number density of only around 10^4 ions m^{-3}, a sprinkling of tenuous gas and dust takes up the bulk of the volume of the Galaxy. As far as mass is concerned, though, this material, the intercloud medium, counts for very little. Cooler, denser regions exist in which the gas is only partially ionised, and contained within these warm areas can be cool atomic clouds a few parsecs across. In the intercloud medium and partially-ionised areas the gas is bathed in the light from all the stars in the Galaxy (the interstellar radiation field or ISRF), which is energetic enough to dissociate any H_2 molecules which may form. The higher density of cool atomic clouds, $10^7 - 10^9$ atoms m^{-3}, means that dust grains more effectively shield the gas. The temperature drops to $\sim$ 100K and conditions in the cool atomic clouds may be suitable for the formation of a few polyatomic molecules. Together, the warm, partially ionised and cool, atomic regions in the intercloud medium make up the diffuse clouds of the ISM.

The temperature of clouds in the ISM is regulated by the balance between heating by cosmic rays and the ISRF, and cooling by line and continuum emission from atoms, ions, molecules and dust. As the cooling molecular transitions are mostly collisionally excited, increasing the density of gas increases its cooling rate, causing it to drop in temperature and pressure, and leading to its becoming yet cooler and denser. This phenomenon explains the presence of a cold molecular phase in the ISM ($10^9 - 10^{10}$ molecules m^{-3}). In these clouds the dust density is high enough that little starlight penetrates and complex molecules can form. Over 100 different molecules have now been detected in the ISM, representing many of the basic organic functional groups (acids, alcohols, aldehydes, ketones... see Ehrenfreund and Charnley, 2000 for a review). Some of these molecules may be the precursors of the amino acids which are brought to Earth in meteorites. The low temperature, $\sim$ 10K, means that the dust grains in these cold molecular clouds acquire mantles composed of ices of some of these volatile molecules. Dense molecular clouds can grow up to tens of parsecs across and contain $\sim 10^6 M_\odot$ of material.

The various components of the ISM are by no means static; in fact they are constantly changing (Fig. 1.2). The medium is enriched by evolved stars, ripped apart by supernovae, and dispersed by the winds from the new stars which form in the heart of the densest regions. In the scenario proposed by Greenberg (1984), for instance, a dust grain will cycle between dense and diffuse clouds something like 50 times in its lifetime, evolving all the time.

Just as the state of the gas differs between dense and diffuse clouds, there is ample evidence that dust properties also vary. For example, it is generally accepted that dense cloud dust grains possess icy mantles — the enhanced depletion of elements such as C, N, and O from the gas phase in molecular clouds is accompanied by the appearance of ice spectral signatures (Whittet et al., 1989). A particularly contentious issue, though, is what happens to these coatings when the dust moves from dense to diffuse clouds, in particular whether they are processed into mantles of a new organic[1] material. This question forms part of the subject of this thesis, and I shall also be examining the nature of some extragalactic dust using an absorption line which, in the Galaxy, is observed in the diffuse ISM. For this reason the following discussion applies (except where otherwise stated) to dust in diffuse rather than dense molecular clouds.

---

[1] In this thesis I use the strict chemical definition of "organic" material as any (covalently-bonded) substance containing carbon. It should not be taken to imply any biological connection.

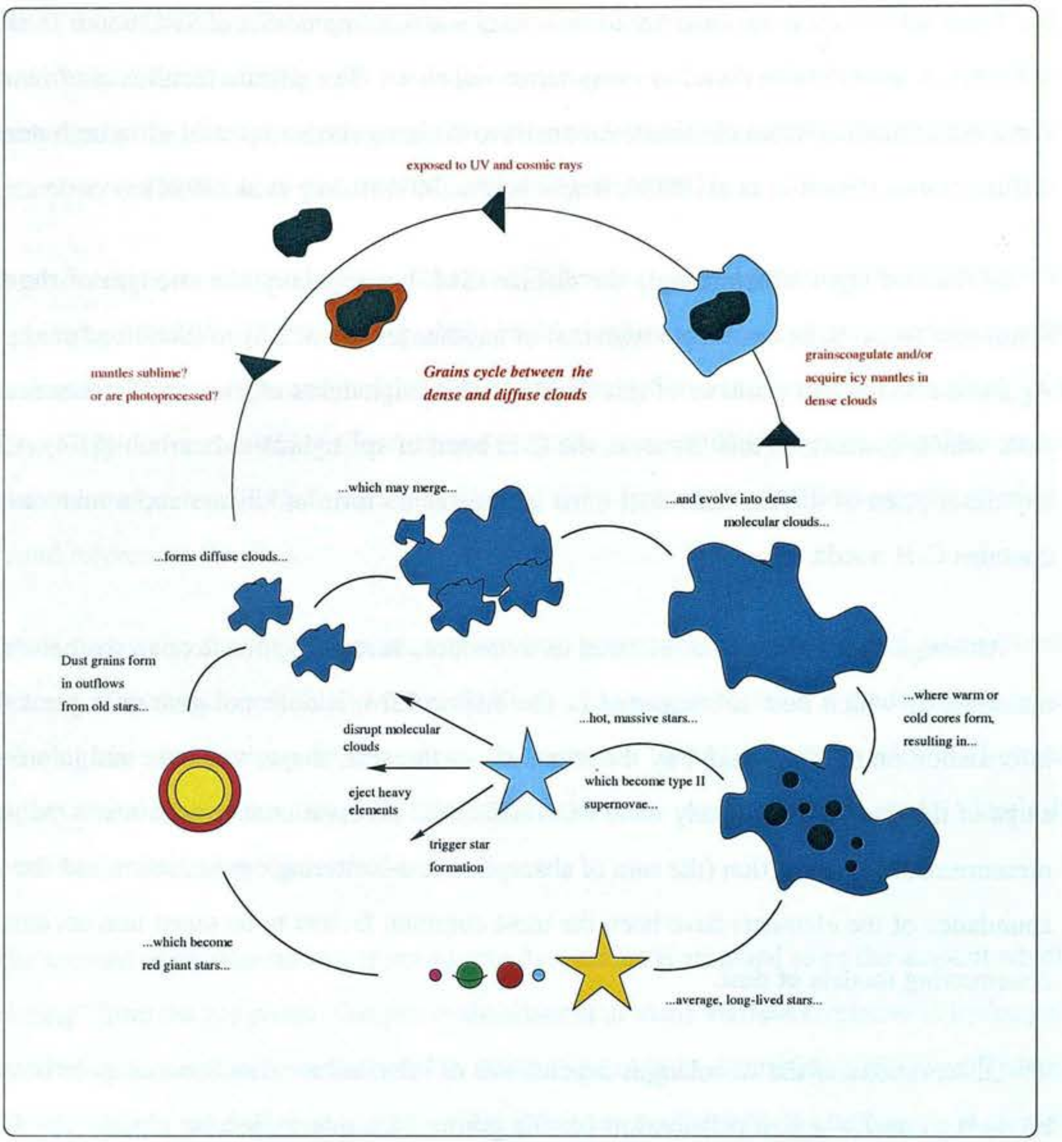

Figure 1.2: Some of the key events in the lifecycle of dust and the ISM.

1.2 Models of interstellar dust

Spectroscopic observations have gone some way towards establishing the composition of diffuse interstellar dust. When viewing a source which is sufficiently distant, lines appear in the spectrum due to transitions between vibrational energy levels of the chemical bonds in the dust along the line of sight. One of the most widespread features is a broad band seen in absorption or emission at 9.7μm, accompanied by a weaker feature at 18.5μm (Simon and Dyck, 1975; Roche and Aitken, 1985; Roche et al., 1991). The wavelengths and relative strengths of these two lines indicates that they are due to stretching and bending modes of Si-O bonds in silicates, not entirely unlike those found in many terrestrial rocks. The silicate features are found in diverse environments, from circumstellar shells to distant galaxies, as well as in both dense and diffuse clouds (Guertler et al., 1989; Roche et al., 1991; Bowey et al., 1998).

In lines of sight which sample the diffuse ISM in our galaxy, the strength of the silicate features is found to be correlated with that of another feature at 3.4μm (Sandford et al., 1995). Again, the shape and position of this band are clear signatures of the specific chemical bond from which it arises; in this instance, the C-H bond of sp^3 hybridised carbon (§1.4). Clearly, any description of diffuse ISM dust must include some form of silicate and a material which contains C-H bonds.

Although spectroscopy has allowed us to deduce, at least to some extent, the nature of the materials of which dust is composed in the diffuse ISM, it does not give us a great deal of information on the form taken by the materials — the size, shape, structure and interrelationships of the grains. Fortunately there exist additional observational constraints. Traditionally, measurements of extinction (the sum of absorption and scattering), polarisation and the cosmic abundance of the elements have been the most common factors to be taken into account when constructing models of dust.

Observations of the wavelength dependence of interstellar extinction and polarisation can be used to derive a size distribution for the grains. Outside molecular clouds, the Galactic extinction curve is fairly constant over many different lines of sight, and can be roughly divided into three parts (Savage and Mathis, 1979). At visible wavelengths the extinction A_V goes approximately as λ^{-1}. The λ^{-1} dependence of A_V mimics the behaviour of weakly-absorbing particles smaller than the wavelength of visible light, where absorption dominates over scattering and is also proportional to λ^{-1}. This is the basis for the belief that a population of submicron-sized grains exists in the ISM (often confusingly known as the "large" or "classical" grain population). Observations of interstellar polarisation also support this view.

At much shorter wavelengths, the curve is characterised by a sharp rise into the far-UV. The submicron-sized particles responsible for the visible extinction would not absorb very efficiently at UV wavelengths, so it seems that much smaller grains are also present. At the very small end of the size distribution, some form of particle made up of only around 50 atoms seems to exist. Such small grains (or large molecules) can be briefly heated to very high temperatures by the absorption of a single photon, which would explain the family of emission features observed in the near- and mid-infrared (Sellgren, 1984).

Sandwiched between the visible and the far-UV lies a broad and prominent extinction peak, centred at about 2175Å. What kind of particle could give rise to such a symmetric feature with constant central wavelength and lack of associated absorption bands remains something of a mystery. Graphite or something like it seems to be the least unlikely carrier; other interpretations include polyaromatic hydrocarbons, C_{60} and OH^- ions on small silicate grains (Draine, 1989, and references therein).

While fitting the above parameters, any realistic grain model must also take into account the amount of material available to form the dust. However successful a model might be at reproducing the observations, if it requires, for instance, 200 C atoms per million H atoms (200ppM) when there exists, say, only 100ppM in the solid phase, then that model clearly is not a valid representation of interstellar dust.

The amount of an element incorporated into dust grains is assumed to be the amount which is "missing" from the gas phase. Gas phase abundances of many elements, relative to hydrogen, can now be quite accurately measured, but difficulties arise in determining the overall abundances from which the depletions into the solid phase can be deduced. As both gas and dust go to form new generations of stars, then in principle the relative abundances of the elements in a star should reflect the total cosmic abundances.

The obvious star to use for this purpose is the Sun, which has better-defined abundances than more distant stars. Unfortunately, the Sun is about 4.5Gyr old, so there has been plenty of time for nucleosynthesis to alter the amount of each element from its original value. The younger B stars seemed an interesting alternative (Gies and Lambert, 1992; Sofia et al., 1994; Snow and Witt, 1996), but their use lowered the abundance of carbon to a value, $\sim 2/3$ solar, which creates great difficulties for all existing dust models. Other studies (Cardelli, 1994; Cardelli et al., 1996) indicated similar low values for the interstellar abundances, but Sofia and Meyer (2001) now argue that if any star can act as a good analogue of the interstellar medium in this sense it is young F and G stars, which turn out to have approximately solar abundances. There is clearly considerable uncertainty about the cosmic abundance of the elements, but signs are emerging that the stringent constraints placed on dust models by the 2/3-solar abundances may be loosening.

Any dust model which can satisfy these demands is a plausible candidate. The composition and size distribution of the grains are limited to a certain extent by the astronomical data, but none of the observations discussed so far directly constrains their structure. Beyond the known correlation between the strengths of the silicate and hydrocarbon features, there is nothing to specify the relationship between the silicate and carbon-containing dust materials, for example. Consequently there is still a fair amount of room to manoeuvre when constructing dust models, and four distinct classes have emerged.

1.2.1 Separate population models

A number of authors have proposed dust models in which silicate and carbonaceous grains exist in separate (but mixed) populations. Draine and Lee (1984, hereafter D&L) have extensively reinvestigated the proposition by Mathis, Rumpl and Nordsieck (1977, "MRN") that dust is a mixture of graphite and silicate grains with an $a^{-3.5}$ distribution of sizes, from $a = 0.005\mu\mathrm{m}$ to $a = 0.25\mu\mathrm{m}$ (a is the grain radius). They find that this model gives an acceptable match to the extinction curve from the UV to the near-IR. It also correctly predicts the IRAS $100\mu\mathrm{m}$ fluxes for three out of four sources studied. Earlier, Mathis (1979) found that the silicate grains with $0.08\mu\mathrm{m} \lesssim a < a\,(max)$ in the model can reproduce the observed wavelength dependence of polarisation in the ISM.

The carbonaceous component of the MRN and D&L models is graphite, which obviously cannot be the whole story: graphite is a form of pure carbon and therefore does not contain the C-H bonds responsible for the observed absorption at $3.4\mu\mathrm{m}$. Nonetheless, this in itself does not invalidate the principle that the carbon- and silicon-containing grains in the model are separate from one another. The model must, however, deal with the problem of grain purity. Shocks in the ISM limit the lifetime of a silicate dust grain to $\sim 2 \times 10^8$ yrs but the stardust injection timescale is an order of magnitude longer (Seab, 1988; McKee, 1989; Jones et al., 1994). This implies that only $\sim 10\%$ of the heavy elements should be incorporated in dust grains, whereas in fact the observed depletions are more like 90%. It seems, then, that dust grains must quite rapidly form in the ISM, probably by condensing in molecular clouds and cycling back into the diffuse medium (Draine, 1990). Unfortunately it is then difficult to understand why the resulting grains are not simply a mixture of whatever types of atom happened to land on the growing grain in the molecular cloud.

1.2.2 Porous aggregates

The issue of grain purity is avoided by models in which the silicate and carbonaceous materials appear in the form of composite grains. Mathis (1996) considers the evidence for this type of dust. Particularly suggestive is the observation that R_V, the ratio of total to selective extinction, increases in dense clouds compared with diffuse clouds. This suggests that there are fewer small grains in dense clouds, and the relative efficiencies of grain-grain coagulation and accretion of atoms from the gas phase indicate that the small grains are depleted as the grains stick to one another. This means that not only will the grains be inhomogeneous aggregates, but that as it is difficult to see how the grains would fit perfectly together, they will also contain voids.

In the Mathis (1996) model, the relative amounts of various forms of carbon, silicates, trace elements and vacuum in the grains were allowed to vary, together with the mass distribution of the grains, until the resulting dust both reproduced the observed extinction curve (from 0.125 — 1.0μm) and was consistent with subsolar interstellar abundances. The visual albedo and A_V/N_H, the extinction per H atom, were also investigated.

Mathis speculates that the timescale for destruction of composite grains may be an order of magnitude longer than that for compact grains. Models of the ISM have some difficulty in explaining the rapid cycling of dust between dense and diffuse clouds, necessary if the short lifetime of dust grains means that they must quickly recondense in molecular clouds, so this is an attractive aspect of the model. However, Li & Greenberg (1997) raise the interesting issue of the tensile strength of aggregate grains. If aggregate grains are to polarise light, they must be aligned, and this alignment probably depends on the grains spinning with a high angular velocity (§3.3.4). Li & Greenberg's calculations show that grains with $a \geq 0.16\mu$m will be unable to withstand the strain induced by spinning, and will be blown apart. This will in turn affect the ability of the model to match the observed wavelength dependence of both extinction and polarisation.

1.2.3 Biological organisms

There also exists a very different kind of grain model, proposed by Hoyle and Wickramasinghe (1984,1999a). Partly inspired by the large and growing number of quite complex organic molecules known to be present in the ISM, the main components of this model are biological organisms, both whole and fragmented, and an additional population of inorganic dust particles. It is argued that the observed abundance of organic molecules cannot possibly be produced by non-biological means, and only the exponential growth characteristic of bacterial populations will suffice. The bacteria drift "freeze-dried" through interstellar space, then replicate when they come into the vicinity of a star, making use of the water and nutrients available in comets.

The model has some success in reproducing the interstellar extinction (based on an estimated refractive index for a dried bacterium, Wickramasinghe 1993). The 9.7μm feature can be reproduced by large organic molecules such as cellulose (in addition to the conventional silicates), and the small aromatic molecules thought to be responsible for the near-IR emission arise naturally from fragmentation of the bacteria.

Sadly, this exciting model has a number of grave flaws. For instance, Duley (1984) points out that terrestrial bacteria typically contain about the same number of carbon and oxygen atoms, and that DNA and RNA have about one phosphorus atom for every ten carbon atoms. For these ratios to hold in bacterial grains would require twice the observed interstellar oxygen abundance and 100 times the abundance of phosphorus. Hoyle and Wickramasinghe (1999b) counter that under certain conditions bacteria may contain much less RNA (and therefore less phosphorus) than usual. Another objection is that strong UV absorption features would also be expected, but are not observed (Whittet, 1992). Perhaps the most serious problem is the finding of Pendleton and Allamandola (2002) that the mid-IR bond stretches seen in the laboratory spectrum of the *e.Coli* bacterium and expected from any organism of such complexity are not observed in the diffuse ISM.

1.2.4 Core-mantle models

In the so-called core-mantle models of dust, submicron-sized grains composed of silicate cores with organic coatings are responsible for the visible and near-IR extinction and polarisation. To account for the far-UV extinction and the 2175Å bump, additional populations of small carbonaceous particles and a mixture of PAHs are also incorporated in the model. The coatings on the larger grains are supposed to arise from photochemical reactions in the icy grain mantles which are known to exist on dust in dense clouds. The most recent version (Li and Greenberg, 1997, hereafter L&G) fulfills many of the observational demands, including fitting the average polarisation and extinction curves and producing the correct ratio of polarisation to extinction. The authors claim that the model also comes closer to being within the elemental abundance constraints than other models.

Other points in favour of the core-mantle model include that experiments do indeed show that ices are processed into a form of organic residue on exposure to UV radiation and cosmic rays (Greenberg et al., 1995a). It is possible that the organic mantle may shield the silicate core from abrasion, thus alleviating the "destruction problem" (Jones et al., 1994). This model also naturally explains the observed correlation between the strength of the absorption features at 9.7 and 3.4μm (Sandford et al., 1995).

The case for core-mantle grains looks strong, but it is by no means closed. Some recent observations suggest that a key prediction of the model is not fulfilled. In the next chapter I will explain the reservations about the core-mantle dust model, and the spectropolarimetric technique which we have used to test it further.

1.3 Dust in other galaxies

Although the form of Galactic interstellar dust is still the subject of research, enough is known about it for the construction of plausible models. Dust in other galaxies is another matter entirely.

Dust certainly exists in other galaxies. Its presence is revealed in a number of ways, from the dust lanes clearly visible in optical images of spiral galaxies, to the massive infrared emission of the ultraluminous infrared galaxies (ULIRGs) discovered by the IRAS satellite in the early 1980s (Houck et al., 1984, 1985). Local examples of dusty galaxies include the classes of active galaxy known as Seyferts I and II, named after the original handful of galaxies noticed by Carl Seyfert in 1943 to have broad emission lines in their spectra (Seyfert, 1943). By the late 1970s it was becoming established that Seyfert galaxies are emitters of copious amounts of infrared radiation, and that this emission arises when dust grains absorb UV and visible radiation from a central source, reradiating it in the IR (Rieke, 1978). Because of their dusty nature and the fact that they are often bright — and quite numerous in the nearby universe — Seyfert galaxies are obvious candidates for the study of dust in external galaxies.

The current prevailing view of active galaxies holds that the type-I (possessing broad emission lines) and type-II (no broad emission lines) objects are essentially the same, but obscured in such a way that our classification of them depends on their orientation (see Antonucci, 1993 for a review). The principal components of this "unified model" (Fig. 1.3) include a central black hole and accretion disc, the powerhouse of the AGN (1), clouds of highly ionised material responsible for the broadest emission lines in the galaxy's spectrum (the broad line region or BLR, 2), and dust and gas in the form of a torus, obscuring the BLR from certain angles and allowing a direct view from others (3). The model also includes narrow line region (NLR) clouds which cause the narrower lines in the AGN spectrum (5), a scattering mirror of dust or free electrons (4) and, in some cases, a radio jet (6).

Whether or not the dust is really arranged neatly in a torus is still the subject of some debate (Cameron et al., 1993). What is accepted, though, is that large masses of dust and molecular gas exist within a few tens of parsecs of the nuclei of active galaxies. If, then,we observe a Seyfert II galaxy which is face-on to us, the dust we observe is essentially dust very

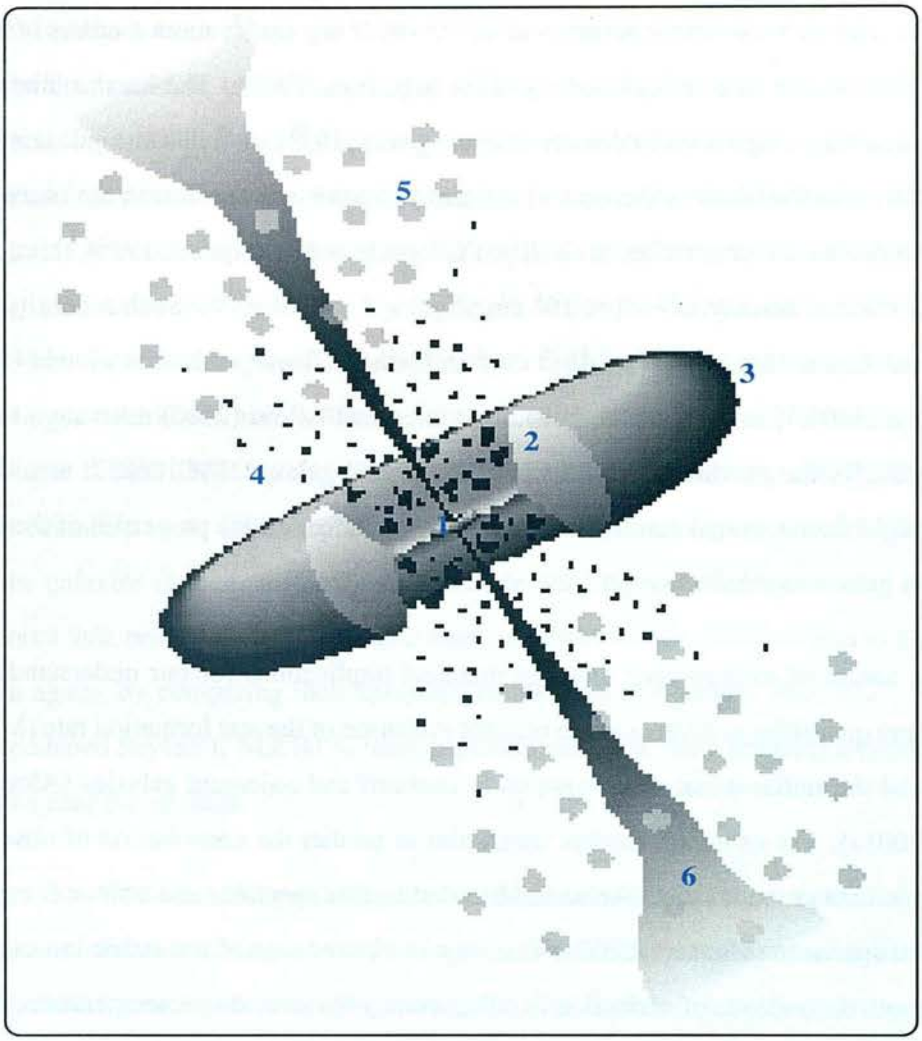

Figure 1.3: Cartoon of an AGN according to the unification hypothesis (not to scale). Adapted from Padovani (1988).

close to and heated by the central supermassive black hole. There will be little contribution from the dust in the spiral arms of a face-on galaxy, even if the telescope beam covers most or all of the galaxy's disc. This is in contrast with the situation in our own Galaxy, where most observations are of dust in the diffuse ISM, molecular clouds and circumstellar regions far from the nucleus, which in any case is currently in a quiescent phase (e.g. Gwinn et al., 1991).

The conditions under which the dust exists in AGN are very different from those in typical Galactic environments. Observations of the Seyfert II galaxy, NGC1068, for example, suggest a nuclear luminosity of $L_{IR} \sim 10^{11} L_{\odot}$ (e.g. Rieke and Low, 1975; Telesco et al., 1984; Tomono et al., 2001), and that this emission comes from a region perhaps a few tens of parsecs in radius. This implies energy densities of $10^{-7} - 10^{-8}$ erg cm^{-3}, about 4 orders of magnitude greater than in the solar neighbourhood ISM (e.g. Jura, 1987). The harsh radiation field is accompanied by a high column density of hydrogen, $> 10^{23}$ cm^{-2} in some galaxies (Maiolino et al., 2001b, and references therein). If the gas is located with the dust in the obscuring torus, and the torus has an outer radius of $\sim$ 10 pc (Taniguchi and Murayama, 1998), this corresponds to a gas number density of $\sim 3 \times 10^5$ cm^{-3} or $\sim 3 \times 10^{11}$ m^{-3}. Such a density would be somewhat higher than the $10^9 - 10^{10}$ m^{-3} in Galactic dense molecular clouds (Dyson and Williams, 1997). The dust can be hot, too: Marco and Alloin (2000) estimate a temperature of ~ 500K for the circumnuclear dust in the Seyfert II galaxy, NGC1068. It would hardly be surprising if such extreme conditions had a dramatic effect on the properties of the dust grains in active galactic nuclei.

The nature of extragalactic dust has practical implications for our understanding of processes and quantities as diverse as the redshift evolution of the star formation rate (Madau et al., 1998) and the stellar initial mass function in starburst and quiescent galaxies (Alonso-Herrero et al., 2001a). For example, studies which aim to predict the contribution of obscured AGN to cosmic backgrounds must take an unobscured quasar spectrum and redden it to predict the observed spectrum (Manners, 2002). This requires knowledge of the extinction curve, but the wavelength dependence of extinction is influenced by the size, shape, temperature, distribution and composition of the interstellar dust, none of which is likely to be known.

It is possible to obtain extinction curves for our and very nearby galaxies (e.g. M31, Bianchi et al., 1996) by observing individual stars of known spectral type, but this severely limits the sample of environments which can be studied. For more distant galaxies a Galactic extinction curve such as that of Cardelli, Clayton and Mathis (1989) is often assumed to apply, perhaps in conjunction with a Magellanic Cloud curve like that of Gordon and Clayton (1998), simply because it is not obvious what extinction curve really should be used. Alternatively, stellar evolution models can be used to produce an unobscured SED for a galaxy and this compared with observations to determine the form of the dust extinction. This has been done for samples of local starburst galaxies, which may be representative of high-redshift star-forming galaxies (Gordon and Clayton, 1998; Calzetti et al., 1994). Loska et al. (1993) present a method for calculating extinction curves for "nonstandard" grains, but this is of limited use when nothing is known about the grains in question.

Suggestions have been raised that there are indeed significant differences between Galactic dust and dust in AGN, particularly as far as the grain size distribution is concerned (see Maiolino and Natta, 2002, for a brief review). As far back as 1993, Laor and Draine carried out radiative transfer calculations which implied that the dust in AGN either lacks silicate grains or contains grains with sizes as large as 10μm. Recently, Maiolino et al. (2001a,b) observed that E_{B-V}/N_H tends to be lower, and A_V/N_H higher, in AGN than Galactic values. They considered a number of possible explanations, but favoured the idea that the grains in these galaxies are much larger (and hence have a flatter extinction curve in the optical) than those observed in the Galactic diffuse ISM. On the other hand, Weingartner and Murray (2002) dispute the method of Maiolino et al. (2001a,b), claiming that their N_H and E_{B-V} sample different regions of the galaxies studied. Instead, they conclude that "current observations are consistent with the torus dust being similar to Galactic dust". Crenshaw et al. (2001) come to a different conclusion again; by comparing their spectrum of the Seyfert I galaxy, NGC3227, with that of the unreddened Seyfert I, NGC4151, they conclude that NGC3227 contains a population of small grains near the nucleus.

The density of the dust and gas in the nucleus of an active galaxy may signal the presence of large grains. Numerous theoretical studies show that, under conditions of sufficient density, dust grains can stick to one another, leaving the dust depleted in small grains and with an enhanced number of larger grains. This process is thought to be observed in dense molecular clouds, where the optical/UV extinction curve is distinctly flatter than that observed in diffuse clouds — the greyness of the extinction is likely to be caused by the presence of grains large compared to the wavelength of the light (Chokshi et al., 1993; Ossenkopf, 1993). Conditions in AGN may favour the coagulation of grains, but if shocks occur in the dust, the picture will probably become a great deal more complicated. High-velocity shocks tend to remove a layer $\sim 0.02\mu$m thick from grains, which will result in the smallest grains being completely annihilated. Slower shocks, though, are more likely to lead to grain-grain collisions and therefore to the shattering of large grains (McKee, 1989; Draine, 1995). Clearly, it is not at all obvious whether the dust in AGN should be dominated by large or small grains, or indeed by any particular population at all. Any work which succeeds at pinning down patterns in the size of dust grains in AGN will be most welcome.

The composition of dust in other galaxies, in comparison with Galactic dust, is probably even more uncertain than the size of the grains. The obvious way of probing dust composition is to investigate spectral lines in the infrared, and individual spectral features from dust have been detected in a number of galaxies. The 9.7μm silicate dust feature has been known for some time, in tens of galaxies (Roche et al., 1991; Dudley and Wynn-Williams, 1997; Imanishi and Ueno, 2000). The feature tends to be weaker than expected from the measured A_V in a lot of galaxies and this has been another factor which has prompted suggestions of large grains in AGN. Alternatively, the dust could be depleted in silicates relative to carbonaceous grains — silicates are thought to be more easily destroyed in shocks (Seab and Shull, 1983; Granato and Danese, 1994).

Recently, Heckman and Lehnert (2000) made some of the first observations of extragalactic diffuse interstellar bands (DIBs), in a sample of nearby starburst galaxies. The carriers of the DIBs remain unknown but are thought to be large free molecules or some component of dust grains (Herbig, 1995). Remarkably, the relative strengths of the DIBs in Heckman and Lehnert's starburst galaxies are very similar to those of Galactic DIBs, and they also follow the same dependence of equivalent width on A_V. This seems to be an indication that dust (or large molecule) properties may be unexpectedly uniform even in the strong radiation fields and high gas densities of starburst galaxies. However, Heckman and Lehnert point out that if the photon energy density and gas pressure are both increased by the same amount, the ratio of number densities of gas atoms and photons/cosmic rays would remain similar (see also Wang et al., 1998). The ostensibly harsh starburst environment may not be so destructive after all; perhaps the same might be true for AGN. Interestingly, there seems to be some variation in DIB properties in the Magellanic Clouds (Ehrenfreund et al., 2002).

The 3.4μm feature has also been searched for in a number of Seyfert and ultraluminous infrared galaxies (Adamson and Whittet, 1990; Bridger et al., 1994; Wright et al., 1996; Imanishi et al., 1997, 1998; Imanishi, 2000a,b; Imanishi and Dudley, 2000; Imanishi et al., 2001). Intriguingly, it appears not to exist in some sources, but where it does, and in the very few cases in which the spectra are of high enough quality to allow comparison, the features again appear surprisingly similar to those observed in our galaxy (Wright et al., 1996). On the surface, this would seem to mean that the formation and evolution of carbon-containing dust follows a similar path in a wide range of galactic environments. Again, given the differences between lines of sight in our galaxy and the active systems in which the features are observed, their apparent similarity surely warrants further investigation.

Chapter 2 details observations we have made, aimed at understanding dust in the nearby Seyfert II galaxy NGC1068. We have carried out spectropolarimetry of the active nucleus of NGC1068 in order to test the core-mantle model of dust structure, but these observations have also allowed us, for the first time, to directly investigate the size distribution of the dust, its structure, and the nature of the carbonaceous component. After observing and modelling the polarisation and 3.4μm band of NGC1068 we have come to some interesting and perhaps unexpected conclusions.

1.4 The carbonaceous component of dust

A crucial tool in our investigation of the nature of dust has been the C-H bond stretch at 3.4μm. Although weak compared to, say, the 9.7μm silicate feature, this complex feature contains a wealth of information.

Chemical structures containing hydrogen bonded to an sp^3- hybridised carbon atom (Fig. 1.4) absorb light at just under 3000cm^{-1}, or around 3.4μm (e.g. Alpert et al., 1973). The absorption arises from a transition from the $\nu = 0$ to the $\nu = 1$ vibrational states of the carbon-hydrogen bond. It is quite distinct from that of a C-H bond stretch where the H atom is bonded to sp^2- or sp-hybridised carbon, which would be seen at wavenumbers $>$ 3000cm^{-1}. The 3.4μm feature has now been seen in a number of dusty lines of sight in the Galactic ISM (McFadzean et al., 1989; Sandford et al., 1991; Pendleton et al., 1994; Sandford et al., 1995; Chiar et al., 2002), informing us that the dust contains hydrocarbon chains like those that form the backbone of familiar terrestrial compounds such as alkanes and alcohols.

The 3.4μm band can generally be divided into four subfeatures, corresponding to two types of vibration - symmetric and asymmetric stretching - of C-H bonds of mid-chain or terminal carbon atoms. The asymmetric stretch bands of -CH$_3$ and -CH$_2$- groups in saturated hydrocarbons are found at approximately 2955cm^{-1} (3.38μm) and 2925cm^{-1} (3.42μm) respectively, while the -CH$_3$ and -CH$_2$- symmetric stretching bands lie at about 2870cm^{-1} (3.48μm) and

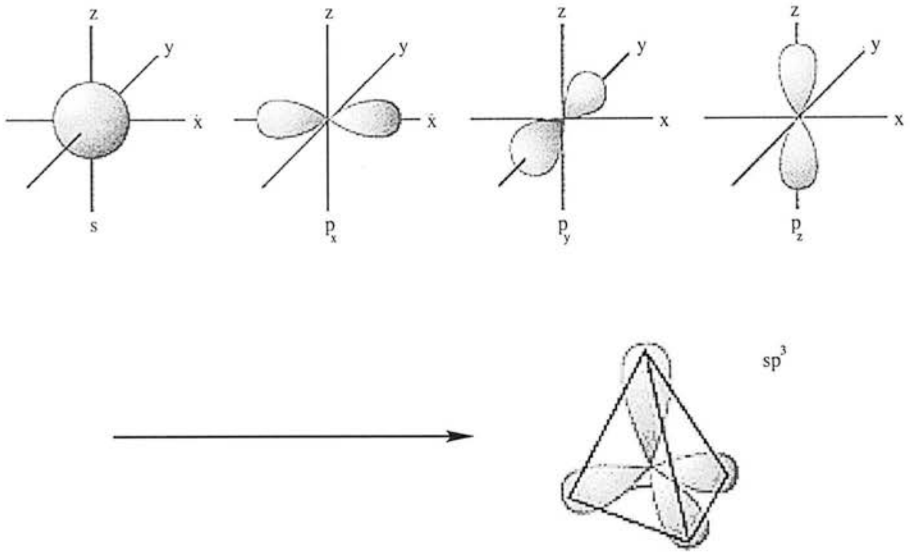

Figure 1.4: Hybrid orbitals. A carbon atom's 2s and three 2p orbitals can mix to form an sp^3 hybrid orbital. This new orbital is tetrahedral in shape and each lobe contains one electron. Each electron may pair up with an electron from another atom (hydrogen, for example) to form four single bonds. Similarly, a 2s orbital can mix with two 2p orbitals and form an sp^2 hybrid. The sp^2-hybridised carbon is planar and forms one double and two single bonds. sp-hybridised carbon (the 2s and one 2p orbitals) forms a triple and a single bond to other atoms. See e.g. Atkins (1994).

2860cm^{-1} (3.50μm). These positions can vary; the frequency at which a chemical bond absorbs or emits light is determined by the bond's force constant, $\nu_{osc} = \frac{1}{2\pi}\sqrt{\frac{f}{\mu}}$Hz, for a simple harmonic oscillator, where f is the force constant and μ the reduced mass of the two bonded atoms (Alpert et al., 1973), which in turn depends on the atoms in the bond and their chemical environment. This means that chemical bonds in slightly different environments may have distinguishable absorption lines in the IR spectrum.

The relative intensities of these features contains valuable information. The intensities are determined principally by the numbers of -CH_3 and -CH_2- groups in the chains, so as the chain length increases, introducing more -CH_2- groups, the strength of the -CH_2- bands will increase. Other effects are also apparent. For instance, the -CH_2- symmetric stretch is suppressed in molecules such as butanol which contain electronegative groups. The 3.4μm feature in astronomical lines of sight lacks a distinct band at 2860cm^{-1}, indicating that the hydrocarbon dust contains some O, N, and/or other electron-withdrawing atoms (Sandford et al., 1991).

Spectropolarimetry relies on the detection of small differences in intensity between spectra, meaning that polarimetric observations also provide very high signal-to-noise ratio (S/N) flux spectra of the source in question. Consequently, our observations of NGC1068 have resulted in one of the highest S/N spectra yet of the 3.4μm feature in an external galaxy, and in Chapter 4 I describe how we have been able to take advantage of this to probe the composition and structure of the dust in NGC1068. The depth and overall shape of the feature have allowed us to begin to understand the relationship between the carbonaceous and silicate components of the dust in NGC1068. The strengths and positions of the subpeaks within the feature, compared with those observed in the Galactic diffuse ISM, circumstellar dust and the ULIRG, IRAS 08572+3915, lead us to believe that the harsh environment of an active nucleus has much less of an effect on the organic fraction of the dust than might reasonably have been expected.

CHAPTER 2

Spectropolarimetry of NGC1068

2.1 Spectropolarimetry and the core-mantle dust model

It has long been known that light from distant stars is polarised by a few per cent, and the polarisation correlates well enough with extinction that its cause is now accepted to be selective absorption by aligned dust grains. If an unpolarised electromagnetic wave encounters an elongated dust grain in the right orientation, the component of the wave parallel to the grain's long axis is free to drive electrons along this axis. The energy of this component of the wave is thus used to heat the grain, so the wave which is finally transmitted is reduced in amplitude. The electrons in the grain are not free to move as far along the grain's short axis, so the component of the incident wave parallel to this axis is not as strongly absorbed. The net effect is preferential transmission of the electric field vector parallel to the grain's short axis; the transmitted wave becomes linearly polarised to some degree (§2.3). This effect is known as absorptive dichroism and the mechanism is analogous to that in operation in wire-grid polarisers and polaroid sheets.

An ensemble of aligned, elongated dust grains can be thought of as having two optical depths, one parallel to the grain's short axis, $\tau_y(\lambda)$ and another perpendicular to this, $\tau_x(\lambda)$. As the component of the electric field parallel to the grain's short axis is less efficiently absorbed than the orthogonal component, $\Delta\tau(\lambda) = \tau_x(\lambda) - \tau_y(\lambda) \neq 0$, and the grains are dichroic. If the grains are illuminated by an unpolarised background source, the polarised intensity of light transmitted through the grains will be

$$P_{abs}(\lambda) = I_0(\lambda)(e^{-\tau_x(\lambda)} - e^{-\tau_y(\lambda)}) \tag{2.1}$$

and the polarised fraction of the light,

$$p_{abs}(\lambda) = \frac{e^{-\tau_x(\lambda)} - e^{-\tau_y(\lambda)}}{e^{-\tau_x(\lambda)} + e^{-\tau_y(\lambda)}}. \tag{2.2}$$

When $\Delta\tau(\lambda)$ is small, this is approximately

$$\begin{aligned} p_{abs}(\lambda) &\approx -\Delta\tau(\lambda)/2 && (2.3)\\ &\approx -f(\lambda)\tau(\lambda), && (2.4) \end{aligned}$$

provided the band strength of any absorption features is small and $f(\lambda)$ only a weak function of wavelength. Polarisation due to selective absorption is therefore proportional to optical depth (Aitken, 1989).

That being the case, where grains are elongated, aligned, and absorbing, one can expect to observe polarisation of the continuum, with enhanced polarisation over absorption features. That is exactly what is observed in a number of lines of sight, perhaps most spectacularly towards the BN object in the Orion Nebula. There, as the optical depth of the 9.7μm silicate feature increases, the polarisation rises from a value of $\sim 2\%$ at the short-wavelength edge of the feature, to 13% at its peak (Aitken et al., 1989, see also Fig. 2.10).

We can use this effect to our advantage. In the core-mantle dust model, the coated silicates account for most of the IR extinction and polarisation in the diffuse ISM. If, in a given line of sight, we observe that the polarisation over the silicate absorption feature is greater than that in the continuum, this means that the silicate component of the grains is aspherical and aligned. In this model the aligned silicate grains possess organic mantles which clearly must also be aligned, and will therefore give rise to enhanced polarisation over any absorption features associated with them. The model also states that the 3.4μm C-H bond stretch, observed to be correlated with the 9.7μm silicate band in the diffuse ISM, arises in the carbonaceous grain mantles. This means that measurements of the polarisation of the 9.7 and 3.4μm features can be a rigorous check on the validity of the core-mantle model of dust grain structure.

Enhanced polarisation over the silicate feature has been known for some time, but the first search for polarisation in the 3.4μm feature was carried out by Adamson et al. (1999, hereafter A99). The Galactic Centre infrared source GCIRS 7 was chosen as it is both bright enough and has a deep enough 3.4μm feature for sufficiently sensitive polarisation measurements to be made. Unfortunately, no measurement of the polarisation over the 9.7μm silicate feature towards GCIRS 7 exists at the time of writing. This admits the possibility that the silicate feature is unpolarised, and that the grains in that line of sight are not in fact elongated and/or aligned. On the other hand, the silicate feature towards the source GCIRS 3 is known to show polarisation of $\Delta p_{9.7} \approx 4\%$ above the continuum polarisation (Aitken et al., 1986). GCIRS 3 lies at a projected distance of only about 0.25pc from GCIRS 7 (Geballe et al., 1989), and as such could reasonably be expected to probe regions where grain properties and alignment are very similar to GCIRS 7. And, as we shall see, the 3-4μm continuum polarisation of GCIRS 7 itself is about 1.5%. These two observations point to the presence of polarising dust grains in the diffuse ISM towards GCIRS 7.

Knowing the optical depth, $\tau_{9.7}$ and polarisation increase, $\Delta p_{9.7}$ in the silicate feature towards GCIRS 3, A99 were able to derive the ratio $\Delta p_{9.7}/\tau_{9.7} = 1.1$[1]. If the band strength of the silicate material and the degree of grain alignment are the same towards GCIRS 7 as towards nearby GCIRS 3, this relation should also hold for GCIRS 7. Assuming that $(\Delta p/\tau)_{3.4} \approx (\Delta p/\tau)_{9.7}$ (and recent work by Li and Greenberg (2002) confirms that this is a good approximation), their measured $\tau_{3.4} = 0.36$ in GCIRS 7 led A99 to predict that a polarisation increase of about 0.4% would be observed at 3.4μm if the core-mantle model were correct. Their spectropolarimetry of the 3.4μm feature in GCIRS 7, though, gave an upper limit on the polarisation increase over the feature of $< 0.08\%$, above a continuum polarisation of approximately 1.5%. This is plainly well below the value to be expected on the basis of the core-mantle dust model.

---

[1] $\Delta p_{9.7}/\Delta\tau_{9.7}$ in their notation

On the face of it, this is a convincing demonstration that the L&G model is badly flawed, that core-mantle grains do not make up a significant fraction of the diffuse cloud grain population. However, there remain one or two reasons to doubt this conclusion. Although the 1.5% polarisation of the 3-4μm continuum towards GCIRS 7 strongly suggests that there are polarising dust grains in the line of sight, the fact remains that the polarisation of the silicate feature in GCIRS 7 is unknown. If it turns out to be very different from that observed in GCIRS 3 the expected $\Delta p_{3.4}$ could be lower.

Another potential problem is that about 10 of the 30 or so magnitudes of extinction towards GCIRS 7 comes from dust in molecular clouds. Dense cloud dust appears not to contain the material which gives rise to the 3.4μm feature (Brooke et al., 1996, 1999). If for some reason the polarising grains were largely confined to the dense clouds then only a small $\Delta p_{3.4}$ would ever be seen towards GCIRS 7, less than the 0.4% predicted by a model in which the 3-4μm polarisation arises in diffuse cloud dust. This seems unlikely, as dust in molecular clouds exhibits decreasing polarisation with increasing A_V (Lazarian et al., 1997; Whittet et al., 2001), but cannot be ruled out.

Ishii et al. (2002) have also examined the polarisation behaviour of the 3.4μm feature, in the line of sight towards the young stellar object, IRAS18511+0146. They found that this source, too, shows no excess polarisation over the band, with an upper limit of $\Delta p/\tau_{3.4} < 1\%$. Unfortunately, this study suffers from the same drawbacks as the previous one, namely that the authors mention no measurement of silicate polarisation in this line of sight, and their spectra contain the deep ice absorption indicative of molecular cloud material.

Observations in other lines of sight would help to clarify the situation, but Galactic sources which are both bright and obscured enough to possess a significant 3.4μm feature are rare. The technology which would permit sensitive spectropolarimetry of these sources is now becoming available; most crucially, the Michelle spectrometer on the 8m Gemini North telescope should soon allow measurements of the polarisation of the silicate feature in GCIRS 7. However, 10m-class telescopes with polarimetric capability lay still in the future at the time this project was conceived. Accordingly, as a further test of the core-mantle model, and to investigate the nature of dust in a galaxy other than our own, we have attempted to measure the polarisation of the 3.4μm and 9.7μm features in the nucleus of the luminous, dusty Seyfert II galaxy, NGC1068.

2.2 NGC1068

As the galaxy that inspired the unification hypothesis, NGC1068 is probably the most-studied active galaxy. Its distance, a mere 15Mpc ($H_0 = 75 \mathrm{km\,s^{-1}\,Mpc^{-1}}$), means that $1''$ corresponds to about 70pc on the galaxy. The diffraction-limited 3μm resolution of a four-metre telescope, for example, is just under $0''.2$, so NGC1068 is an ideal candidate for research aiming to understand in detail the nucleus of an active galaxy. As applied to NGC1068, a type-II Seyfert galaxy, the unified model would say that the dusty torus is approximately edge-on to us and that the broad lines visible only in polarised light are deflected into our line-of-sight by the electrons or dust in the scattering mirror (Antonucci and Miller, 1985, see also Fig. 1.3).

We already have a reasonably detailed view of the central few hundred parsecs of NGC1068, and Fig. 2.1 aims to put into perspective the region of dust studied in this project. The galaxy is an SA-type spiral galaxy measuring about $7.1' \times 6.0'$, as shown in the top panel of Fig. 2.1. At about $10 - 15''$ from the nucleus (and not visible in the figure) is a ring of furious star formation, but the real AGN action starts much closer in. In the background of the middle panel is the northern ionisation cone or narrow-line region (Macchetto et al., 1994), seen in OIII emission. There is a corresponding southern cone, but it is much fainter and is thought to be hidden behind the disc of the galaxy. In the centre of the image, intense radio and infrared emission mark the location of the deeply obscured "true" nucleus (Gallimore et al., 1996; Tomono et al., 2001). Also shown in Fig. 2.1 is an L-band image of the central couple of arcseconds (Marco and Alloin, 2000) in which can be seen a suspiciously doughnut-shaped, horizontal feature. Extending across perhaps $1''$ or 70pc, this fits in quite well with the predicted dimensions of the dusty molecular torus postulated by the unified model of AGN. The E-W structure is curiously absent in images at longer IR wavelengths (Bock et al., 2000; Alloin et al., 2000), but there is still little doubt that the IR emission is due to hot dust surrounding the hidden nucleus[2].

A great advantage of studying NGC1068 in particular is that the disc of the galaxy is almost face-on to us. This, together with our high spatial resolution, means that the line of sight to the

---

[2] Alloin et al. (2000) suggest that the horizontal structure in the near-IR maps traces not the torus itself, but dust in the same plane merging with dust and gas in the galaxy's disc. If some local source of heating were present at this interface (e.g. star formation), the dust could be prominent at short wavelengths and not have the associated cool dust and longer-wavelength emission predicted by torus models with heating only from the central engine.

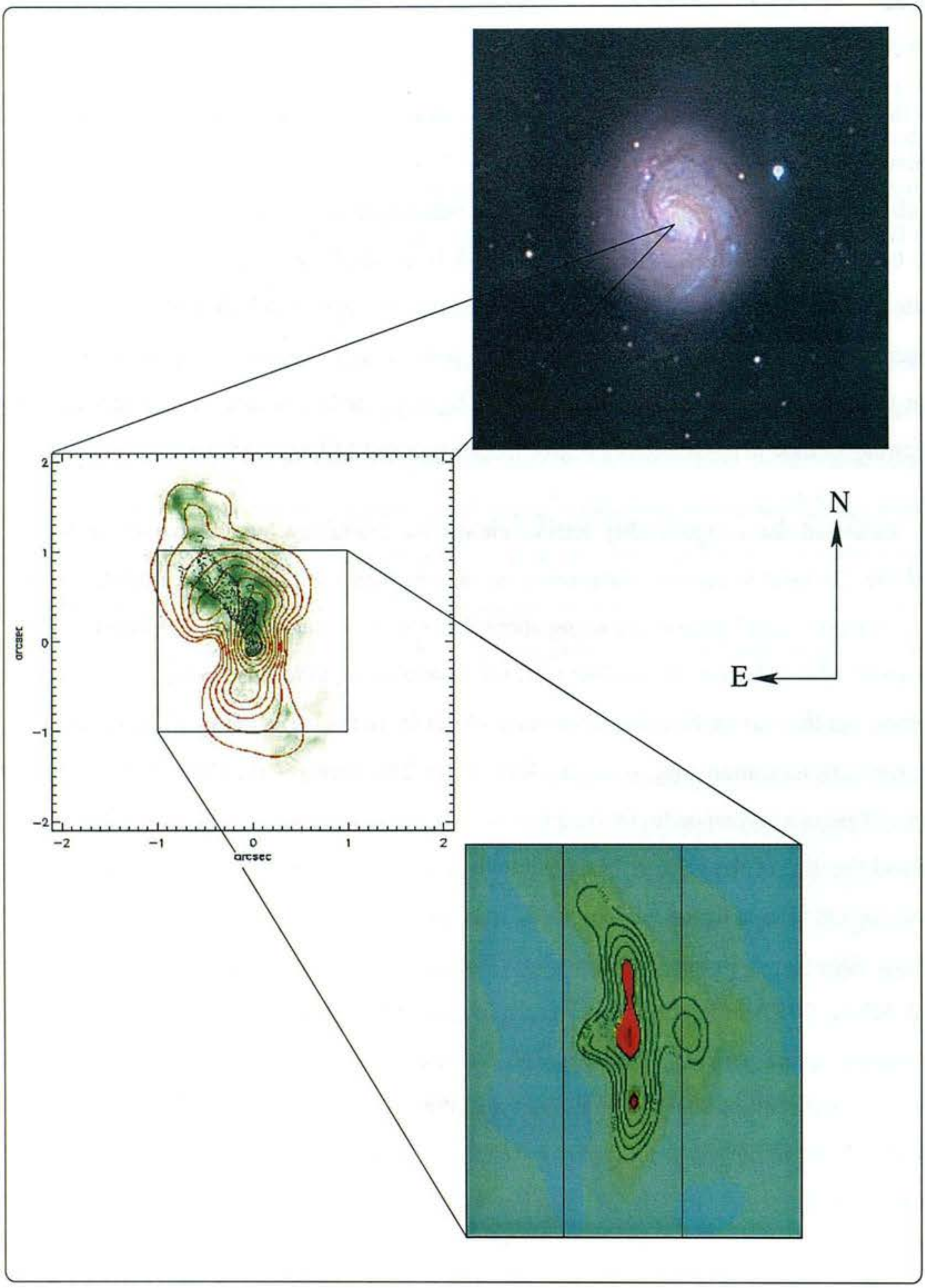

Figure 2.1: The central few arcsec of NGC1068. The red contours in the middle panel show 12.3μm emission, the black contours, 6cm radio emission and the green background, [OIII] emission in the NLR. Adapted from Galliano et al. (2003). Lower panel: L-band image, with vertical lines showing the approximate area covered by the 1-pixel-wide slit of the CGS4 spectrometer on UKIRT, in a N-S orientation.

	Centre of NGC1068	Galactic Diffuse ISM	Galactic Molecular Cloud
3.4μm feature?	Yes	Yes	No
3.1μm feature?	No	No	Yes
Density	$N_{H_2} \sim 10^{11}\mathrm{m}^{-3}$	$10^7 - 10^9$ atoms m^{-3}	$10^9 - 10^{10}$ mol. m^{-3}
Dust temperature	Few hundred K	$\sim$ 20K	$\sim$10K

Table 2.1: Comparison of some properties of the circumnuclear environment of NGC1068 with two Galactic environments. NGC1068's gas density as found by Tacconi et al. (1994)

nucleus is likely to sample dust local to the active nucleus, with little contribution from dust in the ISM of the disc of the galaxy. This should avoid the need to disentangle populations of dust which could potentially differ greatly from each other. The width of the slit of the spectrometer used for our observations (CGS4) is $0''.6$ ($\approx 40\mathrm{pc}$) and the extent of the dusty torus found by Marco and Alloin (2000) is ~80pc in the L band, so the region we observe is roughly the same size as a Galactic giant molecular cloud complex.

The density of the dust may be somewhat higher than that of a Galactic molecular cloud — the central few hundred parsecs of NGC1068 are thought to contain regions with $\mathrm{n}_{\mathrm{H}_2} \sim 10^5\mathrm{cm}^{-3}$ (Tacconi et al., 1994). However, spectra of the nuclear regions of NGC1068 show no evidence for water ice in the form of absorption at 3.1μm, a signature of molecular clouds in our galaxy (Wright et al., 1996). This is not unexpected; the intense near-IR emission from the dust indicates that it is considerably warmer than dense cloud dust and certainly too hot for the existence of icy grain mantles. The 3.4μm feature has, however, been observed in the nucleus of NGC1068 (Bridger et al., 1994; Wright et al., 1996; Imanishi et al., 1997). The signal-to-noise ratio (S/N) of these observations does not permit a detailed comparison (a situation which I remedy in this thesis), but the band does not show any gross differences from that observed in the Galactic diffuse ISM.

As shown by Table 2.1, the signs point to an environment in which dust grows to bear at least a broad resemblance to Galactic diffuse dust, but which is simultaneously warm and dense, unlike many Galactic environments. This turns out to have interesting consequences for the dust grains in NGC1068, something which is explored in detail in Chapter 4. For the moment, however, the bright background source and abundant dust in the galaxy make it simply a convenient laboratory for testing the core-mantle model of interstellar dust.

2.3 Polarised light

Light whose electric field has a constant orientation is known as linearly (or plane-) polarised light. A polarised wave can be resolved into two orthogonal component waves; alternatively, Maxwell's equations for an electromagnetic wave can be solved to yield two mutually perpendicular, linearly polarised waves with electric field vector $\mathbf{E}$

$$\mathbf{E}_x(z,t) = \hat{\mathbf{i}} E_{0x} \cos(kz - \omega t) \tag{2.5}$$

$$\mathbf{E}_y(z,t) = \hat{\mathbf{j}} E_{0y} \cos(kz - \omega t + \epsilon), \tag{2.6}$$

in this case travelling in the z-direction with a relative phase difference, ϵ (Tinbergen, 1996). It is the way in which these waves are combined which determines the state of polarisation of the resulting wave.

If the two waves are in phase, $\epsilon = 0$ and their sum is the wave

$$\mathbf{E} = (\hat{\mathbf{i}} E_{0x} + \hat{\mathbf{j}} E_{0y}) \cos(kz - \omega t) \tag{2.7}$$

which has a fixed amplitude and a fixed direction of vibration *i.e.* it too is linearly polarised. The relative amplitudes of the original waves determine the direction of vibration, that is, the position angle of the polarisation.

If, on the other hand, the waves are of equal amplitude but 90° out of phase, their sum becomes

$$\mathbf{E} = E_0[\hat{\mathbf{i}} \cos(kz - \omega t) - \hat{\mathbf{j}} \sin(kz - \omega t)]. \tag{2.8}$$

The amplitude "contributed" from each wave varies over time; when one wave is at its maximum amplitude, the orthogonal wave is at its minimum. This means that the direction of vibration of $\mathbf{E}$ rotates about the direction of propagation of the wave, though its magnitude does not change. This is circular polarisation, and can be either left- or right-handed.

Of course, the two orthogonal waves are not restricted to being in phase or 90° out of phase. With any other phase relationship both the direction and magnitude of $\mathbf{E}$ change as the

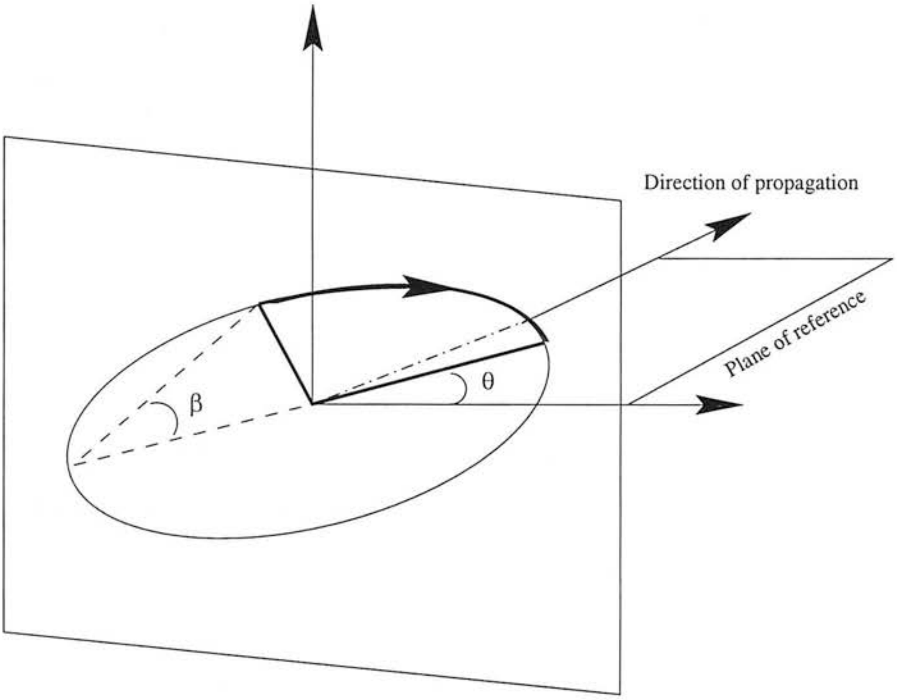

Figure 2.2: The polarisation ellipse for right-handed elliptical light. $\tan\beta$ is the ellipse axial ratio; the equivalent diagram for plane-polarised light would have an axial ratio of 0, for circular light, 1. θ is the position angle of polarisation. Adapted from Tinbergen (1996).

wave propagates, and $\mathbf{E}$ now describes an ellipse about the direction of travel of the wave. This is known as elliptical polarisation. Linear and circular polarisation are two special cases of elliptical polarisation, where the ellipse axis ratios are 0 and 1, respectively. Fig. 2.2 shows the path traced out by the electric field vector of right-handed elliptical light.

Unpolarised (or natural) light can be thought of as composed of two orthogonal waves with no long-term phase relation. A source of unpolarised light, a star for instance, contains many individual light-emitting particles. Each particle will emit a wave of polarised light, but when the average is taken over all the particles and over a sufficiently long time (as is always the case in practice), all possible polarisation states will be observed and none will dominate.

A condition frequently met in astronomy, and which is of particular interest in this thesis, is that of light which is partially linearly polarised. In common with the other polarisation states, partially linearly polarised light can be produced by particles in emission, but the polarising mechanism which is of concern here is an absorptive mechanism. As described in §2.1, aligned, aspherical dust grains are able to preferentially remove one component of the electric field of unpolarised incident light. In this case all directions of vibration of **E** are observed but one dominates over the others to a greater or lesser extent. Partially polarised light can therefore be thought of as the sum of a fully polarised and an unpolarised component.

2.3.1 The Stokes parameters

The Stokes parameters are a convenient mathematical description of both fully and partially polarised light, and can be related to the polarisation ellipse shown in Fig. 2.2. If $I_{P(U)}$ is the intensity of polarised (unpolarised) light and P_E the degree of polarisation, the Stokes parameters are

$$I = I_U + I_P \tag{2.9}$$

$$Q = IP_E \cos 2\beta \cos 2\theta = I_U P \cos 2\theta \tag{2.10}$$

$$U = IP_E \cos 2\beta \sin 2\theta = I_U P \sin 2\theta \tag{2.11}$$

$$V = IP_E \sin 2\beta = I_U P_V, \tag{2.12}$$

where $P = P_E \cos 2\beta$, the degree of linear polarisation, and $P_V = P_E \sin 2\beta$, the degree of circular polarisation.

More intuitively, the Stokes parameters can be defined operationally, in terms of the behaviour of light passing through a particular set of four filters. When illuminated by unpolarised light, each filter will transmit half of the incident light, but while the first filter passes all polarisation states with equal efficiency, the other three are all polarisers. The second filter is a horizontal linear polariser, the third has its transmission axis at 45° and the final filter is a circular polariser. If each filter is positioned separately in the beam, the transmitted irradiances are I_0, I_1, I_2 and I_3. The Stokes parameters are then defined as

$$I = 2I_0 \tag{2.13}$$

$$Q = 2I_1 - 2I_0 \tag{2.14}$$

$$U = 2I_2 - 2I_0 \tag{2.15}$$

$$V = 2I_3 - 2I_0 \tag{2.16}$$

Clearly, the Stokes parameter I is the incident irradiance. Q, U and V express the polarisation state of the light, whether linear or circular and in what direction. For example, for unit incident irradiance, if $I = Q = 1$ and $U = V = 0$, the incoming light is completely linearly polarised in the horizontal direction.

The degree of linear polarisation of a beam of light is the ratio of polarised to unpolarised intensity, which, in terms of the Stokes parameters, is

$$p = \frac{I_P}{I_P + I_U} \tag{2.17}$$

$$= \frac{\sqrt{Q^2 + U^2}}{I} \tag{2.18}$$

The position angle of polarisation is given by

$$\theta = 0.5 \tan^{-1}(U/Q). \tag{2.19}$$

The great advantage of the Stokes parameters is that, as will be demonstrated in §2.4.1, they all are or can be derived from observable quantities.

2.4 The L-band polarisation of NGC1068

2.4.1 Dual-beam polarimetry: CGS4+IRPOL2

To benefit from the relatively large collecting area and good site of the United Kingdom Infrared Telescope (UKIRT), our L-band spectropolarimetry of NGC1068 was carried out using UKIRT's spectrometer, CGS4 and polarimetry module, IRPOL2. IRPOL2 utilises the technique of dual-beam polarimetry, which has the advantage of being relatively unaffected by the variations in atmospheric transmission so common in the infrared.

As described in §2.3, one orientation of the electric field vector is favoured when light is partially linearly polarised. The key to determining the extent to which the light is polarised, and in what direction, lies in directing the incident light through an ideal linear polariser — the analyser — and detecting differences in the transmitted intensity as this device is rotated. A perfect analyser will transmit only the component of the electric field parallel to a certain axis, so if the analyser were gradually rotated the measured intensity would be at a maximum when the analyser angle coincided with the position angle of polarisation of the incident light. The minimum intensity would be measured at 90° to this. This variation in intensity has a characteristic sine wave pattern and is described by Malus's law as

$$I(\theta) = I(0)\cos^2\theta \tag{2.20}$$

where θ is the angle between the position angle of polarisation and the angle of the analyser's transmission axis. The sine wave pattern of the variation in intensity means that, rather than rotating the analyser slowly through 180°, only two analyser positions, 45° apart, are necessary to measure the degree and angle of linear polarisation.

In a dual-beam polarimeter, the analyser is a beam-splitting polariser such as a Wollaston prism. Made of quartz or calcite, the Wollaston prism splits the incident light into two parallel beams, linearly polarised with orthogonal position angle. These are the ordinary (o) and extraordinary (e) beams. With the analyser in the 0° position, the o-beam spectrum records the intensity $i_{0,||}$, the e-beam spectrum $i_{0,\perp}$. By Malus's law, these intensities are

$$i_{0,||} = I_P\cos^2\theta + \frac{I_U}{2} \tag{2.21}$$

$$\begin{aligned} i_{0,\perp} &= I_P\cos^2(90-\theta) + \frac{I_U}{2} & (2.22)\\ &= I_P\sin^2\theta + \frac{I_U}{2} & (2.23) \end{aligned}$$

where I_P and I_U are the polarised and unpolarised intensities of the incoming light. We can use these expressions to obtain the Stokes parameter Q

$$\begin{aligned} i_{0,||} - i_{0,\perp} &= I_P\cos^2\theta - I_P\sin^2\theta & (2.24)\\ &= I_P\cos 2\theta \\ &= Q \end{aligned}$$

Similarly, with the analyser in the 45° position, the e- and o-beams measure the intensities $i_{45,||}$ and $i_{45,\perp}$. The difference $i_{45,||} - i_{45,\perp}$ gives the Stokes U parameter. The degree and position angle of linear polarisation may then be calculated using equations 2.18 and 2.19.

In practice, however, several alterations are made to the basic method. Firstly, rotating the analyser by 45° would cause the e- and o-beams to overlap on the detector. In IRPOL2 this is avoided by placing a half-wave plate in front of the Wollaston prism. The half-wave plate rotates the plane of polarisation of the incident light in such a way that rotating the retarder by $22.5°$ has the same effect as moving the prism by $45°$.

Secondly, measurements are carried out with the waveplate at $45°$ and $67.5°$, as well as at $0°$ and $22.5°$, which helps to deal with the instrumental and atmospheric effects which can be significant sources of error. Given that polarimetry relies on detecting differences in intensities between spectra at different waveplate angles, variations in atmospheric transmission between measurements can easily introduce spurious polarisations. Other effects include polarisation induced by the grating of the spectrometer, which can act a little like a wire grid polariser in the beam. The great advantage of the dual beam system is that many of these factors can be effectively cancelled out, and their removal proceeds as follows (Tinbergen, 1996):

$$i_{0,||} = 0.5(I + I_P)G_{||}F_0 \tag{2.25}$$

$$i_{0,\perp} = 0.5(I - I_P)G_{\perp}F_0 \tag{2.26}$$

$$i_{45,||} = 0.5(I + I_P)G_{||}F_{45} \tag{2.27}$$

$$i_{45,\perp} = 0.5(I - I_P)G_{\perp}F_{45} \tag{2.28}$$

The i values are the e- and o-beam intensities measured by the detector at each waveplate position, I and I_P are total and polarised light input. $G_{||}$ and $G_{\perp}$ are the e- and o- beam spectra at each exposure, including polarisation-dependent sources of error such as the sensitivity of a particular pixel to polarised light. F_0 and F_{45} account for polarisation-independent sources of error, like atmospheric transmission, at each waveplate angle.

Dividing the e- and o-beam spectra at each waveplate angle removes the F-factors, and therefore variations in atmospheric conditions. Dividing the observations at pairs of waveplate angles cancels the G-factors, removing the polarisation-dependent errors.

This is the origin of the "ratio method" of obtaining the Stokes Q and U parameters:

$$R^2 = \frac{i_{0,||}/i_{0,\perp}}{i_{45,||}/i_{45,\perp}} \tag{2.29}$$

$$q = \frac{Q}{I} = \frac{R-1}{R+1} \tag{2.30}$$

Substituting 22.5° and 67.5° for 0° and 45° gives the parameter $u = U/I$. The degree and position angle of the polarisation are then found in exactly the same way as in §2.3.1.

2.4.2 Observations and data reduction

L-band spectropolarimetry of the nucleus of NGC1068 was performed on the nights of 2000 September 19th and 2000 October 6th using the IRPOL2 polarimetry module and CGS4 spectrometer on UKIRT. In order to provide coverage of the 3.4μm feature and the continuum around it, we employed the 40 l/mm grating in first order, centred at 3.4μm. This setup gives a resolving power of about 1360 at the central wavelength, and a spectral coverage of 0.64μm. The $0''.6$ 1-pixel-wide slit of CGS4 was used, thereby maximising the spectral resolution of the observations, and the slit was orientated approximately north-south, though the distribution of the flux in NGC1068 means that the slit angle is not crucial (see Fig. 2.1). Background-limited exposure times of 2.0s on the galaxy were used, and 2x2 sampling. NGC1068 was initially located using its NED[3] coordinates, then a peak-up was performed, ensuring that the galaxy was observed at the peak of its nuclear L-band emission.

There is considerable sky background emission in the L band, so the telescope was nodded by $10''$. The technique of "nodding" involves moving the telescope a few times a minute so that the source falls onto a part of the array that previously contained only blank sky. Subtracting one observation from the subsequent, nodded observation during later data reduction then permits removal of the bulk of the background emission. This particular offset was chosen to avoid the spectra overlapping on the array when the sky and object beams were subtracted. In the L band, the e- and o-beams are separated by 31 pixels or about $19''$and NGC1068's flux extends over about 5 rows, so the $10''$nod was necessary to avoid any overlap; unfortunately, it meant that the offset beam was positioned on NGC1068's circumnuclear star-forming ring. However, the contrast in flux between the nucleus and the star-formation region is so great that we do not expect significant contamination. For example, Davies et al. (1998) find that the 2μm flux in the ring is nowhere greater than 4mJy in a $3''$aperture, whereas the nuclear K-band flux ~370mJy (Rieke and Low, 1972, $6''$aperture). An unpolarised (HD18803) and a polarised (AFGL2591) standard star were also observed on each of those nights with the same instru-

---

[3] NASA/IPAC Extragalactic Database, nedwww.ipac.caltech.edu

mental configuration (except that the exposure time was reduced to 0.12s for AFGL2591), and the data reduced in the same manner as will be described for NGC1068.

In order to obtain Stokes Q and U parameter spectra a frame was taken with IRPOL2's half-wave plate at each of four positions: $0^\circ, 45^\circ, 22.5^\circ, 67.5^\circ$ in that order . The telescope was nodded to obtain an "object" and a "sky" frame at each waveplate position and the cycle repeated 64 times in all. Initial data reduction was carried out by UKIRT's data reduction pipeline, ORACDR, using the recipe "REDUCE_SINGLE_FRAMES". This recipe starts by masking bad pixels, then subtracts a bias frame to correct for the array's zero-point offset. To correct for variations in pixel sensitivity across the array, the recipe goes on to divide each frame by a flat field, the image of a featureless blackbody source within the instrument. The 2x2 sampling involves stepping the array by a small amount between exposures, and these frames are interleaved at this stage in the data reduction. The exposures are then coadded and the resulting frames given an estimated wavelength scale.

Fig. 2.3 illustrates some of the subsequent steps in the data reduction. Inspection of the sky emission lines in the images and of lines from an argon arc lamp showed that they were distinctly slanted on the array; in other words the pixel-wavelength relation varied from top to bottom on the array. This arises because IRPOL2's Wollaston prism is located in front of CGS4's slit, meaning that the slit must be orientated so as to allow both the e- and o-beams to pass through. The slit is usually projected onto the array perpendicular to the direction of dispersion, but the presence of the polarimeter means that this is not possible and the images are tilted. As the spectrum of NGC1068 was extended over several rows, I corrected for this using the routines ARC, IARC and ISCRUNCH from Starlink's Figaro data reduction package. ARC assigns wavelengths to the lines in the spectrum of an argon arc lamp extracted from a row in the centre of the array, effectively determining the pixel-number — wavelength conversion for that row. Starting from this fit, IARC looks for the arc lines in neighbouring rows and performs the same kind of fit in each row of the array. ISCRUNCH (or ISCRUNI, if arc images bracketing the object observations are available) uses the pixel — wavelength relationships given by IARC to rebin the data in each row in the target images to the corrected wavelength scale. This procedure effectively corrected the tilt of the images on the array — as shown by Fig. 2.3 — and wavelength-calibrated the data.

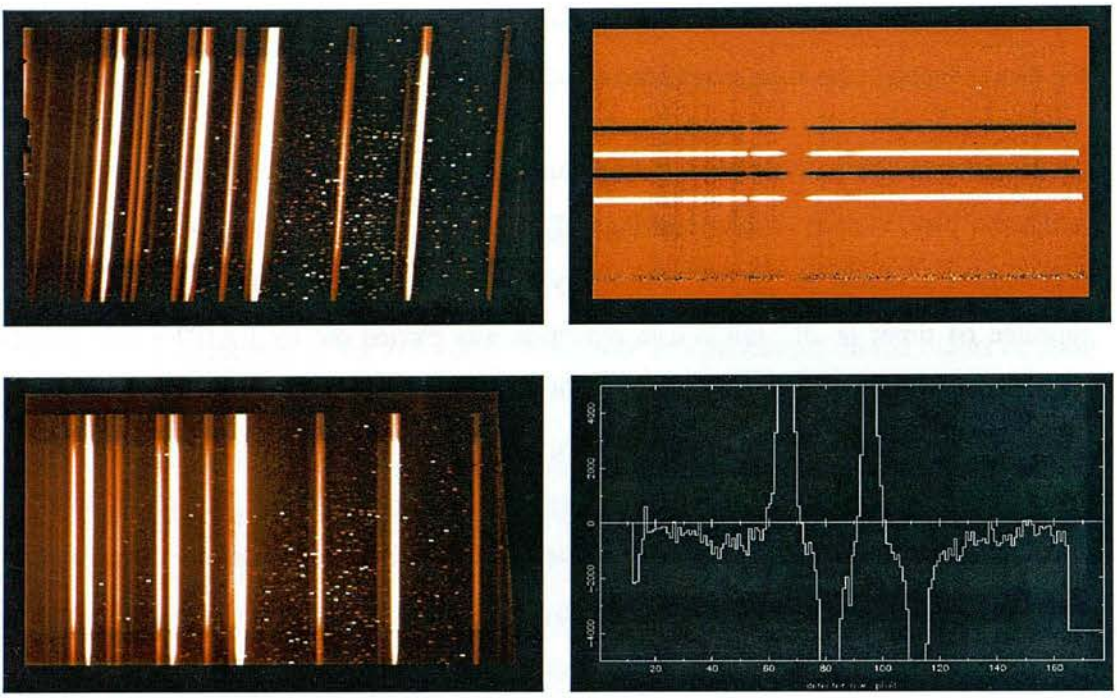

Figure 2.3: Left panels: lines from an argon arc lamp, before and after correcting for the slant caused by the orientation of CGS4's slit. Top right: a typical frame after subtraction of the sky and object observations, showing the positive and negative e- and o-beams. Bottom right: y-cut through such a frame, showing the small residual sky background.

At this stage, the nodded sky and object pairs were subtracted to remove some of the background sky emission. In many cases this worked very well and the residual emission was small (see Fig 2.3). Still, the Figaro routine POLYSKY was used to fit a polynomial to the signal on either side (spatially) of the object spectrum and subtract the residual.

The e- and o-beam spectra were extracted using the Figaro applications PROFILE and OPTEXTRACT, based on the optimal extraction algorithm of Horne (1986). Straightforward extraction entails finding a balance between extracting over too many rows on the array and therefore adding noise to the spectrum, or too few, and losing valuable flux from the object. Optimal extraction deals with this problem by assigning weights to the pixels in the image according to their variance. A profile of the object is created in the spatial direction, then a polynomial fit performed to each row in the dispersion direction, so the result is an image containing the relative weights to be assigned to the pixels containing information on the object. The spectrum is then simply extracted according to these weightings. Pairs of "sky" and "object" spectra (shown as black and white in Fig. 2.3) are then subtracted.

At this stage, the NGC1068 data take the form of 128 e-beam and 128 o-beam spectra of the 3.4μm feature and the continuum around it, with equal numbers at each of the four waveplate angles.

2.4.3 Constructing the polarisation spectrum of NGC1068

The data were now ready to be transformed into Stokes q and u parameter spectra. The highest S/N q and u spectra are generally obtained by summing up the e- and o-beam spectra at each waveplate angle and calculating q and u using the ratio method on the totalled spectra. It is also possible to find individual q and u spectra for each cycle of waveplate positions and coadd them all, but this can mean that significant errors are propagated into the final q and u spectra. In fact, I found that NGC1068 is bright enough that both methods give virtually indistinguishable results; those presented here are based on the latter method, for reasons to do with error calculation which will become clear below.

In principle the polarisation spectrum could now be calculated. Prior to this, however, further treatment of the raw Stokes parameter spectra was necessary, as illustrated in Fig. 2.4. Firstly, data points between 3.3μm and 3.4μm (before any redshift correction) were rejected. This part of the spectrum contains deep absorptions from the hydrocarbon cement in IRPOL2's Wollaston prism (at $3.35 - 3.4\mu$m) and from atmospheric methane ($3.31 - 3.33\mu$m), and these lines do not ratio out satisfactorily . Most of the other telluric lines cancel quite well when the e- and o-beam ratios are taken.

A second effect which must be dealt with is a large-amplitude ripple in the spectrum which is thought to be caused by multiple reflections in the waveplate. Aitken and Hough (2001) point out that, in an exact half-wave plate, the reflected e- and o-beams all end up in phase with their simply- transmitted counterparts and the polarisation is unchanged. They go on to show, however, that if the waveplate is not a simple, exact half-wave plate, the e- and o-rays can be shifted in phase by different amounts, and a ripple appears in the spectrum. Infrared polarimeters are particularly prone to this effect, as there is often no choice but to construct infrared half-wave plates from two distinct plates (of MgF_2 in the case of IRPOL2), neither of which is a perfect half-wave plate but which together can act as one. In the NGC1068 data,

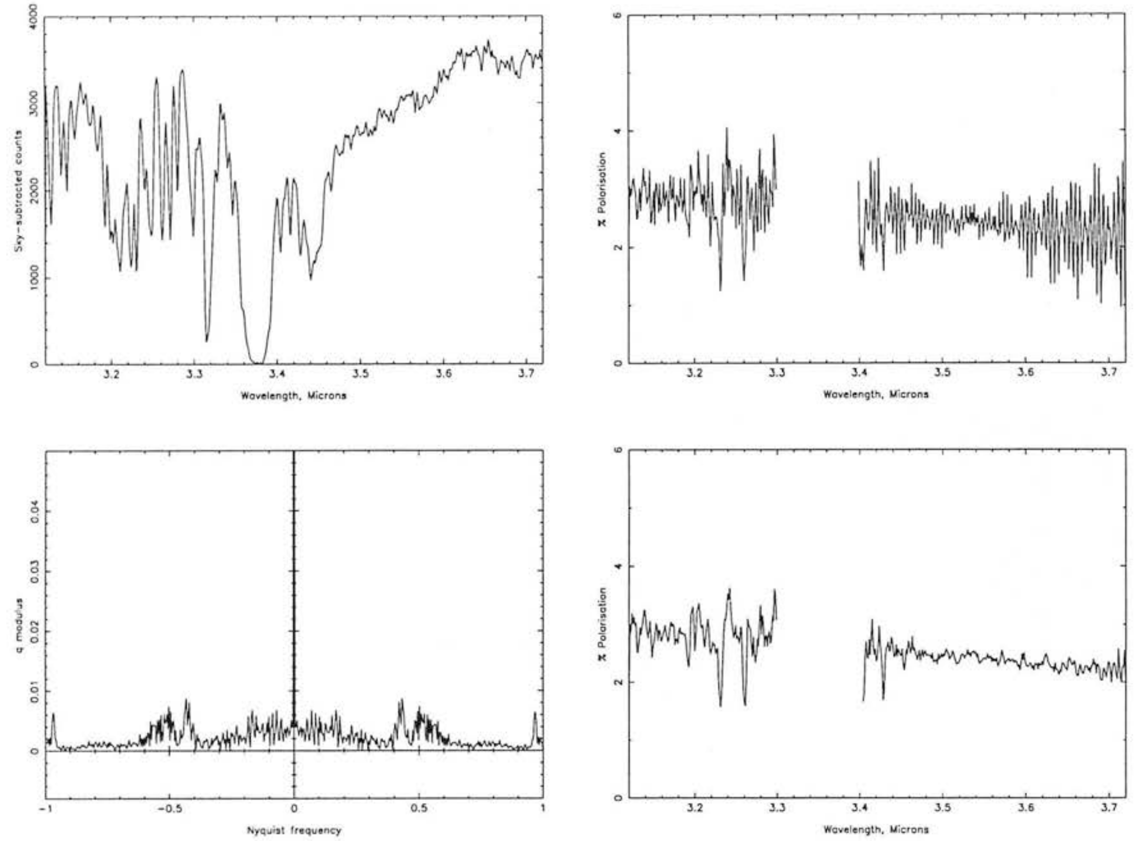

Figure 2.4: Top left: Undivided count spectrum of NGC1068 (cf Fig. 2.15). The obvious absorption band centred at about 3.37μm arises in the cement holding IRPOL2's Wollaston prism together, the sharper feature at about 3.31μm is atmospheric CH_4. Top right: polarisation spectrum of NGC1068, showing the ripple thought to be caused by reflections in the waveplate. Bottom left: Fourier transform of NGC1068's q spectrum. Bottom right: Polarisation spectrum of NGC1068 after the peaks in the FFT are set to zero and the transform reversed.

this ripple was removed using the same FFT technique described by A99. The ripple causes peaks to appear at around 0.5 and 1.0 times the Nyquist frequency in the Fourier transform of the q and u spectra, but if these peaks are set to zero and the transform inverted, the Fourier component corresponding to the ripple is removed. Fig. 2.4 shows the waveplate ripple and the way in which this treatment greatly reduces its amplitude.

UKIRT and CGS4 themselves polarise light to the extent of $\sim 0.5\%$, over and above the astronomical polarisation signal, and this instrumental zero point of polarisation was determined and removed using observations of the G8V star, HD18803. The high proper motion of HD18803 is likely to mean that it is nearby and not seen through a substantial polarising column of interstellar dust. Its low optical polarisation (0.03%, Clayton and Martin, 1981) indicates

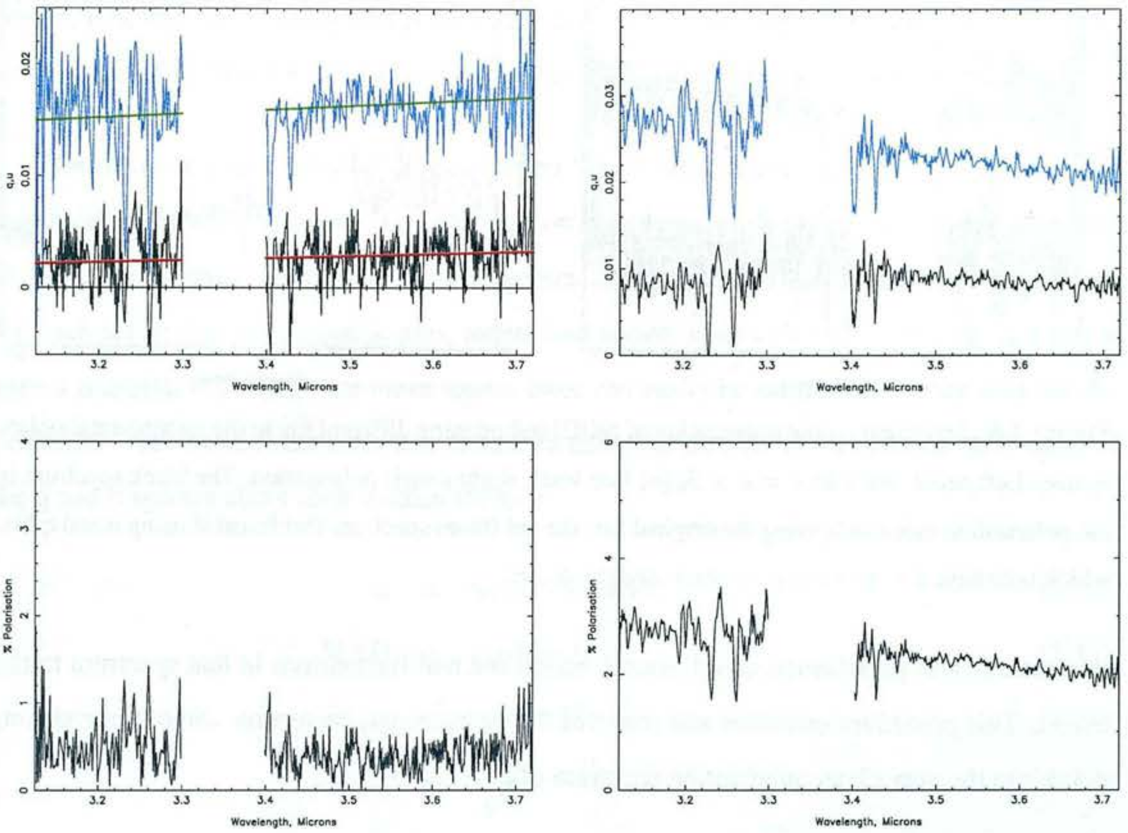

Figure 2.5: HD18803 should be unpolarised, but instrumental effects mean that it is in fact polarised by about 0.5% (bottom left). This was corrected for by subtracting fits to HD18803's q and u spectra (top left) from NGC1068's q and u spectra (top right). Q spectra are shown in black, u spectra in blue; HD18803's u spectrum is offset by 0.015 for clarity. Bottom right: the polarisation spectrum of NGC1068 after correction for this instrumental polarisation.

that dust really is absent from the line of sight, so it should be safe to assume that HD18803 is unpolarised in the near-IR as well. The measured polarisation of HD18803, shown in Fig. 2.5, arises when the light from the star passes through the telescope and instrument, particularly CGS4's diffraction grating, as mentioned in §2.4.1. To correct for this effect, the q and u spectra of HD18803 were subtracted from the q and u spectra of NGC1068 to obtain q and u spectra free of instrumental polarisation; this treatment is adequate when the degree of polarisation is small (Tinbergen, 1996). The observations of HD18803 did not have an extremely high S/N, though, and the noise in the q and u spectra is reflected in increased noise in the resulting polarisation spectrum of NGC1068. This was dealt with by using Figaro's least-squares fitting routine (FITPOLY) to fit straight lines to the q and u spectra of HD18803, and subtracting these fits rather than the q and u spectra themselves. The smoothness of NGC1068's polarisation spectrum before the correction justifies this approach — it is very unlikely that

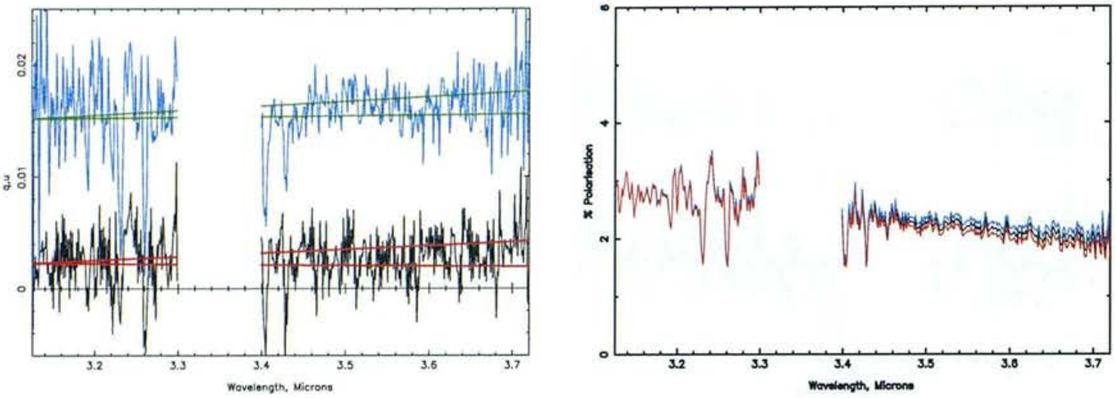

Figure 2.6: The effect on the polarisation of NGC1068 of using different fits to the instrumental polarisation. Left panel: fits with $a = a \pm S_n(a)$ (see text). Right panel: polarisation. The black spectrum is the polarisation calculated using the original fits, the red (blue) spectrum that found if using u and q fits which both have a slope increased (decreased) by $S_n(a)$.

the instrumental polarisation could exactly cancel out real fluctuations in that spectrum to this extent. This procedure estimates and removes the instrumental correction without introducing noise into the very clean polarisation spectrum of NGC1068.

The value and slope of the polarisation after this instrumental correction will depend on the particular fit which is used to represent the instrumental q and u spectra. The slope of the polarisation turns out to be important to the conclusions I draw from these observations, so to investigate this I have calculated the errors on the slope of the fitted line. For a straight line of the form $y = ax + b$, the best estimate of the error of a is given by

$$S_n(a) = n\sigma_n(y)/\{(n-2)[n\Sigma x^2 - (\Sigma x)^2]\}^{\frac{1}{2}} \tag{2.31}$$

where n is the number of data points which have been fitted (Barford, 1967). This formula assumes that the error of measurement of each point is the same, so the mean standard error (see below) over all the points was taken to represent $\sigma_n(y)$. Fig 2.6 shows the fits that would result if $a = \pm S_n(a)$, with the intercept b held constant. The polarisation which would be found if these fits were used to represent the instrumental Stokes parameter spectra was then recalculated. In order to expose the maximum change in slope, the polarisation was reconstructed using first the u and q fits both with an increased a, then both with decreased a. The results are shown in Fig 2.6; it is clear that changing the slope of the fit by the likely error on a has only a very small effect on the slope of the polarisation curve. The intrinsic gradient of NGC1068's u spectrum is much larger than that of the instrumental u spectrum. It is worth noting, too, that the instrumental polarisation is known to be very stable over the timescales over which NGC1068's polarisation was measured (A. Adamson, private communication).

The errors on a measurement of polarisation can be either positive or negative, but polarisation itself is a positive quantity. The polarisation must therefore be "debiased" using estimates of the standard error, σ_n, on the q and u spectra. The method of calculating q and u spectra for each set of four waveplate angles, mentioned above, means that an ensemble of q and u values is available and the root mean square error can easily be estimated. Rather than use the "classical" rms error, σ, the error was estimated using the median of the absolute deviations of the q and u spectra about their median (MAD):

$$\begin{aligned} d_i &= \left|q_i\left(u_i\right) \pm median\left(q\left(u\right)\right)\right| && (2.32)\\ \mathrm{MAD} &= median\left(d\right) && (2.33)\\ \sigma_{q(u)} &\approx 1.48 \times \mathrm{MAD} && (2.34)\\ \sigma_{n,q(u)} &= \frac{\sigma_{q(u)}}{\sqrt{n}} && (2.35) \end{aligned}$$

where n is the number of spectra and $1.48 = \frac{1}{\phi^{-1}(0.75)}$, with $\phi(.)$ the cumulative normal distribution function (Comport et al., 2003).

The advantage of using the MAD rather than directly calculating σ is that the MAD is much less sensitive to extreme values than σ, so gives a more useful estimate of the errors on the q and u spectra for the purpose of debiasing the polarisation. The errors on q and u propagate through to the polarisation:

$$\sigma_{n,p} = \frac{\sqrt{\sigma_{n,q}^2 q^2 + \sigma_{n,u}^2 u^2}}{p} \qquad (2.36)$$

and to the position angle of polarisation:

$$\sigma_{n,\theta} = 28.6^\circ \frac{\sigma_{n,p}}{p}. \qquad (2.37)$$

The polarisation is debiased by

$$p_{debias} = \sqrt{p_{meas}^2 - \sigma_{n,p}^2} \qquad (2.38)$$

In fact, σ_n for NGC1068's q and u spectra was small enough that debiasing made very little difference to the polarisation spectrum.

The final correction to the polarisation spectrum is for the polarising efficiency of IRPOL2's half-wave plate. This is generally $> 90\%$, but varies with wavelength. The L-band wavelength — efficiency relation has been fitted by a second-order polynomial[4]

$$\eta_\lambda(\%) = -398.1 + 272.6\lambda - 37.5\lambda^2. \tag{2.39}$$

The fit is only shown to apply to polarisations at $\lambda \gtrsim 3.5\mu$m, but I have assumed that it is valid for all of our data, which extend down to 3.1μm. This is reasonable because the waveplate is achromatic and designed to work best at the centre of the band. The relative retardation of the e- and o-beams, Δ is given by

$$\Delta = 2\pi(n_e - n_o)/\lambda \tag{2.40}$$

so clearly as the wavelength and the wavelength-dependent refractive indices change, so will the measured polarisation. This effect will have roughly the same magnitude per unit wavelength in both directions (i.e. shortwards and longwards of the design wavelength), so it is justifiable to assume that the fit shown above will apply across the whole of the polarisation spectrum.

The spectrum was corrected for this effect by applying the formula

$$P_{\lambda,corr}(\%) = 100 \times \frac{P_{\lambda,meas}}{\eta_\lambda}, \tag{2.41}$$

which slightly changed the shape of the polarisation spectrum, bringing it to lower values at shorter wavelengths.

Equation 2.39 is an empirical fit to the efficiency, but it would also be possible to use the theoretical efficiency of a zero-order waveplate

$$\eta_\lambda = \sin[(\pi/2)(\lambda_0/\lambda)] \tag{2.42}$$

where λ_0 is the wavelength at which the waveplate is designed to be half-wave. The curves diverge by about 5% at the shortest wavelengths we measure; using the theoretical curve would introduce a very small change in the slope of the polarisation spectrum. This will not affect the conclusions drawn from this work (see §4.1).

---

[4] www.jach.hawaii.edu/JACpublic/UKIRT/instruments/irpol/UIST/specpol.html#4

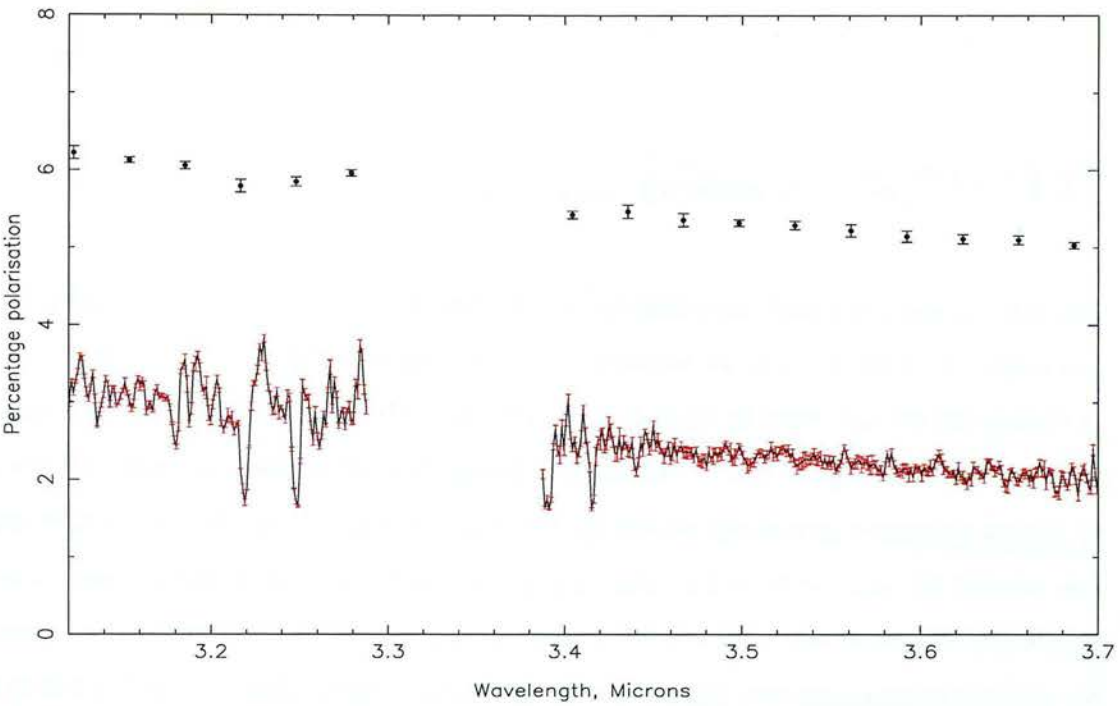

Figure 2.7: The L-band polarisation spectrum (with 1σ error bars) of NGC1068 after correction for waveplate ripple, instrumental polarisation, positive bias and the wavelength dependence of the polarising efficiency of IRPOL2's half-wave plate. The binned spectrum is offset by 3% for clarity.

The polarisation spectrum of NGC1068 after all of these corrections is shown in Fig. 2.7. This spectrum has been moved to the rest frame using the formula

$$\lambda_{rest} = \frac{\lambda_{obs}}{1+z} \tag{2.43}$$

and a redshift of 0.00379 (Huchra et al., 1999).

By sacrificing some wavelength resolution, the S/N of a spectrum can be improved. I have therefore rebinned NGC1068's already very clean polarisation spectrum to lower resolution, a process which must start with the q and u spectra (Tinbergen, 1996). The value of each bin was chosen to be the median of the values contained within it, rather than the mean which would be influenced by any outlying data points. A complication was introduced by the absence of the data at 3.3—3.4μm; bins which would have overlapped this empty region were treated as if they contained only the non-zero data. Starting from the sets of binned q and u spectra for NGC1068, AFGL2591 and HD18803, the polarisation and its errors were reconstructed in exactly the same way as the unbinned polarisation spectrum, with the same corrections and calibration. Any number of bins could have been used, but Fig. 2.7 shows bins which are approximately 0.03μm in width, which strike a balance between smoothing the spectrum and showing enough data points to be informative.

2.4.4 The position angle of polarisation of NGC1068

The position angle of polarisation (PA) can now be calculated using equation 2.19, using the q and u spectra which have had the instrumental q and u spectra subtracted from them (§2.4.3). In finding the PA care must be taken to deal correctly with the arctangent function. Simply taking the inverse tangent of (u/q) would mean losing information about the signs of q and u, so instead a function such as the Fortran intrinsic function ATAN2 must be used, which takes into account the signs of the input values and avoids coming up with a position angle which is 90 ° out. The PA is measured relative to a reference angle within the instrument — usually the analyser transmission axis and the zero-degree angle of the waveplate — so it needs to be calibrated, and the standard calibration procedure is to measure the polarisation of a source whose PA is well-known (Dolan and Tapia, 1986).

We found the position angle calibration factor by determining the difference between our measurement of the position angle of polarisation of the well-studied young stellar object, AFGL2591, and literature values (Aitken et al., 1988). The calibrated position angle of NGC1068, Θ, is then

$$\Theta_{NGC1068,corr} = \Theta_{NGC1068,meas} + (\Theta_{AFGL2591,lit} - \Theta_{AFGL2591,meas}) \qquad (2.44)$$

However, the ripple in the spectra of AFGL2591 was pronounced and variable, and I was unable to remove it using either the FFT technique described in §2.4.3 or the Figaro routine IRFLAT, which can determine the amplitude and period of ripple in a spectrum. Calibrating NGC1068's PA with this spectrum would have introduced a lot of noise. Instead, the q and u spectra of AFGL2591 were fitted with straight lines and the PA spectrum recalculated using these fits. Fig. 2.8 shows both the "raw" PA spectrum of AFGL2591 and that calculated using the fits to the q and u spectra. This fitted spectrum was then used to calibrate NGC1068 using equation 2.44.

We measured a value of approximately 85° for AFGL2591, against Aitken et al.'s figure of 170 °and a figure of about 38 ° for NGC1068 (Fig. 2.8). The correction to NGC1068's position

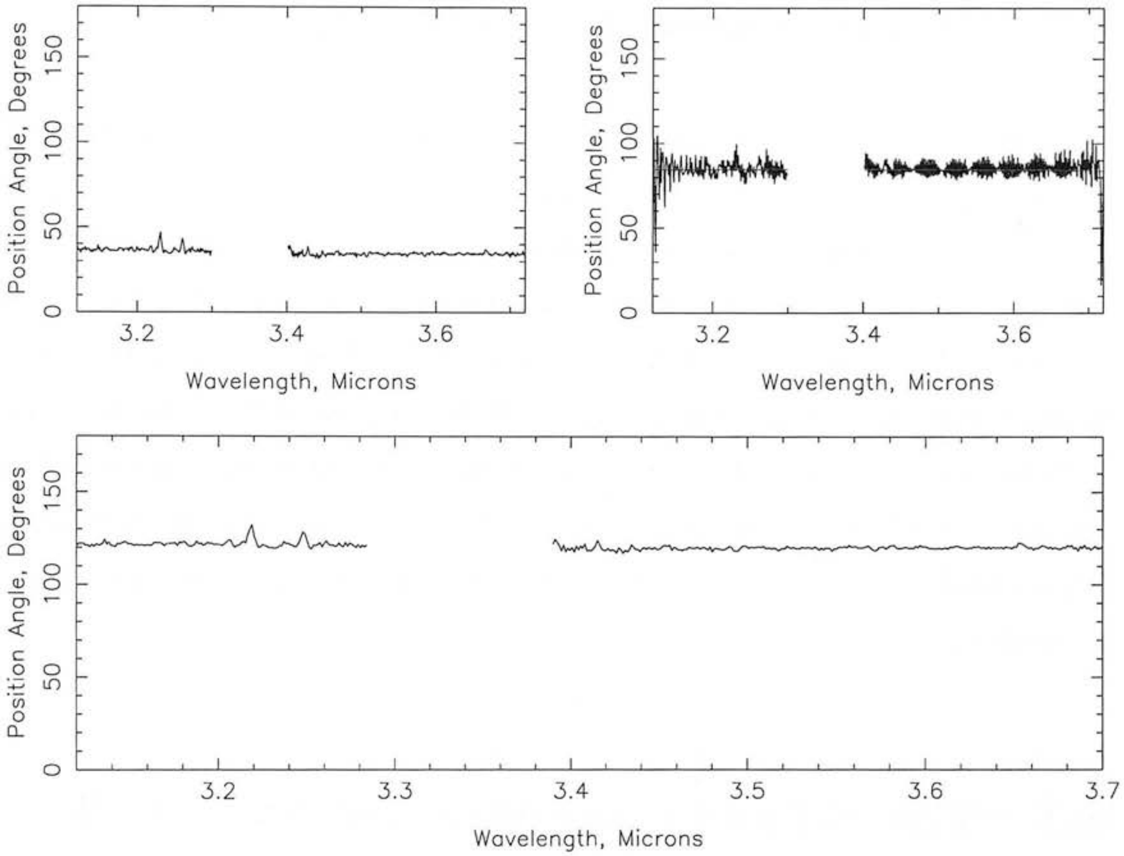

Figure 2.8: Top left: position angle of polarisation of NGC1068, uncalibrated. Top right: the measured position angle of the polarised standard star, AFGL2591. The red line shows the PA of AFGL2591 calculated from straight-line fits to its q and u spectra, thereby removing the ripple in the spectrum. Bottom panel: NGC1068's position angle, calibrated with reference to AFGL2591 and corrected for the galaxy's redshift.

angle of polarisation was therefore about 85°, bringing it to around 120°, in good agreement with published measurements (Bailey et al., 1988). At a later date I also observed and examined the polarisation and position angle of the young stellar object, W33A. The depth of the 3.1μm ice absorption band and resulting noise in the polarisation at $< 3.5\mu$m meant that this object could only be used as a rough check, but in the part of the spectrum at wavelengths $> 3.5\mu$m, the same approximately 85° alteration was required,

2.4.5 Comparisons with existing observations

Spectropolarimetry of NGC1068 around 3μm has been carried out by Bailey et al. (1988), who report polarisations of 3.44±0.52, 2.71±0.32 and 2.29±0.18% at 3.16, 3.45 and 3.8μm respectively. The position angles of these measurements are 127±4, 120±3 and 119±3°. Lebofsky et al. (1978) have also measured the polarisation of NGC1068 at 3.45μm, finding its degree and position angle to be 2.7±0.2% and 125±2°. These values, and the trend of polarisation decreasing with wavelength, agree quite well with this current work. Differences in aperture size and the fact that the previous observations were carried out using a single-beam system (and therefore have larger errors — see §2.5.1) may account for the small discrepancies. Our measured position angle of polarisation is quite steady at about 120°across the band, again in agreement with Bailey et al. (1988) within the errors.

2.5 The N-band polarisation of NGC1068

As described in §2.1, if a measurement of the polarisation over the 3.4μm C-H bond stretch is to be interpreted in a simple way, it is also necessary to know the behaviour of the polarisation over the 10μm silicate feature. The N-band polarisation of NGC1068 has been studied before, but the only spectropolarimetric data, although suggestive of an increase at 10μm, is too noisy to be considered a reliable detection (Aitken et al., 1984). As well as that, the 4″aperture used was considerably larger than the 0″.61 CGS4 slit we have used to measure the 3.4μm polarisation and could therefore sample quite different regions of dust. In an attempt to better determine the N-band polarisation properties of the dust in NGC1068 we have carried out spectropolarimetry of this galaxy with the new mid-IR imager and spectrometer, Michelle, the first such observations performed using this instrument.

2.5.1 Single-beam polarimetry: Michelle

The mid-IR analogue of the Wollaston prism does not yet exist, so polarimeters operating at these wavelengths tend instead to rely on a wire grid analyser. This introduces some differences to the measurement of the polarisation. The principle remains the same, to measure differences in intensity between the orthogonal polarisation planes (eg. equation 2.24). This time, though, the orthogonal beams are not in the form of e- and o-beam spectra separated by the Wollaston prism and measured simultaneously. Instead, the waveplate is rotated through 0°, 22.5 °, 45 °and 67.5 °, equivalent to analyser positions of 0°, 45 °, 90 °and 135 °.

The Stokes parameters are then given (in terms of the *waveplate* positions) by

$$q = \frac{q1 - q2}{q1 + q2} \tag{2.45}$$

$$= \frac{i_0 - i_{45}}{i_0 + i_{45}} \tag{2.46}$$

$$u = \frac{u1 - u2}{u1 + u2} \tag{2.47}$$

$$= \frac{i_{22.5} - i_{67.5}}{i_{22.5} + i_{67.5}} \tag{2.48}$$

The main drawback with this arrangement is that time has elapsed between the measurement of the intensities from which are derived the Stokes q and u spectra. Variations in sky background, tracking, in fact anything which varies over time and affects the measured intensities, now becomes an important factor.

2.5.2 Observations and data reduction

Spectropolarimetry of NGC1068 from $8 - 13\mu$m was obtained on the nights of 2001 October 10th[5] & 19th using the mid-IR spectrometer and imager, Michelle, on UKIRT. The weather was good on the first night but less good with some cirrus on the second. The silicate feature is broad, extending from about $8 - 13\mu$m (e.g. Dudley and Wynn-Williams, 1997, see also Fig. 2.18), so these observations used the Low-N grating, which gives wavelength coverage of 7.7μm. Although the feature is centred at about 9.7μm, centring the grating at that wavelength would mean that the short-wavelength end of the spectrum would include regions outside the atmospheric N-band window. To avoid this wastage, we instead centred the grating at 11μm.

When used with the 2-pixel-wide slit, the Low-N grating gives a spectral resolving power of ~200, and this was the slit width used on the first night. The plate scale of Michelle in this

---

[5] data kindly provided by A. Glasse and T. Kerr

configuration is 0".18/pixel in the spatial direction. As for the L-band observations, the slit was orientated N-S. As the sky background is so bright at these wavelengths, all observations were carried out using the background-limited exposure time of 0.11s. On the first night 2x1 sampling was used, but when the weather deteriorated on the second night we switched to 1x1 sampling. This has the disadvantage that bad columns on the array always fall at the same wavelength in the spectrum, but it also means that less time elapses between telescope nods, reducing the impact of the varying sky background.

When observing at shorter IR wavelengths, nodding of the telescope so that the "sky" and "object" beams are interchanged a few times a minute is sufficient to cancel out gradients in the sky background and differences due to the different optical paths taken by the two beams through the telescope. The remaining background can be subtracted using the parts of the array containing only blank sky. In the mid-IR, on the other hand, the sky background varies quickly and irregularly over the field and nodding alone is not sufficient to cleanly subtract it. This is overcome by "chopping", moving the secondary mirror to look at blank sky at a frequency of several Hz. On our second night of observing NGC1068, we encountered some difficulties with the piezo-electric actuators which control the secondary mirror during chopping. This meant that we had little control over the size or direction of the chop throw and found that the chop beam sometimes fell out of the slit. To minimise the chances of this happening, we opened the silt to its maximum 8-pixel width. Although this meant that we were more likely to observe the chop beam, the slit being four times wider degraded the resolution by about the same factor, giving a resolving power of only ~ 50.

The Stokes parameters were obtained by taking frames at eight waveplate positions, 0°, 22.5 °, 45 °and 67.5 °, and (on 20011019 only) 180°, 202.5 °, 225 °and 247.5 °. As the observations presented here were the first Michelle polarimetry observations, the second set of angles was used to show up any systematic errors which may have been present due to irregularities in Michelle's waveplate (Fig. 2.9 shows that no obvious errors were in fact detected). The initial reduction of the raw data was performed using the ORACDR recipe, POINT_SOURCE_POL. This script begins by applying the recipe REDUCE_SINGLE_FRAMES (see § 2.4.2) and then goes on to add the observations into groups at each waveplate angle, subtract the chopped and nodded frames and extract spectra from them. In fact, the later steps of this routine require a different version of FIGARO than the version to which was then installed at the ROE, so the sequence was terminated once the nodded frames had been subtracted, leaving frames containing four object spectra.

Michelle's polarimeter is integral to the instrument and contains no beam-splitting prism, so there is no requirement that the slit be orientated at any particular angle to the array. Consequently there is no need to correct for slanted sky lines, as was the case for our IRPOL2 observations. The next step in the data reduction was then to subtract any residual sky background, using POLYSKY as described for the CGS4 data. Although there was much more background to subtract at this wavelength, it was often quite effectively removed. As for the L-band data, the spectra were then optimally extracted.

As a check on the sky subtraction, however, a cut through each frame in the spatial direction was displayed, contrasting the data before and after sky subtraction. This showed that the background level in some of the frames was far from zero, and some were very weak detections of NGC1068. These faults were dealt with by calculating the median level of the data in each optimally extracted spectrum over pixels known not to contain sky lines or bad columns, and plotting these data against the waveplate angle (Fig. 2.9). This clearly revealed the deviant frames, which could then be discarded. A total of 12 out of 42 waveplate cycles were rejected.

The wavelength calibration of the data was carried out using observations of sky lines rather than an arc lamp. These observations used the Low-N grating centred at 11μm, so the wavelength coverage of 0.0258μm/pixel (A. Glasse, private communication) over Michelle's 320×240 pixels means that the observations span the range of $6.872 - 15.128\mu$m. A section of a model N-band sky spectrum (generated from the HITRAN database of atmospheric species using the FASCOD programme; Clough et al., 1981) was extracted over these wavelengths, rebinned to 320 elements, and this wavelength scale copied onto a sky spectrum extracted from a frame from before sky subtraction. The shift between the observed and model spectra was then determined (using SCROSS), and the wavelength scale shifted to account for this. The shift differed very little between the two nights (being 17 pixels on 20011010 and 19 pixels on 20011019), and given the low spectral resolution of most of the data, this difference was ignored. Inspection of the model and observed spectra now showed that all of the atmospheric features lined up very well, so the final wavelength scale was then simply copied onto the polarisation and flux spectra.

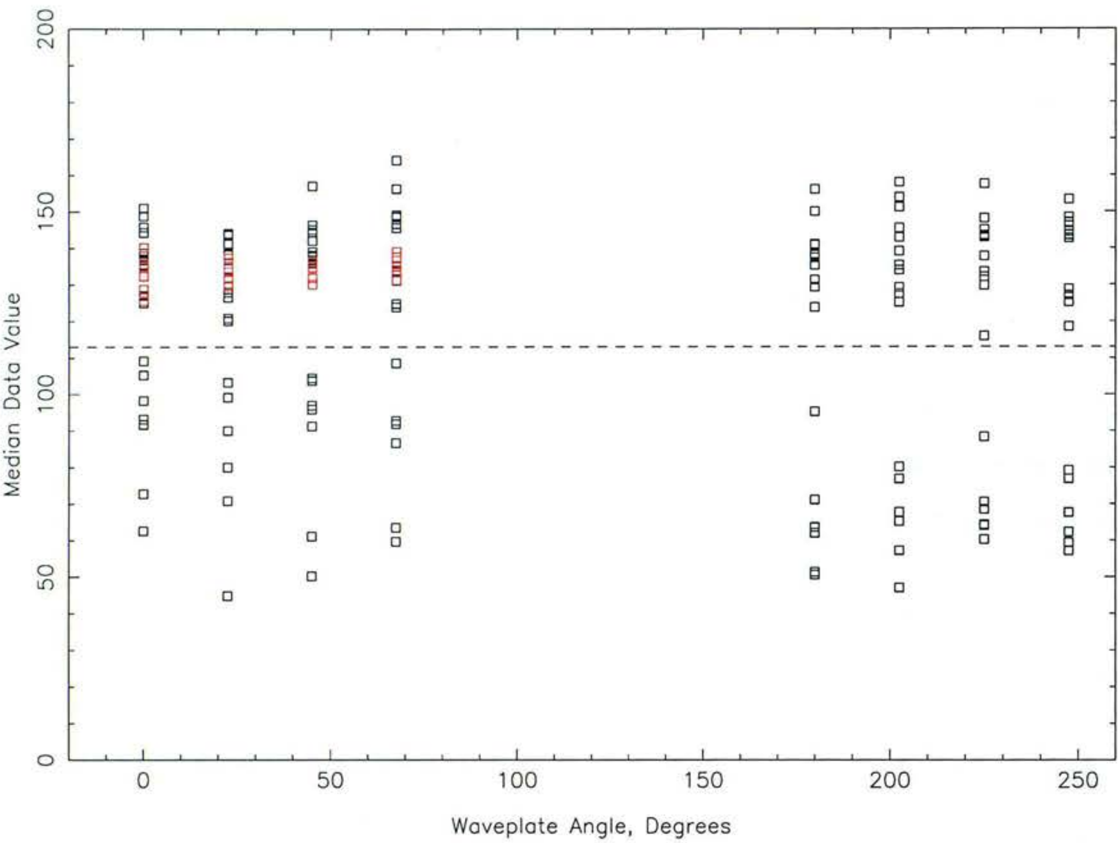

Figure 2.9: Choosing observations to keep or reject. When inspected, the frames below the dashed line all had problems with sky subtraction or simply did not detect the target. If a frame was found to be defective at one waveplate angle, it generally was at all the others, too. Black data points are from the night of 2001119, red from 20011010.

An unpolarised standard star, BS1713 (Rigel), was also observed on 2001 October 19th in the same manner as NGC1068. For position angle calibration, spectropolarimetry of the Becklin-Neugebauer (BN) object was performed on 2001 October 9th[6]. The instrumental setup was as described for 2001 October 10th, and weather conditions were also similar to those on that night. The data for both standards were reduced in the same way as the NGC1068 data.

2.5.3 The N-band polarisation of NGC1068

The N-band polarisation spectrum of NGC1068 and the standards could now be calculated directly from the set of optimally-extracted spectra using equations 2.46, 2.48 and 2.18. The

---

[6] these data also provided by A. Glasse and T. Kerr

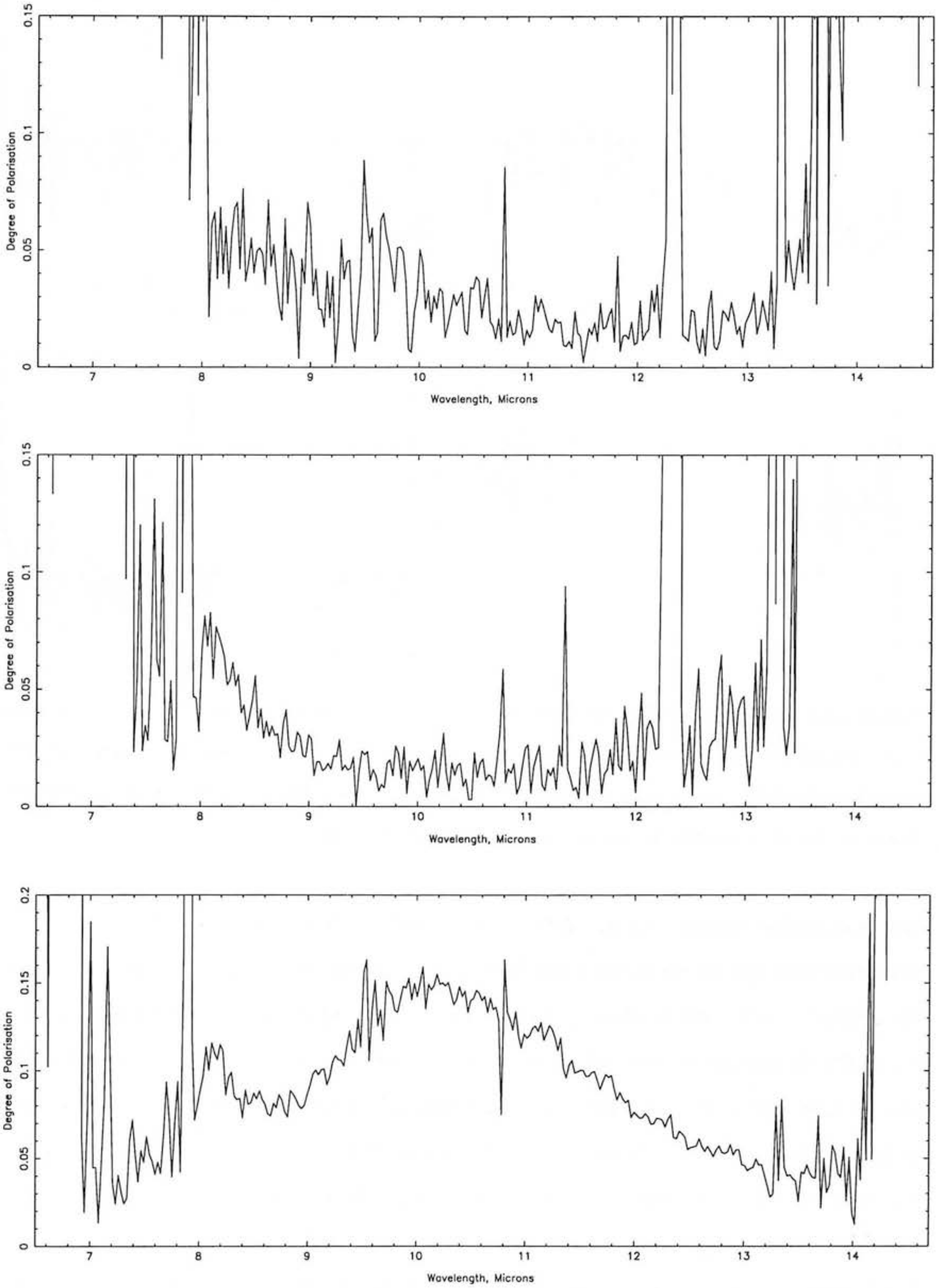

Figure 2.10: Raw polarisation spectra of NGC1068 (top), Rigel (centre) and the BN object (bottom). All spectra show the deterioration of the N-band atmospheric window at their edges, as well as a rise or peak around 8.2μm. Particularly prominent in NGC1068's polarisation spectrum, but also seen in that of the BN object, is noise just shortwards of 10μm, over the telluric O_3 absorption. Also visible in the spectra of NGC1068 and Rigel are peaks at 12.3μm, caused by bad columns on Michelle's detector.

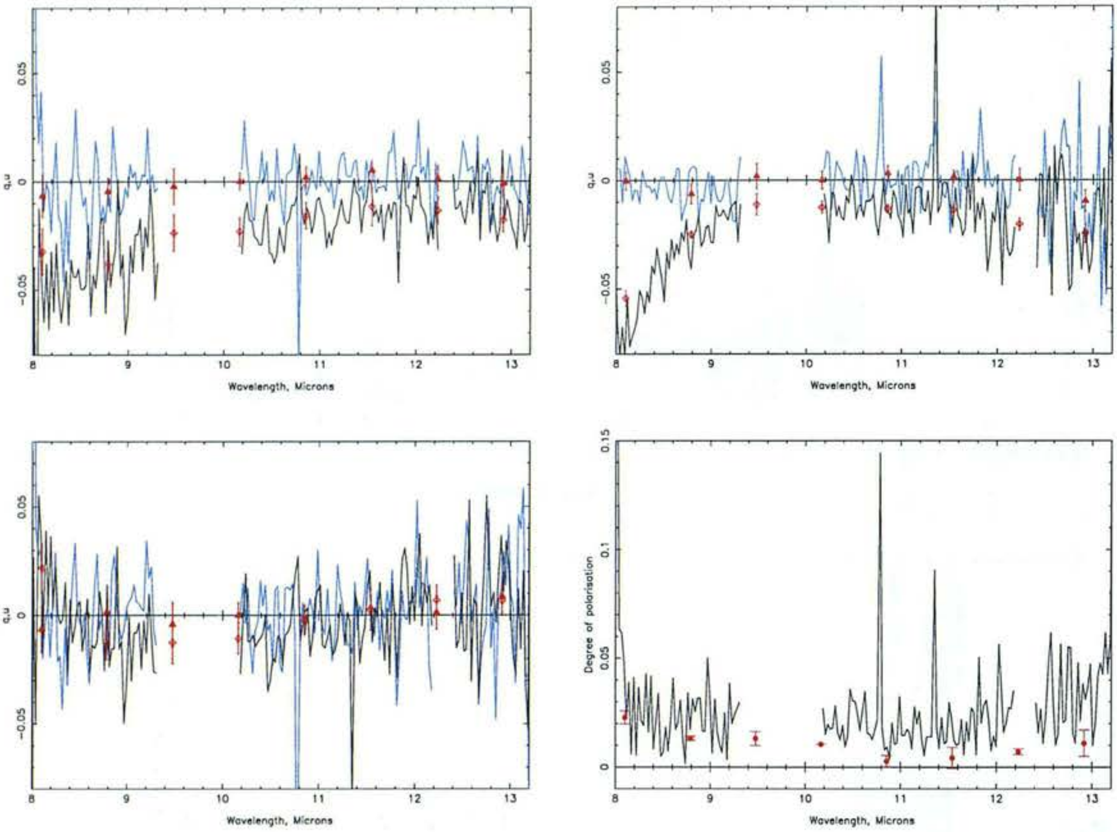

Figure 2.11: Top left: the q (blue) and u (black) spectra of NGC1068, from which are subtracted the q and u spectra of Rigel (top right). Also shown are the same spectra binned to lower resolution (red). The lower left plot shows the q and u spectra of NGC1068 after this subtraction. The resulting spectrum, now corrected for instrumental polarisation, is in the lower right panel.

raw polarisation spectra obtained using this method are shown in Fig. 2.10. Several points concerning the spectra should be made here. Firstly, the spectra deteriorate considerably near the edges of the N-band window. and these regions are simply discarded in subsequent plots. Secondly, the spectra of NGC1068 and the BN object show a small peak between about 9.3 and 10.1μm. This coincides with the wavelength of a deep atmospheric ozone absorption, indicating that it is an artefact due to imperfect cancellation of that line. This being so, this region of the spectra was set to zero before proceeding any further. Another obvious feature of the NGC1068 and Rigel data is a very strong and narrow peak around 12.3μm. This is due to bad columns on Michelle's array and would be less prominent had we not had to take most of the data for these objects using 1×1 sampling. This small region was also removed from the data.

A further feature of the data is a rise or peak in the polarisation at about 8.2μm. This is

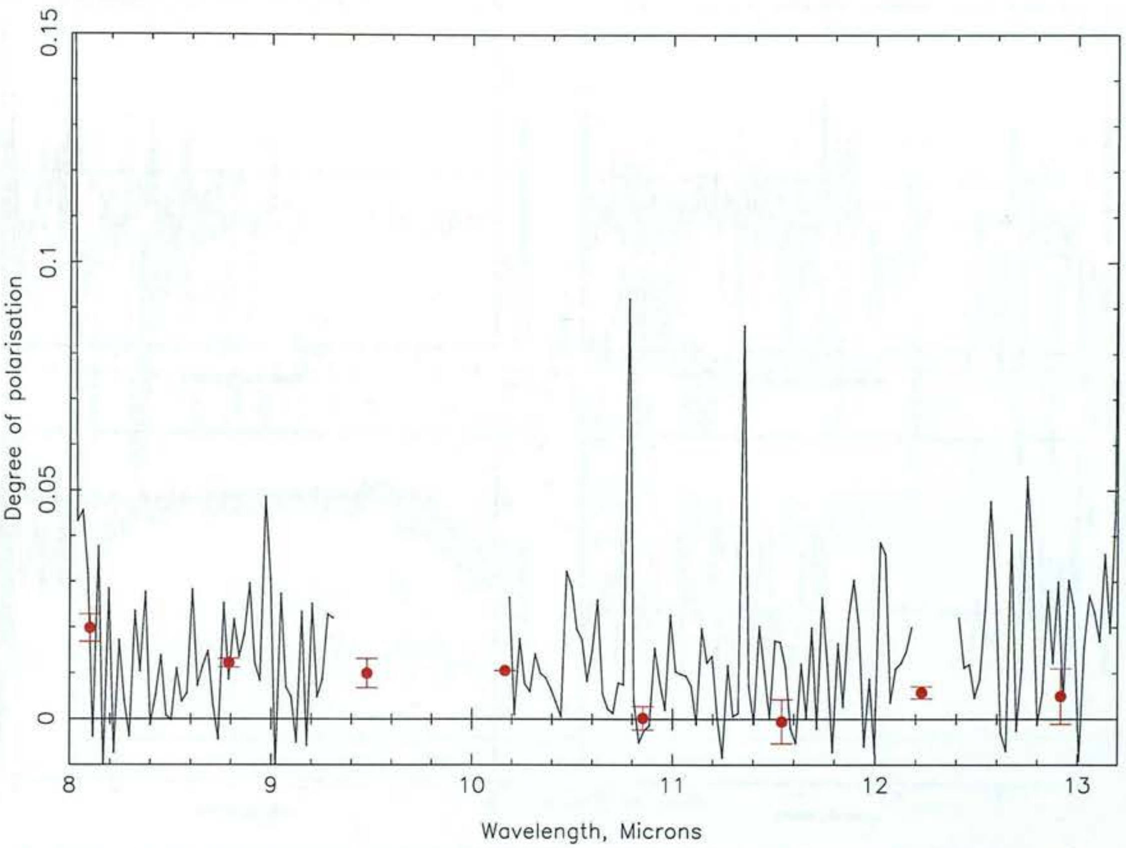

Figure 2.12: NGC1068's N-band polarisation spectrum after correction for statistical bias.

seen in the spectra of all the objects, indicating that it is an instrumental effect and illustrating the need for further treatment of the data. In exactly the same manner as for the L-band data, the instrumental polarisation was determined and removed using observations of the unpolarised standard star, Rigel. This process is shown in Fig. 2.11. The top two plots in the figure show that the q and u spectra of NGC1068 and the standard star are very similar, suggesting that rather than detecting polarisation from the galaxy, we have simply measured the instrumental polarisation. Indeed, when the standard's q and u spectra are subtracted from those of NGC1068, the q and u spectra become very close to zero. However, the q and u spectra are noisy enough that a polarisation of about 2% is found when the polarisation is recalculated after this instrumental correction. This procedure has the effect of removing the 8.2μm rise in the NGC1068 polarisation, whilst shifting it to higher values at the long-wavelength end of the spectrum. As for the $3-4\mu$m data, the polarisation was then debiased by subtracting in quadrature the standard error on the polarisation.

To reduce the noise in the q and u spectra and thus get a better measurement of the polar-

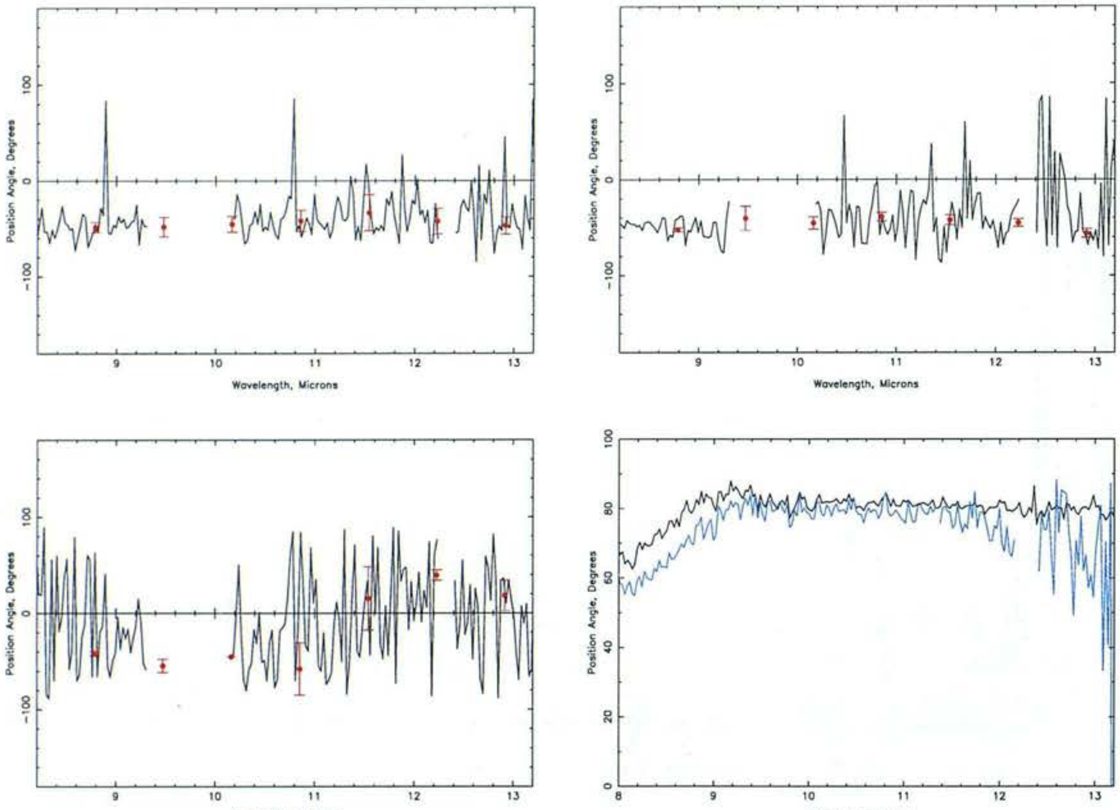

Figure 2.13: The position angle of polarisation of NGC1068. Top left: as measured. Top right: the observed position angle of the unpolarised standard star, Rigel. Bottom left: the position angle of NGC1068 after the instrumental contribution has been removed. Bottom right: the position angle of the BN object before (black) and after (blue) removal of the instrumental polarisation.

isation, the spectra were binned in the same manner as the L-band data. The binned data are also shown in Fig.2.11. The binned points clearly follow the raw q and u spectra very well, but when Rigel's q and u parameters are subtracted from those of NGC1068, the points become noticeably closer to zero. This has the effect of reducing the final measured polarisation of NGC1068 (lower right panel). In the limit where the entire q and u spectra from 8.2-13.2μm (discounting the parts set to zero) are placed into one bin (i.e. their median is taken), and the de-biased polarisation recalculated, a value of 0.17±0.33 is measured. This strongly suggests that, rather than measuring polarisation intrinsic to NGC1068, we have observed only polarisation due to the telescope and instruments themselves.

For completeness, the raw position angle of polarisation of NGC1068 and the standard stars was calculated using equation 2.19. Fig. 2.13 illustrates that, as in the case of the q and u parameters, the PA of NGC1068 and the unpolarised standard bear a strong resemblance

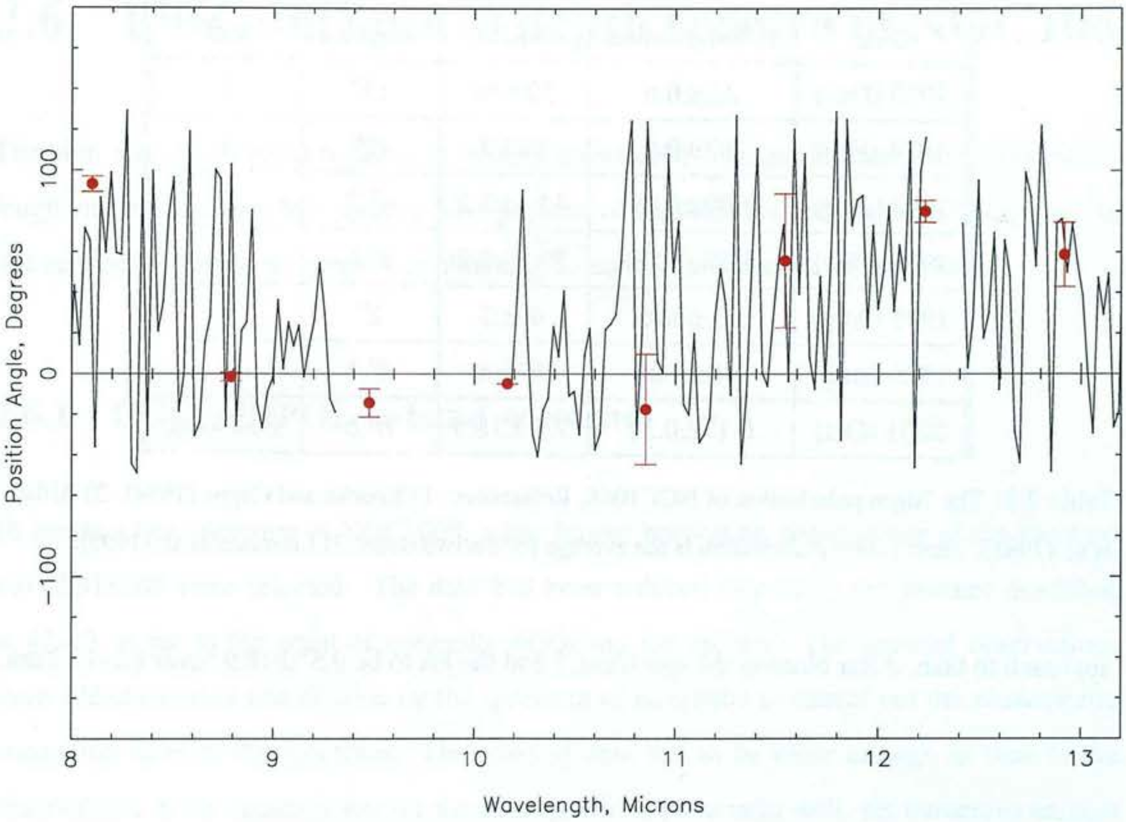

Figure 2.14: The position angle of NGC1068, calibrated with reference to the BN object.

to each other. Again, this implies that we are measuring mainly instrumental polarisation, so the PA of NGC1068 was reconstructed using its q and u spectra after those of Rigel had been subtracted off them. The result, also shown in Fig. 2.13, is very noisy, ranging from about -90 °to +90 °across the spectrum. In an attempt to reduce the noise on the PA, rather than using using the actual q and u spectra of Rigel to remove the instrumental contribution to the position angle, polynomial fits to Rigel's q and u spectra were used. However, the principal source of the noise is the fact that the q and u parameter spectra of NGC1068 are noisy enough that they frequently cross zero even when these fits are subtracted off them. This leads to the PA flipping wildly when the inverse tangent of u/q is taken, and using these fits does not result in any improvement.

The PA of NGC1068 was calibrated using the observed position angle of the BN object (Fig. 2.13). The position angle of the BN object in the N-band is 120° at 8-9μm, decreasing slightly with wavelength after that (Aitken et al., 1989), whereas we measure a position angle of approximately 80°. NGC1068's PA was therefore calibrated by simply adding 40° to each pixel in the spectrum (Fig.2.14); given the large amount of noise in the data, this is a reasonable

Date	% Polarisation	Angle	Aperture	Ref
1973 (Dec)	2.2±0.6	52±16	12″	1
1974 (Feb)	2.3±0.5	84±7	12″	1
1983 (Aug)	1.39±0.09	44.1±3.2	4″.2	2
1983 (Dec)	1.39±0.09	59.4±2.2	5″.6	2
1995 (Aug)	1.3±0.05	49±3	2″	3
1995 (Aug)	1.8±0.05	57±6	4″.5	3
2001 (Oct)	0.17±0.33	9.5 ±18.9	0″.6	This work

Table 2.2: The 10μm polarisation of NGC1068. References: 1) Knacke and Capps (1974). 2) Aitken et al. (1984). Their 1.39% polarisation is the average for the two dates. 3) Lumsden et al. (1999).

approach to take. After binning the spectrum, I find the PA to be 9.5°±18.9 °over 8.2-13.2μm.

2.5.4 Comparisons with existing observations

Measurements of the N-band polarisation of NGC1068 go back as far as 1974, and are summarised here in table 2.2.

The large errors on the polarisation and the poor measurement of its position angle, together with the clear inconsistency with previous measurements, indicate that we have not been able to improve on the published data, the aim of this work. That the degree and direction of polarisation are not well-determined is not surprising, given the less-than optimal weather conditions, the telescope fault on the second night and the fact that the weather conditions meant that significantly less time was spent on taking data than had been allocated to us. I conclude that, even if these data genuinely reflect the polarisation of NGC1068, they cannot be used even to pin down the value of the 10μm polarisation and position angle of NGC1068. They certainly do not permit an accurate determination of the size of any increase in polarisation over the 9.7μm silicate feature, as was hoped. Fortunately for this project, some calculational techniques developed in recent years mean that this turns out not to be crucial to the interpretation of the L-band polarisation; but more of that in Chapter 3.

2.6 Flux and optical depth spectra of NGC1068

The high S/N observations required to reliably detect small changes in polarisation with wavelength mean that a very high-quality flux spectrum of the source is simultaneously acquired. In this section I describe the process of obtaining L- and N-band spectra of NGC1068.

2.6.1 CGS4+IRPOL L-band spectrum

To create a flux spectrum of NGC1068, a few frames bracketing observations of the standard star HD18803 were selected. The data had been reduced in exactly the manner described in §2.4.3 as far as the point of optimally extracting the spectra. The selected observations were added together and divided by the spectrum of HD18803 to cancel out the atmospheric absorption lines in the spectrum. The selected data had to be close enough in time to the observations of the standard star for the atmospheric lines to ratio well, yet numerous enough that good S/N was obtained. The appropriate balance was found simply by trial and error; the number of observations of NGC1068 used to create the flux spectrum was varied until a spectrum was obtained which was both free of telluric lines and had high S/N.

The resulting spectrum was flux-calibrated with reference to the G8V-type standard star, HD18803. The star's V magnitude was converted to a magnitude at 3.45μm using V-K and K-L colours appropriate to this spectral type[7], and this L-band magnitude into flux density. As the spectrum of NGC1068 had been divided by that of the standard, it was then multiplied by the flux density of the star to give a spectrum in units of $\mathrm{Wm^{-2}\mu m^{-1}}$. This spectrum, shown in Fig. 2.15, has a flux density of approximately $6 \times 10^{-13}\,\mathrm{Wm^{-2}\mu m^{-1}}$ at 3.45μm, comparable to the $7 \times 10^{-13}\,\mathrm{Wm^{-2}\mu m^{-1}}$ measured by Imanishi et al. (1997) at this wavelength.

For comparison with literature spectra of the 3.4μm absorption feature, the flux spectrum was converted to an optical depth spectrum using the equation

$$I(\lambda) = I_0(\lambda)e^{-\tau(\lambda)} \qquad (2.49)$$

The flux in the continuum underneath the absorption feature, $I_0(\lambda)$, must be estimated by

---

[7] available at www.jach.hawaii.edu/JACpublic/UKIRT/astronomy/temp.html

fitting a curve through the data around the feature. A good fit to the continuum is provided by a third-degree polynomial curve, shown in Fig. 2.15. This is physically reasonable, as the 3.4μm feature is though to be caused by cool dust absorbing the IR continuum radiated by warm dust closer to the nucleus, which will have a roughly blackbody spectrum. The third-degree continuum fit can be reproduced by a combination of three blackbody spectra, at various temperatures and variously reddened (A. Adamson, private communication).

The optical depth spectrum of the 3.4μm feature in NGC1068 is shown in Fig. 2.15. As the flux and optical depth spectra were derived from data taken with IRPOL2 in the beam, they show the same strong absorption features as described in §2.4.3. The 3.3-3.4μm region has therefore been removed, as before. The remainder of the band shows two of the subfeatures characteristic of the 3.4μm absorption - the CH_2 asymmetric stretch at 3.42μm and the CH_3 symmetric stretch around 3.48μm. On closer inspection, though, the profile of the 3.4μm feature presented in Fig. 2.15 is quite different from that observed in many other lines of sight. In particular, the peak at 3.42μm is stronger than usual relative to the shoulder at about 3.48μm. However, the peak of the feature coincides with a fairly broad and deep atmospheric absorption band (visible in Fig. 2.4). At this resolution this band is often split into distinct H_2O lines (see e.g. A99), but a high water column density could mean that the lines strengthen and blend together. It is possible that the 3.42μm peak of the feature is exaggerated by incomplete removal of this feature during division by the standard star. Additionally, the presence of IRPOL in the beam means that some parts of the feature cannot be examined at all. For these reasons we have taken advantage of the commissioning of UKIRT's new imager/spectrometer, UIST, to acquire another spectrum of this band in NGC1068.

2.6.2 UIST L-band spectrum

Spectra of NGC1068 and a standard star (HD16970, A3V) were obtained on 2002 November 9th as part of the UKIRT Service Programme. The objects were observed using UIST's short-L grism and a 4-pixel-wide slit, a combination which gives a spectral resolution of $\lambda/\Delta\lambda \approx 650$ and a wavelength range of about 2.9-3.6μm. Background-limited exposure times of 11s were used, along with a nod offset of $12''$ and slit position angle of 90°.

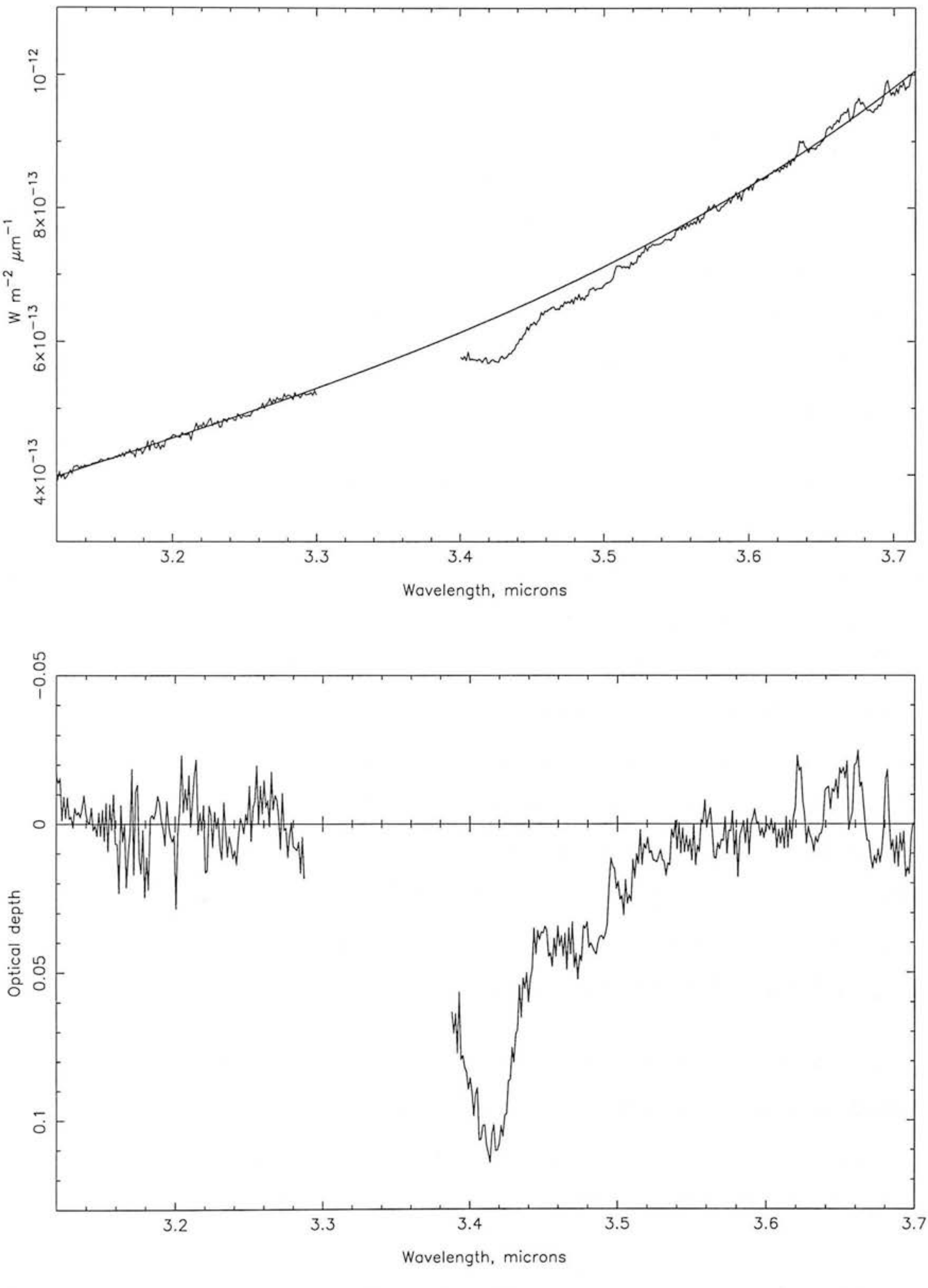

Figure 2.15: Top: flux spectrum of NGC1068 showing the fitted continuum and the good cancellation of the atmospheric absorption lines. Bottom: the optical depth of the 3.4μm feature in NGC1068 (rest frame).

The data were reduced using the ORACDR data reduction pipeline. The NGC1068 data used the recipe "POINT_SOURCE", while the standard star observations were reduced using "STANDARD_STAR". Both of these recipes start by using the "_REDUCE_SINGLE_FRAME_" primitive, described in §2.4.2, to get as far as sky and object frames with an estimated wavelength scale. The sky and object pairs are then added into groups. Spectra of the target are extracted from the group images, cross-correlated, and added together. The spectra of the standard star and the target are aligned, and the target spectrum divided by the standard to cancel out atmospheric absorption lines. In practice, I found that a slightly cleaner spectrum was obtained if I cross-correlated the star and galaxy spectra outside the pipeline, shifted the galaxy spectrum and then divided by the standard.

Observations of an argon arc lamp were provided for wavelength calibration. However, as the optics in the calibration unit are themselves quite bright in the L-band, the arc lamp is instead observed through the J- or H-band filter in second order. The refractive index of these filters introduces a wavelength shift to the observed arc lamp lines, meaning that the wavelength scale derived from the arc spectrum is incorrect. Instead the NGC1068 data were wavelength-calibrated using HI lines in the Pfund series. These lines, marked with arrows in Fig. 2.16, are found in the spectrum of the A-type standard star and show up clearly in the spectrum of NGC1068 once it has been ratioed with that standard[8]. The HI lines were used to calibrate the wavelength scale by using the Figaro ARC command in the same way as in §2.4.2, and the corrected wavelength scale copied onto the NGC1068 spectrum. Flux calibration then proceeded as described in §2.6.1, yielding a flux density in good agreement with both the CGS4 spectrum in Fig. 2.15 and that of Imanishi et al. (1997).

As in §2.6.1, the ratioed, wavelength-calibrated spectrum of NGC1068 can now be transformed into an optical depth spectrum. As we have only data taken with UIST's short-L grism, the spectrum does not include much continuum on the long-wavelength side of the feature. However, the optical depth spectrum presented in Fig. 2.15 suggests that the feature extends

---

[8] Marco and Brooks (2003) attribute emission lines in their L-band spectrum of NGC1068 to PAHs and MgVIII ions intrinsic to that galaxy. However, their detection of the 3.28μm PAH line is tentative at best, and the 3.028μm MgVIII line lies very close to and could easily be partially masked by the 3.039μm Pfund series line. This, together with the match in relative positions and intensities of the emission lines in Fig. 2.16 with H emission lines, suggests that my identification of these lines is quite safe.

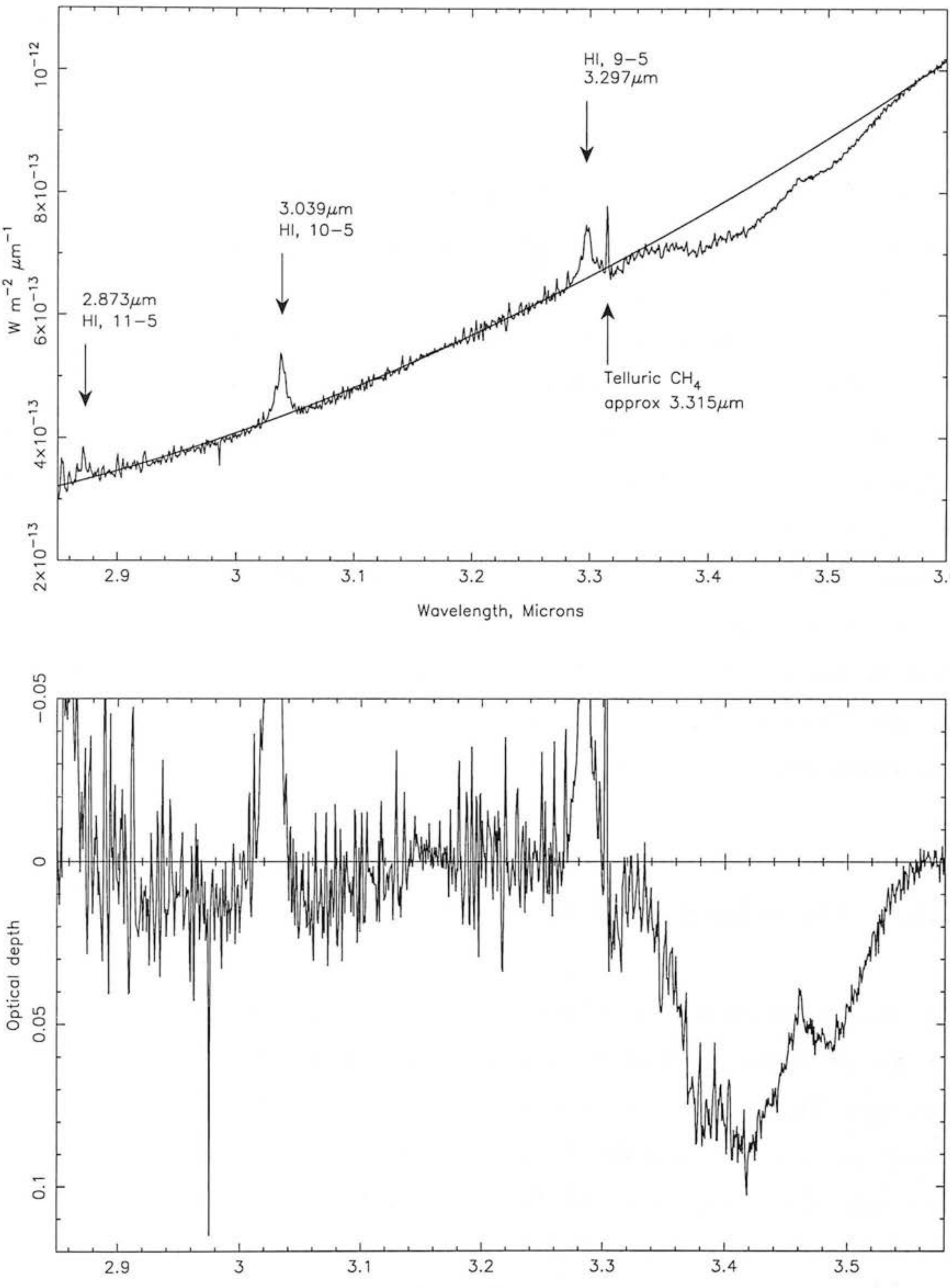

Figure 2.16: UIST flux and optical depth spectra of the 3.4μm band, taken without IRPOL in the beam. Top: flux and fitted continuum. Also shown are the identifications and emitted wavelengths of the emission lines in the spectrum. The line labelled "Telluric CH$_4$" is a badly-cancelled atmospheric absorption band. Bottom: rest frame optical depth spectrum. Line identifications taken from www.jach.hawaii.edu/JACpublic/UKIRT/astronomy/calib/pfund.html.

from approximately 3.3μm to about 3.58μm (rest wavelengths). As for the CGS4+IRPOL data, then, a third-degree polynomial fit was performed to the data points outside this range. The continuum fit, and the resulting optical depth spectrum, are shown in Fig. 2.16

Fig. 2.17 compares the CGS4+IRPOL and UIST spectra. That the two spectra match up well in the 3.54-3.58μm region indicates that the continuum used to derive the new optical depth spectrum was appropriate, despite the lack of data points to fit to at that end of the spectrum. The extended wavelength coverage of the UIST spectrum also confirms that the nucleus of NGC1068 does not exhibit the 3.1μm ice absorption band typical of Galactic dense molecular clouds (Wright et al., 1996; Imanishi et al., 1997). The optical depth, $\tau = 0.9$, of the 3.4μm band, is slightly smaller than that measured by CGS4+IRPOL, and the contrast between the 3.42μm peak and 3.48μm shoulder is less marked than in the old spectrum. The remote possibility exists that the profile of the 3.4μm feature changes over short timescales, but this is much more likely simply to indicate that the atmosphere has divided out more successfully in these observations. The feature's profile now looks much more like that observed in other lines of sight — lines sampling the Galactic diffuse ISM, for instance. This new L-band spectrum, and what it reveals about the carbon-containing dust in NGC1068, is discussed in Chapter 4.

2.6.3 The N-band flux spectrum of NGC1068

The 10μm flux spectrum of NGC1068 was obtained in much the same way as the CGS4 3μm spectrum, by taking a set of spectra obtained on 20011019 and ratioing them by the standard star, Rigel. The NGC1068 data taken closest in time to the standard star were of very low quality (and were rejected in the calculation of NGC1068's polarisation), leaving only data taken earlier in the night to work with. This is probably the reason why the telluric O_3 feature has not divided out very well (Fig. 2.18).

Again, the spectrum was flux-calibrated with reference to the standard star, Rigel. Rather than extrapolating from the V-band magnitude the 10μm magnitude of this star was taken from the literature and used directly (Barlow and Cohen, 1977). The measured 10μm flux of NGC1068, approximately $5 \times 10^{-12}\mathrm{Wm}^{-2}\mu\mathrm{m}^{-1}$, is in fair agreement with literature values (e.g. Rieke, 1978; Rieke and Lebofsky, 1978; Malkan and Filippenko, 1983; Roche et al.,

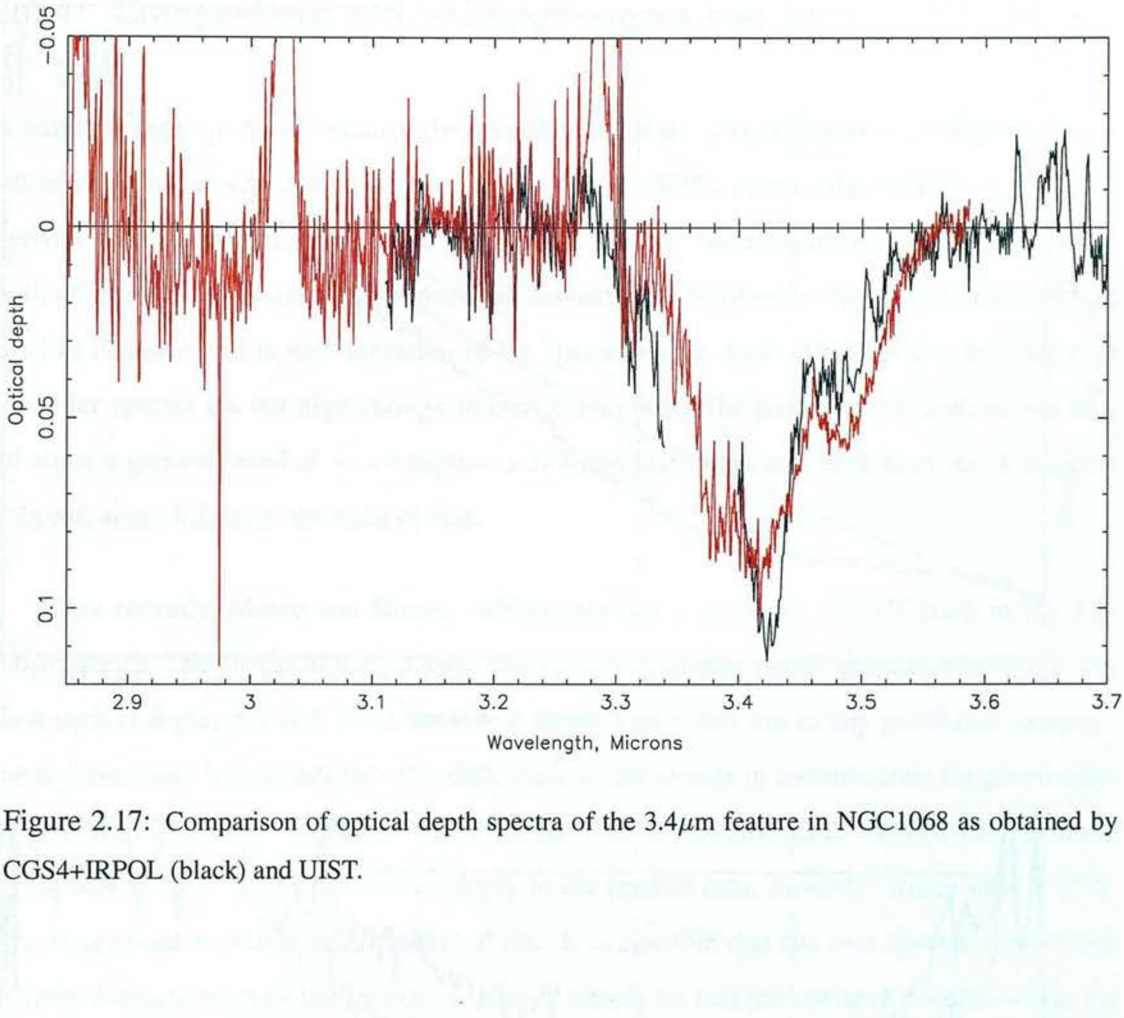

Figure 2.17: Comparison of optical depth spectra of the 3.4μm feature in NGC1068 as obtained by CGS4+IRPOL (black) and UIST.

1984), considering the differences in aperture sizes and the poor weather conditions under which these observations were made.

As the N-band atmospheric window is not a great deal wider than the silicate feature, there is some uncertainty in the shape of the continuum emission around the feature. Others have found that the shape of the spectrum in this region is "relatively flat" (Kleinmann et al., 1976), but the flux spectrum in Fig. 2.18 has a definite rise to longer wavelengths and appears to be well fit by a second-order polynomial curve. A straight-line continuum fit is also shown, to illustrate the difference that this would make to the derived optical depth. The resulting optical depth spectra of the silicate feature are also presented in Fig. 2.18. The uncertainty in the continuum and the distortion caused by the atmospheric O_3 band, mean that it is difficult to determine precisely the optical depth of the feature, but it is at least 0.3 and probably closer to 0.35 using the second-degree continuum and 0.45-0.5 using the linear fit.

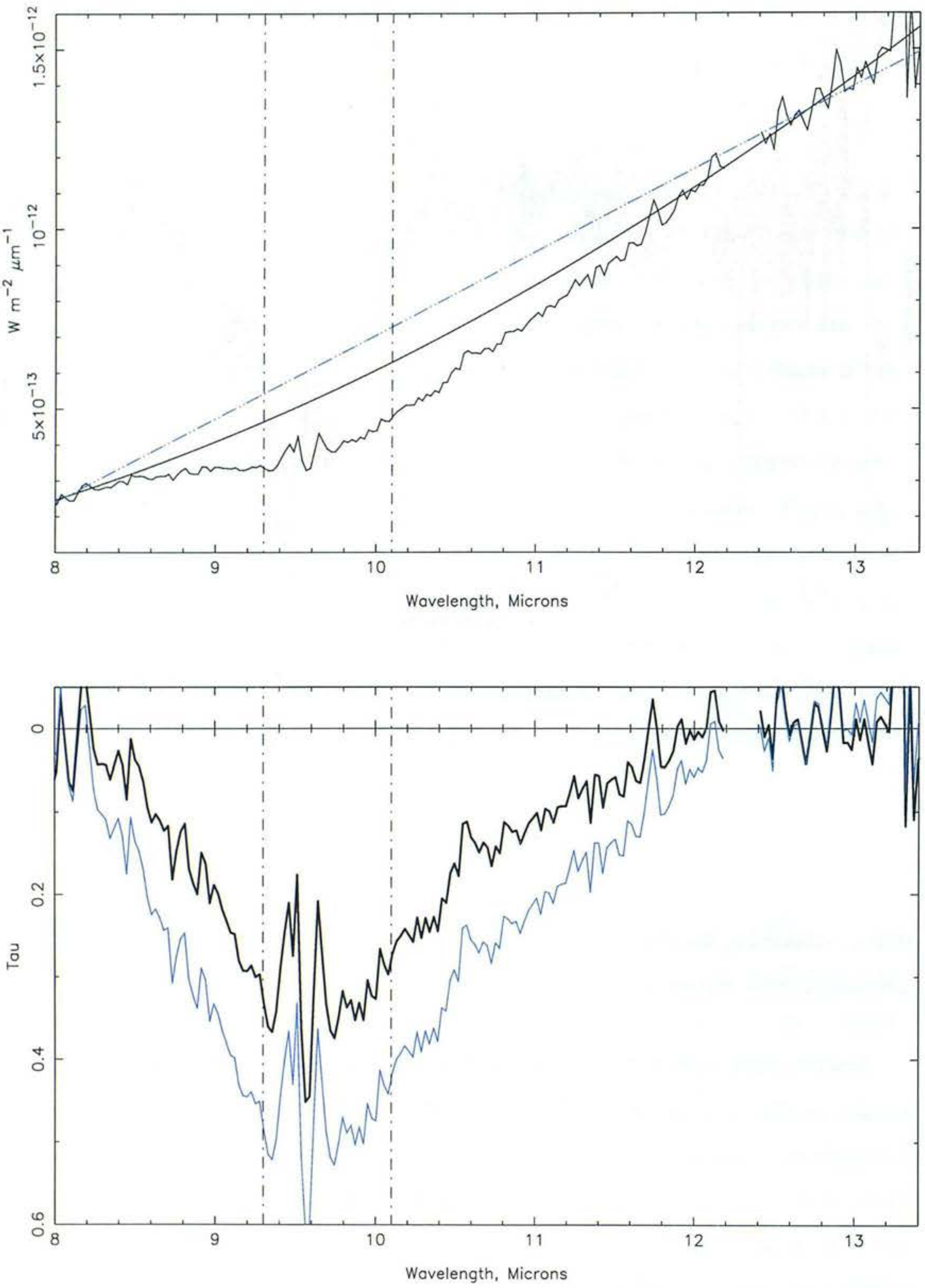

Figure 2.18: Top: ratioed N-band flux spectrum of NGC1068. The black line is a second-degree polynomial fit to the spectrum, the dashed blue line a straight-line fit. Bottom: optical depth spectra of NGC1068. The colours correspond to the continuum fits shown in the upper panel. Dashed lines show the approximate extent of the telluric ozone feature. As in §2.5.3 the small part of the spectrum corresponding to bad columns on Michelle's array has been removed.

2.6.4 Comparisons with existing observations

A number of groups have measured the optical depth of the 3.4μm feature in NGC1068. Imanishi et al. (1997) cite an optical depth of $\tau_{3.41} = 0.126 \pm 0.014$, comparable with the $\tau_{3.42} = 0.1$ derived by Bridger et al. (1994) and Wright et al. (1996). We measure $\tau_{3.4} = 0.09$, similar to both of these values. Small differences can probably be ascribed to variation in the continua used to obtain τ and in the resolution of the spectrometers used. The S/N and resolution of the older spectra are not high enough to compare in depth the profile of the feature, but they all show a general trend of an absorption maximum just longwards of 3.4μm and a possible subpeak about 0.1μm to the right of that.

More recently, Marco and Brooks (2003) obtained a spectrum of NGC1068 in the 3.0-3.6μm range. The profile of their 3.4μm feature is very similar to that presented in §2.6.2, but their optical depth, $\tau_{3.4} = 0.14$, is somewhat larger than either our or any published measurement. Marco and Brooks attribute this difference to differences in aperture size; the previously-published spectra used larger apertures and could therefore include some less-obscured material in the beam. This explanation cannot apply to the present data, however, which used a $0''.6$ slit, as opposed to Marco and Brooks' $1''$slit. It is possible that the two spectra come from slightly different parts of the galaxy, or it could simply be that the continua used to obtain the optical depth spectra were different.

The optical depth of the silicate feature in NGC1068 has been reported by Roche et al. (1984) and Tomono et al. (2001) to be 0.51 ($4''.2$ aperture) and 0.72±0.33 ($0''.4$) respectively. These measurements are similar to the value I obtain using a straight-line fit to the spectrum but somewhat larger than that obtained with a second-order polynomial continuum. The Tomono et al. (2001) optical depth was derived by fitting the observed SED of NGC1068 with greybody radiation absorbed by silicate grains; the limited number of data points used in the fit could perhaps mean that this is a less reliable estimate of $\tau_{9.7}$ than one derived from a spectrum of the feature itself.

CHAPTER 3

Modelling Extinction and Polarisation

The original motivation for measuring the polarisation of NGC1068 was to see whether the core-mantle dust model would stand up to such scrutiny. As discussed in Chapter 2, the non-detection of a rise in polarisation over the 3.4μm feature in GCIRS 7, together with an enhancement in the silicate polarisation in a nearby source, seemed to indicate that the dust in that line of sight is not in the form of core-mantle grains. However, the signal-to-noise ratio of our observations of the silicate feature in NGC1068 was low enough that we were unable to establish a helpful upper limit on its polarisation. We have, then, no simple way of relating the optical depth of the absorption features to the degree of polarisation over them, as was the case with GCIRS 7. The value of the ratio $\Delta p/\tau$ derived for GCIRS 7 depends on the degree to which the grains are aligned, and there is no reason why this should be the same in NGC1068.

To clarify the situation, I have modelled the polarisation which would be expected from various models and distributions of dust grains in order to predict the polarisation observed in the 3.4μm feature and in the IR continuum of NGC1068. As well as allowing me to calculate the 3.4μm polarisation, comparison of these results with both the present and literature observations has enabled me to investigate the nature of the grains in NGC1068, in particular the size distribution and structure of the aligned grain population. Having established a method, I have also applied the modelling technique to the A99 observations of GCIRS 7.

In this chapter I discuss the parameters and assumptions used in the modelling, together with the some of the theory which makes it possible. Chapter 4 deals with the interpretation of the results, and the conclusions this work allows us to draw about the grains in NGC1068 and GCIRS 7.

3.1 The near-IR polarisation of NGC1068

Prior to that, however, there is an important issue which must be addressed: Fig 2.7 clearly shows that we have detected NIR polarisation towards the nucleus of NGC1068, but is it clear that dust absorption is the cause of it? In discussing polarisation caused by dust I have assumed that dichroic absorption is the dominant mechanism, and this is thought to be the case in the Galactic diffuse ISM. There, the grains are cold enough that polarised near-IR emission from aligned grains will be insignificant. A blackbody source whose emission peaks at 3μm has a temperature of $\sim$ 1000K, much hotter than the $\sim$ 20K dust temperature typical of the diffuse ISM. The grains are also small enough that absorption will be a far more important process than scattering. When light is scattered from small spherical grains, the angular distribution of the scattered light is different for the two components of the incoming electric field vector (Fig. 3.1, left panel). For forward scattering the cross-sections C_{sca} for the two components are equal, so forward-scattered light is unpolarised. At 90°, however, $C_{sca} = 0$ for one component so the scattered light in that direction is completely polarised. Depending on the geometry of the source and scattering material relative to the line of sight, scattered light can be highly polarised. For grains the $\lesssim 0.1\mu$m size of most of those in the diffuse ISM, though, the absorption cross-section $C_{abs} \gg C_{sca}$ and the observed IR polarisation is due to dichroism (Fig. 3.1, right panel).

Dichroic absorption may be the dominant source of infrared polarisation in the Galactic diffuse ISM, but it is not clear *a priori* whether this will also be the case in NGC1068. As discussed in §1.3, the circumnuclear dust is warm, and its dense environment might encourage coagulation of small grains into larger ones. The polarisation mechanisms in NGC1068 have,

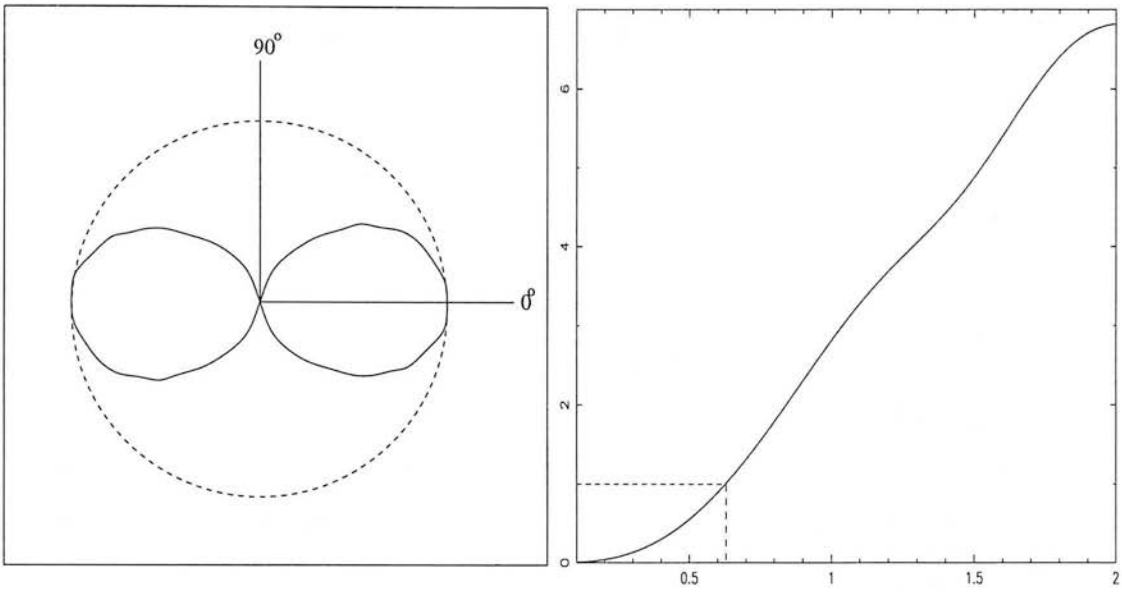

Figure 3.1: Left panel: polar plot of angular scattering for spheres small compared with the wavelength. The normalised scattered intensities, $i_{\|}/C_{sca}$ and $i_{\perp}/C_{sca}$ are shown by solid and dashed lines, respectively. Right panel: Q_{sca}/Q_{abs} for silicate spheres vs the size parameter, $x = 2\pi a/\lambda$. The dashed line shows $Q_{sca}/Q_{abs} = 1$, at $x \approx 0.63$, equivalent to a sphere of radius 0.3μm at 3.0μm (for example). The efficiencies, Q_{abs} and Q_{sca}, are related to cross-sections by $Q = C/\pi a^2$.

however, been the subject of intense study, and Fig. 3.2 shows some of the relevant measurements which have been made. Antonucci and Miller (1985) were among the first to observe the UV and visible polarisation of NGC1068, famously discovering a hidden broad line region in this Seyfert II galaxy. They interpreted the high, wavelength-independent polarisation as being due to scattering off very small particles, probably free electrons. This scattering region is shown schematically as [4] in Fig. 1.3. Bailey et al. (1988) later discussed the polarisation properties of NGC1068 from the UV out to 10μm, and found a twist in position angle from the optical into the near-IR. They interpreted this as dust or electron scattering being replaced by dust absorption as the most important polarising mechanism. Their data also show an abrupt change of $\sim 70°$ in position angle at 4.8μm, which is what would be expected if emission from aligned dust grains takes over from absorption at about this wavelength.

Further evidence for the importance of dichroic absorption as an IR polarisation mechanism comes from the imaging polarimetry of Lumsden et al. (1999). After analysing the deviations from the centrosymmetric polarisation patterns expected from scattering alone, they conclude that their data are consistent with another mechanism of constant position angle contributing

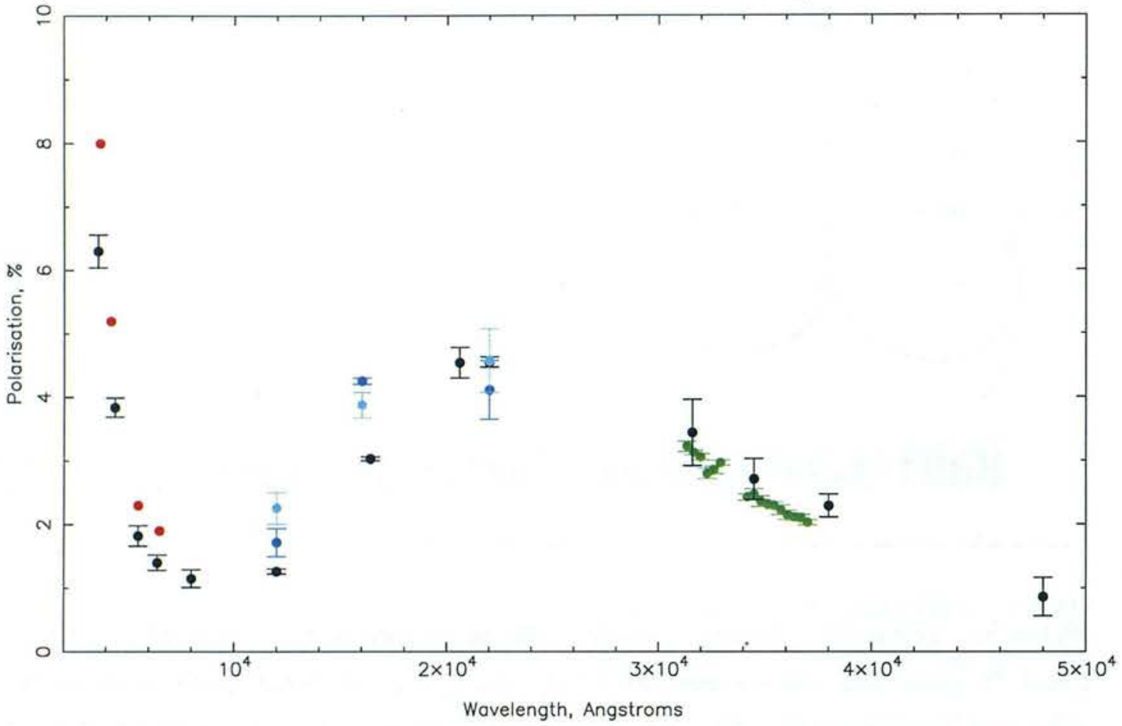

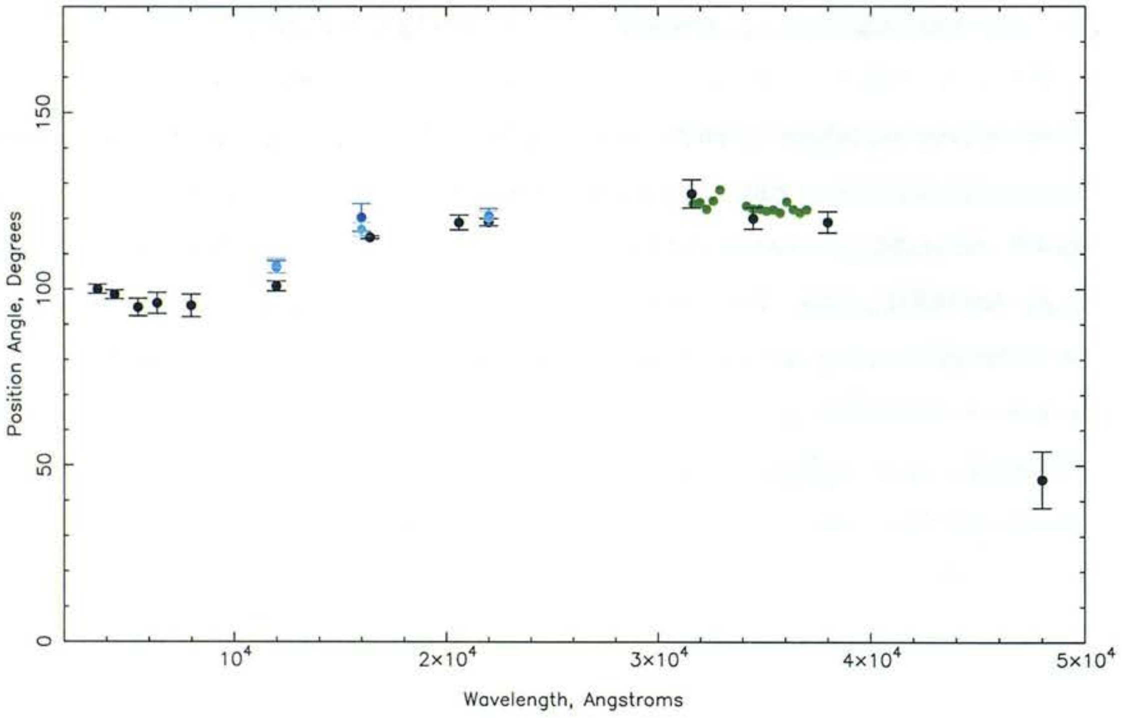

Figure 3.2: The percentage polarisation and position angle of polarisation of NGC1068, from the UV to the IR. Green — the present work; black — Bailey et al. (1988); red — Antonucci and Miller (1985, before correction for dilution by starlight (position angle and errors not available)); blue — Packham et al. (1997); light blue — Lumsden et al. (1999).

to the polarisation. The effect of this other mechanism grows with increasing wavelength, out to the K band, as would be expected if absorption were taking over from scattering. The position angle of the polarisation caused by this effect is $\sim 115°$, close to the inclination angle of the torus-like structure in NGC1068 ($\sim 100°$, Marco and Alloin, 2000). Lumsden et al. (1999) estimated that this mechanism contributes $> 90\%$ of the K-band polarisation. Whereas Lumsden et al. (1999) found that the characteristic centrosymmetric scattering patterns were only observed at distances >2" from the scattering centre, though, analysis of more recent HST data shows that the deviations are in fact confined to a smaller region, within 1" from the peak of the polarised flux (Simpson et al., 2002). The optimal extraction algorithm used to extract spectra from our spectropolarimetric data (§2.4.2) typically used data from about 5 rows on the array, with about $\frac{2}{3}$ of the extracted flux coming from the central three rows. CGS4's pixels span 0".61 in the spatial direction, meaning that a substantial fraction of the light we observe comes from within a 1" radius of the nucleus. Furthermore, the evidence I discuss below implies that in the L band the polarisation we observe is predominantly caused by dust absorption.

Lumsden et al. (1999) were successful in fitting their observed JHK polarised flux points with greybody emission from hot (T$\sim$1200K) dust, reddened by a $\lambda^{-1.75}$ extinction curve and scaled by a Serkowski law appropriate for moderately extinguished Galactic sources. This is consistent with the more detailed modelling of Young et al. (1995), who find that neither electron nor dust scattering can account for the near-IR polarisation unless the underlying Seyfert I nucleus presumed to power NGC1068 has a more extreme spectrum than any yet observed. However, if a dichroic component is added, the near-IR polarised flux spectrum can be reproduced. In the Young et al. (1995) model there is still some contribution from electron scattering to the near-IR flux, but this decreases with wavelength relative to the dichroic component. By the K-band, electron scattering contributes perhaps 10% of the total flux, with dust making up almost all of the remainder. Together, imaging polarimetry, spectral modelling and the observation of a near-90°flip in position angle suggest that we can expect a model of the *L-band* polarisation of NGC1068 based on absorptive dichroism to be a reasonable representation of the true situation.

At shorter wavelengths, the contribution from scattering is larger. This is not a problem for models of the 3-4μm polarisation, but if we wish to model the J-, H- and K-band polarisation, this needs to be taken into account. In the Young et al. (1995) model, the polarisation below approximately 1.3μm can be completely accounted for by scattering. This suggests that we should not attempt to model the J-band polarisation of NGC1068 using solely dust absorption as a polarising mechanism. In the H-band, at 1.6μm, their model requires that scattering and dust emission both contribute to the observed flux. By the K-band, though, Young et al. (1995) find that the dichroic component is roughly ten times greater than the scattered component. This means that the polarisation at this wavelength will be dominated by dichroism, a finding consistent with the evidence discussed above. K-band polarisation data, then, can be considered a reasonable estimate of the polarisation caused by dust absorption alone. The implications of the origins of the JHK polarisation for the interpretation of this modelling are discussed further in Chapter 4.

Before attempting to interpret infrared polarisation data of a galaxy, though, there is another effect which must be investigated. With the spatial resolution that is currently available, the region of an AGN that is observed will contain flux not only from the nuclear source and surrounding dust, but also from stars. Light from stars, unless it has been absorbed or scattered by dust in the line of sight, is unpolarised, so adding in this component will have the effect of "diluting" the polarisation. If an estimate can be made for the fraction of the observed flux that comes from the polarised, nonstellar component, then a correction can be made:

$$P_{corr} = P_{obs} \times \left(\frac{100}{f_{nonstellar}} \right) \tag{3.1}$$

The dilution from the unpolarised stellar component will be wavelength-dependent (depending in turn on the temperature of the stars), so this correction will need to be assessed and applied at each wavelength at which the polarisation is measured.

Estimates of the contribution of the stellar component to the observed flux from the nucleus of NGC1068 have been made by various groups (McCarthy et al., 1982; Origlia et al., 1993; Thatte et al., 1997; Alonso-Herrero et al., 2001b). The method of Alonso-Herrero et al. (2001b) involved a decomposition of observed surface brightness profiles into nuclear and stellar components. In the case of their ground-based data, the nucleus was described by a delta function convolved with a Gaussian profile to account for seeing effects. To fit their space-based data, a point-spread function was used to represent the nucleus. In both cases the stellar bulge was described by an $r^{\frac{1}{4}}$ profile. Thatte et al. (1997) and Origlia et al. (1993) took a different approach.

Ref.	Aperture Diameter	J(%)	H(%)	K(%)	L(%)
1a	3"	17	47	69	95
1b	3"	9	41	71	—
2	3"	—	59	81	—
3	4.4"	—	~ 30	$\gtrsim 80$	—
4	5".2x10".5	—	—	~ 80	—

Table 3.1: Percentage of the light from NGC1068 which comes from a nonstellar source. References: 1a) Alonso-Herrero et al. (2001b), ground-based data; 1b) Alonso-Herrero et al. (2001b), space-based data; 2) Thatte et al. (1997); 3) Origlia et al. (1993); 4) McCarthy et al. (1982). Data from Thatte et al. (1997) were originally given for concentric annular apertures; figures shown here are weighted averages over 3" diameter circular apertures.

They took advantage of the observation that the ratio of the stellar Si and CO lines at 1.59 and 1.62μm can be used to predict the intrinsic equivalent width of the stellar CO lines. The contribution of a non-stellar component to the total near-IR flux can then be computed from the ratio of the observed and intrinsic equivalent widths of those lines. The values obtained are listed in Table 3.1; clearly the correction will be most important in the J band, where as much as $\sim 90\%$ of the flux may come from stars. Even at K, though, a significant correction will be necessary. It is only at longer wavelengths, in the L and M bands, that little or no correction is required.

As it is not immediately apparent which of the above methods will give the more accurate estimate of the stellar contribution — stellar lines or nucleus+bulge decomposition — I have explored the effect on the polarisation of NGC1068 of correcting for the values given by both Alonso-Herrero et al. (2001b) (both sets of data) and Thatte et al. (1997). The figures are quoted for apertures of 3" diameter, but the available polarisation data are for apertures of 2" (Packham et al., 1997; Lumsden et al., 1999) and 4".5 (Bailey et al., 1988). Clearly the relative amounts of stellar and nonstellar emission in the beam will be aperture-dependent, so I have averaged the polarisations given by Bailey et al. (1988), Packham et al. (1997) and Lumsden et al. (1999) in order to more closely approximate the polarisation which would be measured in a 3" aperture. The L-band is something of a special case. Although Alonso-Herrero et al. (2001b) cite a figure of 95% for the nonstellar component at L, this is for a larger aperture than that used for the spectropolarimetry presented in this thesis. As discussed above, most of the

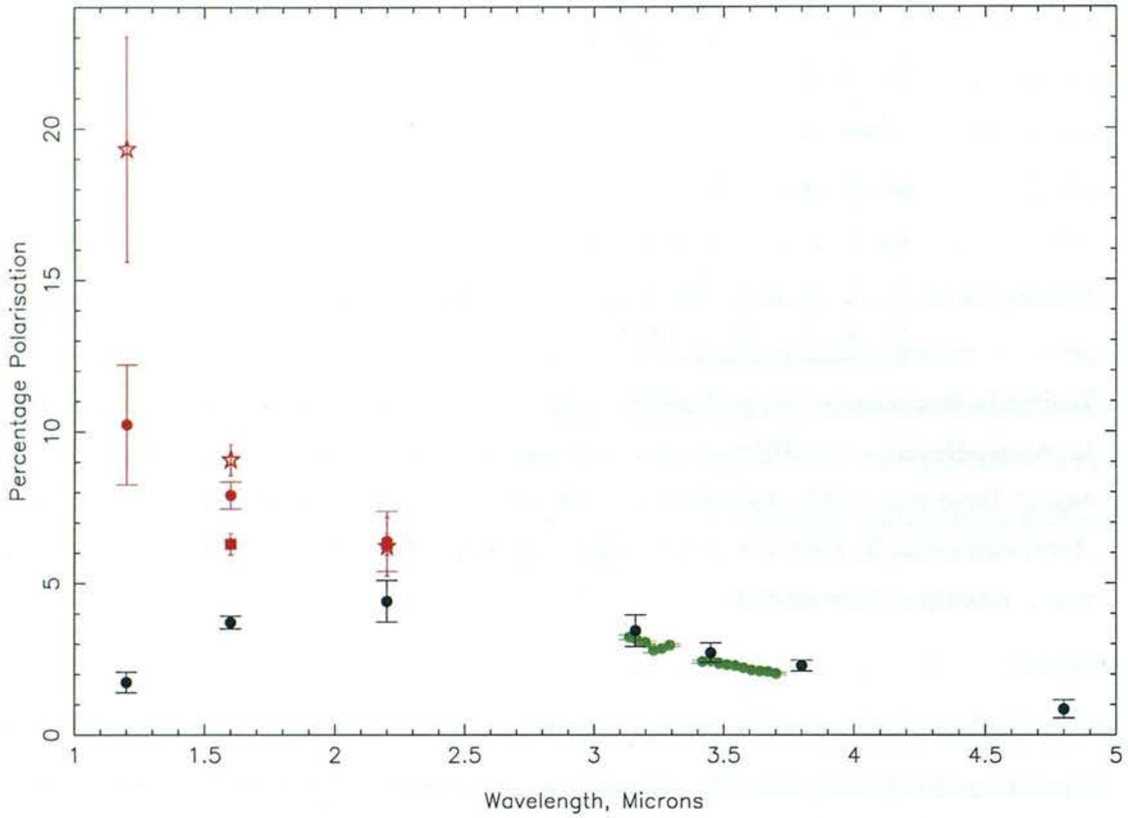

Figure 3.3: 1-5μm polarisation of NGC1068, corrected for dilution by unpolarised starlight. The black and green points show the observed polarisation: at J, H, and K, the mean of the Bailey et al. (1988), Packham et al. (1997) and Lumsden et al. (1999) data, at longer wavelengths, the Bailey et al. (1988) and the present data. The red points represent the polarisation after correction for the contribution of unpolarised starlight (as no errors were quoted for the nonstellar fractions of Alonso-Herrero et al. (2001b) the error bars reflect the errors of the observed polarisation only). Stars — using the Alonso-Herrero et al. (2001b) NICMOS data; circles — using the Alonso-Herrero et al. (2001b) UKIRT data; squares — using the Thatte et al. (1997) data.

flux we observe from NGC1068 comes from an area of (extraction window × slit width) = 1.1 sq. arcsec. Thatte et al. (1997) find that even in the K-band, 94±5% of the light in a 0.78 sq. arcsec aperture is nonstellar. This suggests that, at the longer wavelengths of the L-band, the stellar dilution of the polarisation will be negligible. I do, however, note that as the stellar contribution decreases with wavelength, the effect of any correction would be to increase the slope of the continuum polarisation.

The polarisation which results from the correction for unpolarised starlight, using equation 3.1, is shown in Fig. 3.3. The difference between this and the uncorrected polarisation in Fig. 3.2 is clear: the polarisation now rises strongly to shorter wavelengths. As will be discussed in §3.5.2 and §4.1, the size of the polarising dust grains is a crucial factor governing the behaviour of the polarisation over the 3.4μm feature, and the wavelength dependence of the polarisation may provide us with a means of constraining that size. It is therefore very important to know the true polarisation of the nucleus of this galaxy.

The model described in this chapter and the next implicitly treats the dust as a simple absorbing screen in front of a source of unpolarised radiation. Clearly, this actual situation in NGC1068 will be rather more complex. If, as suggested by Lumsden et al. (1999) and many others, the source of the observed infrared radiation from NGC1068 is hot dust itself heated by a central source, there will be a temperature gradient through the dust. The hotter dust grains closer to the nucleus will suffer more extinction than the cooler grains, and as more of the shorter-wavelength radiation is emitted by the hotter grains, the near-IR radiation will be more extinguished than the mid-IR emission. This may well mean that, even in the case of pure dichroic polarisation, the wavelength dependence of the polarisation will reflect not only the size and composition of the dust, but also the amount of absorption experienced at different wavelengths. However, the small range of wavelengths covered by our spectropolarimetry of 3.4μm feature should mean that the polarisation over and around this feature is relatively unaffected by the complexity of the source (see §4.1).

As the observed degree of polarisation (as opposed to polarised flux) is independent of the spectrum of the source, no assumptions need to be made about the intrinsic flux of NGC1068. As far as extinction is concerned, I do not try to reproduce the observed flux spectrum but instead deal only with the optical depth of the 3.4μm feature. As long as reliable continua can be fitted to the data at each side of the feature, this should allow a fair comparison between the shape and depth of the observed and calculated bands. In this situation, the polarisation spectrum and 3.4μm band shape and depth can be derived from the extinction cross-sections and efficiencies of the grains concerned. The rest of this chapter is devoted to describing the way in which the cross-sections can be calculated, the information needed to achieve this, and how they can then be turned into observable quantities.

3.2 Calculating extinction and polarisation

When an electromagnetic field is incident upon a particle, it induces dipole moments in the material. The dipoles oscillate at the frequency of the field, scattering radiation in all directions. The part of the incident field that does not reappear as scattered radiation is converted into other forms of energy (e.g. thermal energy); this fraction is said to have been absorbed by the particle. The balance between absorption and scattering for a given material is governed by the complex refractive index for that material, $m(\lambda) = n(\lambda) + ik(\lambda)$.

The first step in calculating extinction and polarisation is to calculate the electromagnetic field in the particle and in the medium in which it is embedded, in accordance with the refractive index of the particle and with the requirement that the field be continuous across its surface (the boundary condition). In the case of a homogeneous spherical particle, Gustav Mie and Peter Debye independently established that exact solutions could be found, and developed analytical expressions to solve the problem of scattering and absorption by a sphere. The result is now known as "Mie theory" and is extensively discussed by, for example, Bohren and Huffman (1983). I have made use of this now-standard result when using the computer codes "BHMIE" and "BHCOAT" to calculate extinction cross-sections for spherical particles as a check on the accuracy of the approximate solutions discussed in §3.2.1.

As well as spheres, exact solutions can be obtained for infinite cylinders and spheroids (Asano and Yamamoto, 1975; Bohren and Huffman, 1983), but there are disadvantages to using the exact solutions. In particular, the computations can be long, complicated and (for spheroids at least) still considered non-standard, and the range of shapes that can be examined is very restricted. Fortunately, several approximate techniques have been developed which permit relatively straightforward calculation of extinction and polarisation for a wide range of particles.

3.2.1 The Discrete Dipole Approximation

If it were somehow possible to treat separately every atom in a dust grain, extinction cross-sections could be calculated for grains of any shape or size, based on the response of each atom to the incident electric field and to the field of all the other atoms in the grain. Given the enormous number of atoms in even the smallest dust grain this approach is clearly not feasible, but the same principle forms the basis of the "Discrete Dipole Approximation" (DDA), conceived by Purcell and Pennypacker (1973) and expanded by Draine (1988). Purcell and Pennypacker realised that a dust grain can be described as an array of elements — dipole oscillators — on a cubic lattice, each oscillator representing a fairly large number of actual atoms. Then the appropriate polarisability, $\alpha = \alpha' + i\alpha''$, of each element can be derived from the bulk optical properties, ϵ, of the material using the Clausius-Mossotti relation (Jackson, 1975). The amplitude of the ith dipole is simply

$$\mathbf{P}_i = \alpha \mathbf{E}_i \tag{3.2}$$

in which $\mathbf{E}_i$ is the electric field impinging on that element, from the incident field and the field of all the other dipoles, $\mathbf{P}_j$.

Knowledge of $\mathbf{P}_i$ allows useful cross-sections to be obtained. The extinction cross-section is defined as the ratio of the total power taken from the wave to the incident power per unit area (Jackson, 1975). The time-averaged rate of work done by the electric field in powering the dipoles is

$$\frac{dW}{dt} = \left\langle \mathbf{E}.\dot{\mathbf{P}} \right\rangle \tag{3.3}$$

or, using complex representation,

$$\frac{dW}{dt} = \frac{1}{2}\mathbf{Re}\left(\mathbf{E}^*.\dot{\mathbf{P}}\right) \tag{3.4}$$

Knowing that $\mathbf{P} = \alpha \mathbf{E}_0 e^{i\omega t}$, and, therefore, that $\dot{\mathbf{P}} = \alpha \mathbf{E}_0 e^{i\omega t}.\,(i\omega)$, this brings us to

$$\frac{dW}{dt} = \frac{1}{2}\omega \mathbf{Im}\left(\mathbf{E}^*.\mathbf{P}\right) \tag{3.5}$$

The Poynting vector describes the power per unit area crossing a surface perpendicular to that vector (Hecht and Zajac, 1974)

$$\mathbf{S} = c^2 \epsilon_0 \mathbf{E} \times \mathbf{B} \tag{3.6}$$

and the incident electromagnetic flux density on that surface is given by its time-averaged magnitude

$$I = \langle S \rangle = \frac{c\epsilon_0}{2} E_0^2 \tag{3.7}$$

The extinction cross-section, therefore, is

$$C_{ext} = \frac{\text{work rate}}{\text{incident flux density}} = \frac{k}{\epsilon_0 E_0^2}\mathbf{Im}\left(\mathbf{E}^*.\mathbf{P}\right) \tag{3.8}$$

where $k = \omega/c$.

The oscillating dipoles reradiate some of the light incident upon them, and this is seen as the radiation scattered by the system. The scattering cross-section is then the ratio of the power radiated by the dipoles to the incident flux density. The power radiated by an oscillating dipole is given by Larmor's formula

$$\dot{\varepsilon} = \frac{2}{3}\frac{e^2}{4\pi\epsilon_0 c^3}\,\dot{\nu}^2 \tag{3.9}$$

which relates to the dipole amplitude $\mathbf{P}$ through $\mathbf{P} = ex$

$$\dot{\varepsilon} = \frac{1}{3}\frac{\mathbf{P}.\mathbf{P}^*}{4\pi\epsilon_0}\frac{\omega^4}{c^3} \tag{3.10}$$

where $\dot{\nu} = -\omega^2 x$. The scattering cross-section is then

$$C_{sca} = \frac{\text{power radiated}}{\text{incident flux density}} = \frac{2}{3}\frac{k^4}{\epsilon_0 E_0^2}\mathbf{P}.\mathbf{P}^* \tag{3.11}$$

Finally, the absorption cross-section can be obtained from

$$C_{abs} = C_{ext} - C_{sca} \tag{3.12}$$

The great advantage of approximate methods such as this one is that they can readily cope with shapes other than spheres and infinite cylinders which might be more appropriate descriptions of interstellar dust grains. The range of cases in which the DDA can reliably be applied has been examined (Draine and Goodman, 1993; Draine and Flatau, 1994) and a Fortran code to implement it made available to the public. It is this code, DDSCAT5a.10 (Draine and Flatau, 2000), that I have used for all the calculations on non-spherical grains presented in this work.

3.2.2 Applicability and use of DDSCAT5a.10

The reliability of DDSCAT's calculations is governed by the refractive index, $m = m' + im''$, of the material, the number of dipoles and interdipole spacing in the target and the wavelength in question. Tests of DDSCAT show that reliable cross-sections can be obtained if $N > 10^4$ dipoles are used, $|m|kd < 1$ and $|m - 1| < 2$, where $k = 2\pi/\lambda$ and d is the interdipole spacing (Draine and Flatau, 2000). The first criterion can be used to find the maximum grain radius for which accurate results may be calculated:

$$a(\mu\mathrm{m}) < 9.88\frac{\lambda(\mu\mathrm{m})}{|m|}\left(\frac{N}{10^6}\right)^{1/3} \tag{3.13}$$

The shortest wavelength I consider in the models is 1μm, and values of $|m|$ for the grain materials are never more than about 1.8 at that wavelength. As a result the calculations should be reliable to a grain size of $a = 1.22\mu$m, if 10^4 dipoles are used. The largest particle considered in the models has $a = 1.0\mu$m.

The highest value of the complex refractive index of the grain materials I consider, $m' = 2.0, m'' = 0.9$ occurs within the silicate bond stretch. Using these values, the maximum value of $|m-1| = \sqrt(1^2+0.9^2) = 1.3$. It can therefore be expected that calculations using DDSCAT will give accurate results for the range of parameters explored in the models.

Input parameters

The input required by DDSCAT is illustrated in the sample input file, "ddscat.par", shown in Fig. 3.4. Lines 3-8 set options such as the algorithms to be used in DDSCAT's calculations; I have stayed with the suggested defaults for these. The first line which may require alteration is that specifying the shape of the target particle. I have used the options CONELL and ELLIPS, which provide for coated and uncoated ellipsoids. The precise shape of the ellipsoid (and, indirectly, the number of dipoles within it) is governed by the values of the "shape parameters" on line 10. For an uncoated oblate spheroid with axial ratios 2:2:1, for example, $SHPAR1 = SHPAR2 = 2 \times SHPAR3$.

Of course, DDSCAT also needs to be provided with the refractive indices of the grain material(s), and files containing these are named in ddscat.par. ICTHM and IPHM in lines 17-18 determine the number of angles at which the scattered intensity is calculated, which will in turn affect the scattering cross-section C_{sca}. Draine and Flatau (2000) suggest that ICTHM $> 5(1+x)$ and IPHM $> 2(1+x)$ should be used (where $x = 2\pi a/\lambda$), while cautioning that this is only a very rough rule-of-thumb.

After setting the wavelength to be used, the grain size must be fixed. As particles of arbitrary shape can be dealt with by DDSCAT, this is given in terms of the "effective radius", the

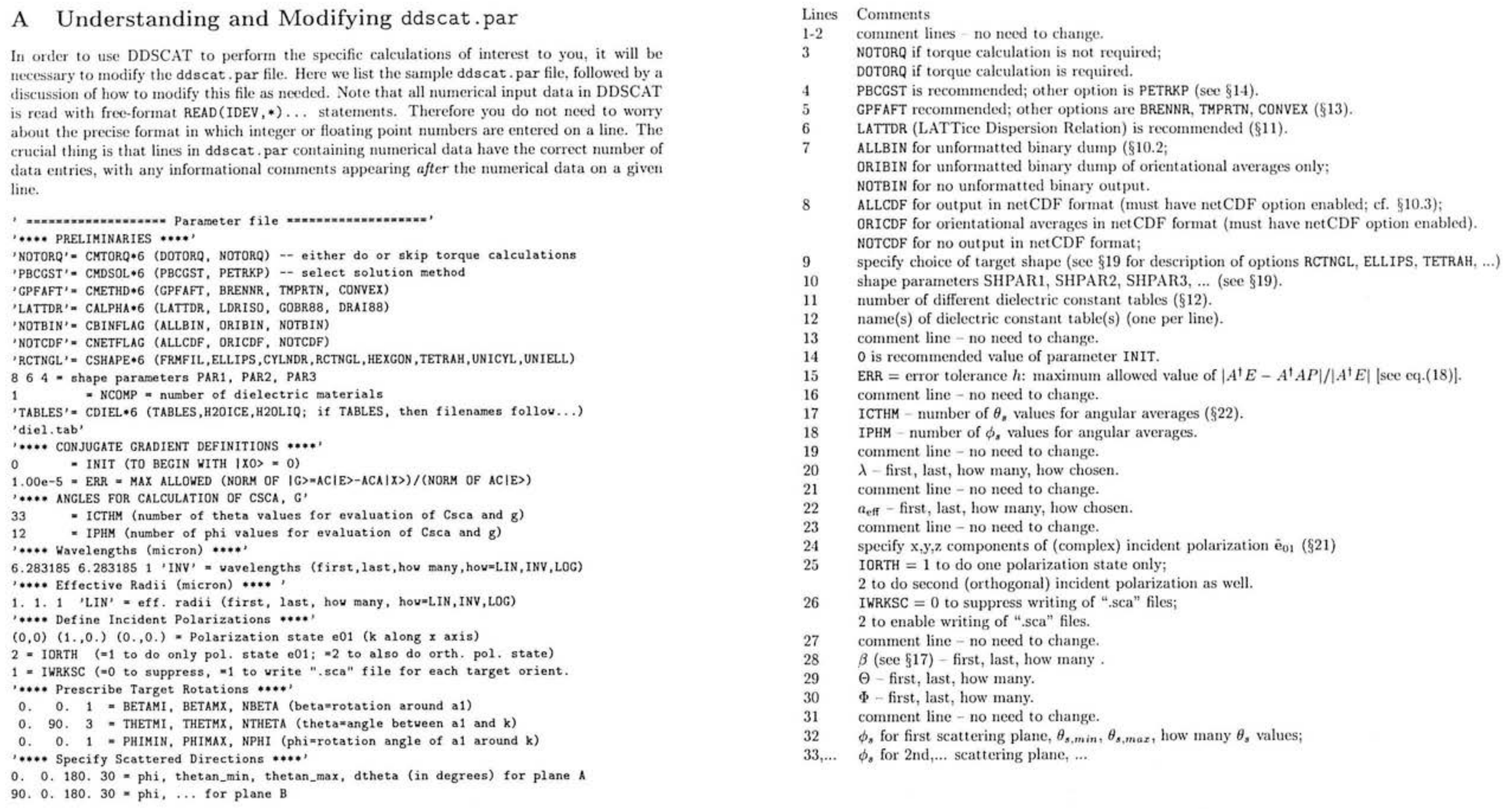

A Understanding and Modifying `ddscat.par`

In order to use DDSCAT to perform the specific calculations of interest to you, it will be necessary to modify the `ddscat.par` file. Here we list the sample `ddscat.par` file, followed by a discussion of how to modify this file as needed. Note that all numerical input data in DDSCAT is read with free-format `READ(IDEV,*)...` statements. Therefore you do not need to worry about the precise format in which integer or floating point numbers are entered on a line. The crucial thing is that lines in `ddscat.par` containing numerical data have the correct number of data entries, with any informational comments appearing *after* the numerical data on a given line.

```
' ==================== Parameter file ===================='
'**** PRELIMINARIES ****'
'NOTORQ'= CMTORQ*6 (DOTORQ, NOTORQ) -- either do or skip torque calculations
'PBCGST'= CMDSOL*6 (PBCGST, PETRKP) -- select solution method
'GPFAFT'= CMETHD*6 (GPFAFT, BRENNR, TMPRTN, CONVEX)
'LATTDR'= CALPHA*6 (LATTDR, LDRISO, GOBR88, DRAI88)
'NOTBIN'= CBINFLAG (ALLBIN, ORIBIN, NOTBIN)
'NOTCDF'= CNETFLAG (ALLCDF, ORICDF, NOTCDF)
'RCTNGL'= CSHAPE*6 (FRMFIL,ELLIPS,CYLNDR,RCTNGL,HEXGON,TETRAH,UNICYL,UNIELL)
8 6 4 = shape parameters PAR1, PAR2, PAR3
1        = NCOMP = number of dielectric materials
'TABLES'= CDIEL*6 (TABLES,H2OICE,H2OLIQ; if TABLES, then filenames follow...)
'diel.tab'
'**** CONJUGATE GRADIENT DEFINITIONS ****'
0       = INIT (TO BEGIN WITH |XO> = 0)
1.00e-5 = ERR = MAX ALLOWED (NORM OF |G>=AC|E>-ACA|X>)/(NORM OF AC|E>)
'**** ANGLES FOR CALCULATION OF CSCA, G'
33      = ICTHM (number of theta values for evaluation of Csca and g)
12      = IPHM (number of phi values for evaluation of Csca and g)
'**** Wavelengths (micron) ****'
6.283185 6.283185 1 'INV' = wavelengths (first,last,how many,how=LIN,INV,LOG)
'**** Effective Radii (micron) **** '
1. 1. 1  'LIN' = eff. radii (first, last, how many, how=LIN,INV,LOG)
'**** Define Incident Polarizations ****'
(0,0) (1.,0.) (0.,0.) = Polarization state e01 (k along x axis)
2 = IORTH  (=1 to do only pol. state e01; =2 to also do orth. pol. state)
1 = IWRKSC (=0 to suppress, =1 to write ".sca" file for each target orient.
'**** Prescribe Target Rotations ****'
 0.   0.  1  = BETAMI, BETAMX, NBETA (beta=rotation around a1)
 0.  90.  3  = THETMI, THETMX, NTHETA (theta=angle between a1 and k)
 0.   0.  1  = PHIMIN, PHIMAX, NPHI (phi=rotation angle of a1 around k)
'**** Specify Scattered Directions ****'
0.  0. 180. 30 = phi, thetan_min, thetan_max, dtheta (in degrees) for plane A
90. 0. 180. 30 = phi, ... for plane B
```

Lines	Comments
1-2	comment lines – no need to change.
3	`NOTORQ` if torque calculation is not required; `DOTORQ` if torque calculation is required.
4	`PBCGST` is recommended; other option is `PETRKP` (see §14).
5	`GPFAFT` recommended; other options are `BRENNR`, `TMPRTN`, `CONVEX` (§13).
6	`LATTDR` (LATTice Dispersion Relation) is recommended (§11).
7	`ALLBIN` for unformatted binary dump (§10.2; `ORIBIN` for unformatted binary dump of orientational averages only; `NOTBIN` for no unformatted binary output.
8	`ALLCDF` for output in netCDF format (must have netCDF option enabled; cf. §10.3); `ORICDF` for orientational averages in netCDF format (must have netCDF option enabled). `NOTCDF` for no output in netCDF format;
9	specify choice of target shape (see §19 for description of options `RCTNGL`, `ELLIPS`, `TETRAH`, ...)
10	shape parameters SHPAR1, SHPAR2, SHPAR3, ... (see §19).
11	number of different dielectric constant tables (§12).
12	name(s) of dielectric constant table(s) (one per line).
13	comment line – no need to change.
14	`0` is recommended value of parameter `INIT`.
15	`ERR` = error tolerance h: maximum allowed value of $\lvert A^\dagger E - A^\dagger AP\rvert/\lvert A^\dagger E\rvert$ [see eq.(18)].
16	comment line – no need to change.
17	`ICTHM` – number of θ_s values for angular averages (§22).
18	`IPHM` – number of ϕ_s values for angular averages.
19	comment line – no need to change.
20	λ – first, last, how many, how chosen.
21	comment line – no need to change.
22	$a_{\rm eff}$ – first, last, how many, how chosen.
23	comment line – no need to change.
24	specify x,y,z components of (complex) incident polarization $\hat{\mathbf{e}}_{01}$ (§21)
25	`IORTH` = 1 to do one polarization state only; 2 to do second (orthogonal) incident polarization as well.
26	`IWRKSC` = 0 to suppress writing of ".sca" files; 2 to enable writing of ".sca" files.
27	comment line – no need to change.
28	β (see §17) – first, last, how many .
29	Θ – first, last, how many.
30	Φ – first, last, how many.
31	comment line – no need to change.
32	ϕ_s for first scattering plane, $\theta_{s,min}$, $\theta_{s,max}$, how many θ_s values;
33,...	ϕ_s for 2nd,... scattering plane, ...

Figure 3.4: A sample DDSCAT input file, taken from the DDSCAT User Guide (Draine and Flatau, 2000).

radius of a sphere with volume equal to the volume of the target particle. The lengths of the axes of an ellipsoidal grain are related to the effective radius through the shape parameters:

$$\begin{aligned}
r_1 &= \left[\frac{a^3}{(SHPAR2/SHPAR1)\,(SHPAR3/SHPAR1)}\right]^{1/3} && (3.14)\\
r_2 &= r_1\left(\frac{SHPAR2}{SHPAR1}\right) && (3.15)\\
r_3 &= r_1\left(\frac{SHPAR3}{SHPAR1}\right) && (3.16)
\end{aligned}$$

where r_1, r_2 and r_3 are the lengths of the axes defined by SHPAR1, SHPAR2 and SHPAR3 respectively.

The number of dipoles in the target must be large; $> 10^4$ to satisfy the above applicability criteria, and certainly large enough that the interdipole spacing is small compared to the wavelength and any structure in the target. The interdipole spacing relates to the target's axis lengths and the shape parameters through

$$(r_1/SHPAR1)^2 + (r_2/SHPAR2)^2 + (r_3/SHPAR3)^2 = d^2/4 \qquad (3.17)$$

and the number of dipoles in the target is approximately

$$N \approx \frac{4}{3}\pi SHPAR1 \times SHPAR2 \times SHPAR3. \qquad (3.18)$$

In fixing many of these parameters it is assumed that the target has a specific orientation with respect to the incident light, and this is dealt with in lines 28-30. Fig. 3.5 shows the reference frame in which DDSCAT operates. The target orientation is set by choosing appropriate values of the angles β, Θ and Φ. Finally, if scattering in particular directions is of interest, these directions can be specified in the last two lines. The workings of DDSCAT are described in more detail, with examples, in the DDSCAT User Guide (Draine and Flatau, 2000).

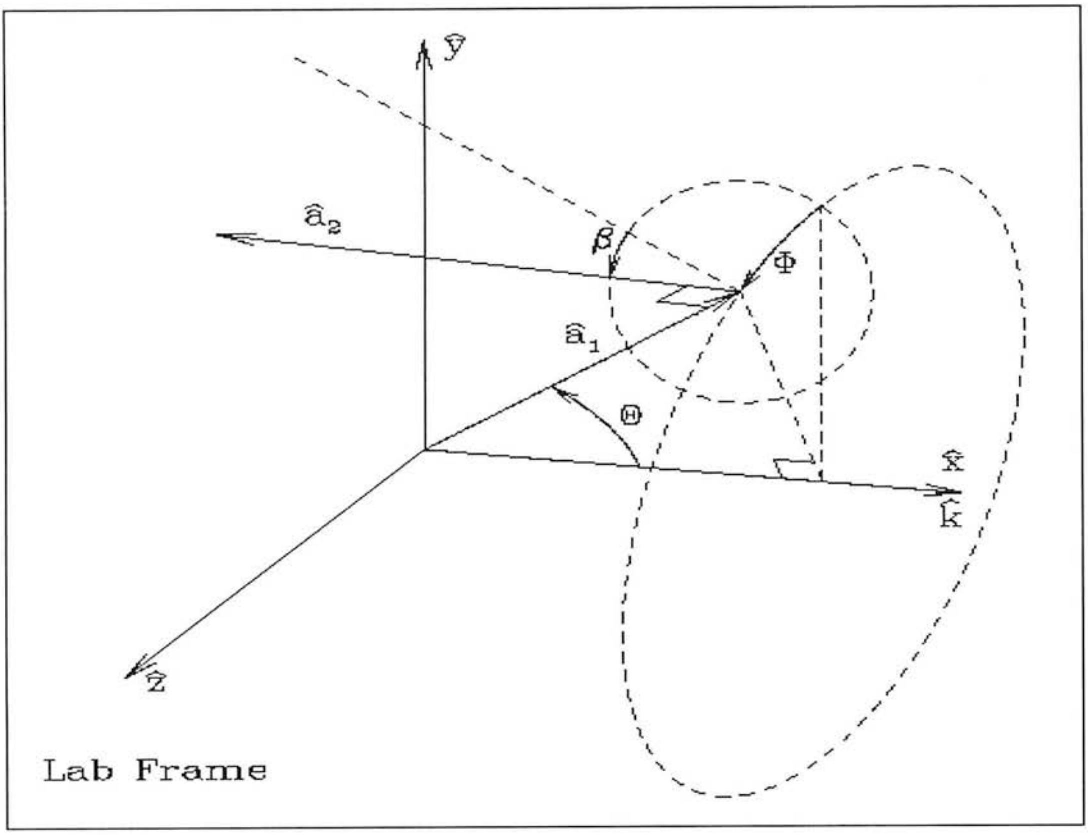

Figure 3.5: Description of target orientation in DDSCAT. The incident light propagates along $\hat{\mathbf{x}}$, with its two orthogonal components of $\mathbf{E}$ in the $\hat{\mathbf{y}}$ and $\hat{\mathbf{z}}$ directions. The target's axes are described by the unit vectors $\hat{\mathbf{a}}_1$ (along the longest axis), $\hat{\mathbf{a}}_2$ (orthogonal to this) and $\hat{\mathbf{a}}_3 = \hat{\mathbf{a}}_1 \times \hat{\mathbf{a}}_2$. The orientation of $\hat{\mathbf{a}}_1$ is specified by the angles Θ and Φ, which fix the angle between $\hat{\mathbf{a}}_1$ and $\hat{\mathbf{x}}$ and the rotation of $\hat{\mathbf{a}}_1$ about $\hat{\mathbf{x}}$. The angle β fixes the rotation of $\hat{\mathbf{a}}_2$ around $\hat{\mathbf{a}}_1$. Figure taken from Draine and Flatau (2000) — see this reference for a fuller description and examples.

Output from DDSCAT

Given this information, DDSCAT calculates a number of quantities. Those of which I have made use in this work are the following:

$$Q_{abs} = C_{abs}/\pi a^2 \tag{3.19}$$

$$Q_{sca} = C_{sca}/\pi a^2 \tag{3.20}$$

$$Q_{ext} = Q_{abs} + Q_{sca} \tag{3.21}$$

$$Q_{pol} = Q_{ext,\parallel} - Q_{ext,\perp} \tag{3.22}$$

in which Qs are efficiencies and Cs cross-sections for absorption, scattering and extinction, and $Q_{ext}, \|$ and $Q_{ext}, \perp$ refer to extinction efficiencies for the two orthogonal incident polarisation states (Draine, 1988).

From Q_{ext} and Q_{pol}, extinction and polarisation spectra for ensembles of grains can be obtained in the following manner:

$$\tau(\lambda) = N_{grain} \int_{a_{min}}^{a_{max}} n(a) C_{geo}(a) Q_{ext}(a, \lambda) da \tag{3.23}$$

$$P(\lambda) = N_{grain} \int_{a_{min}}^{a_{max}} n(a) C_{geo}(a) Q_{pol}(a, \lambda) da \tag{3.24}$$

where C_{geo} is the geometrical cross-section of the grain in question, N_{grain} the column density of grains (if $\int n(a)da = 1$) and a_{min} and a_{max} the limits of the size distribution to be considered. I have chosen a_{max} by inspecting plots of n(a) vs a for the grain size distribution, selecting a value of a_{max} where n(a) is acceptably small (see §3.3.3).

3.3 Parameters describing the dust grains

The model developed in this chapter seeks to predict extinction and polarisation in NGC1068 and GCIRS 7 for comparison with observations. Naturally, it should be based on a description of the obscuring material which is as realistic as possible. In this section I discuss the reasons for selecting particular values of the parameters necessary to describe the dust grains.

3.3.1 Optical constants

The complex refractive index $m(\lambda) = n(\lambda) + ik(\lambda)$ of a material governs the way in which it absorbs and scatters light. With some uncertainty, the complex refractive index of dust materials can be inferred from astronomical spectra or laboratory spectra of candidate substances. Accordingly there can be several choices of available optical constants.

Silicates

Perhaps the most widely-used set of optical constants are those of "astronomical silicate" (D&L; Draine, 1985). Their data were constructed so as to reproduce the observed infrared emissivity and the shape and strength of the Trapezium 9.7 and 18μm silicate features. Greenberg and Li (1996) point out that the astronomical silicate optical constants were derived assuming that the grains have no mantles, and they point out that the astronomical silicate fails to match the 9.7μm feature shape and the ratio of the 9.7 and 18μm absorptions in the BN object (Aitken et al., 1989). They favour instead the optical constants of amorphous olivine, which they say better reproduce the observations of the BN object.

At wavelengths shortwards of the silicate feature, the astronomical silicate and amorphous olivine optical constants have a similar wavelength dependence. The main differences are over the feature itself and at longer wavelengths[1]. The models I develop here consider only the wavelength dependence of polarisation at $\lambda < 10\mu$m and the shape of the 3.4μm C-H bond stretch, neither of which should differ appreciably whichever set of silicate optical constants is used. As the astronomical silicate optical constants are freely available I have used the recent, "smoothed" version, as described by Weingartner and Draine (2001). This also potentially has the advantage of allowing a slightly more direct comparison between the results I present in this thesis and the many other studies which have used the astronomical silicates.

The Carbonaceous Component

The Database of Optical Constants (Henning et al., 1999) contains numerous references to publications containing optical constants and related information for many carbonaceous materials. However, at the time of writing the only optical constants with sufficient wavelength resolution and coverage in the infrared are those of Li and Greenberg (2002) and Greenberg and Li (1996). Using the transmission spectrum of the Murchison meteorite, together with measurements of the density and mass absorption coefficient of a laboratory sample of hydrogenated amorphous carbon, Li and Greenberg (2002) were able to construct a complex refractive index for the organic dust component. This differed from their 1996 approach by concentrating

---

[1] plots comparing the two sets of optical constants can be seen in Fig.s 1 and 2 of Greenberg and Li (1996)

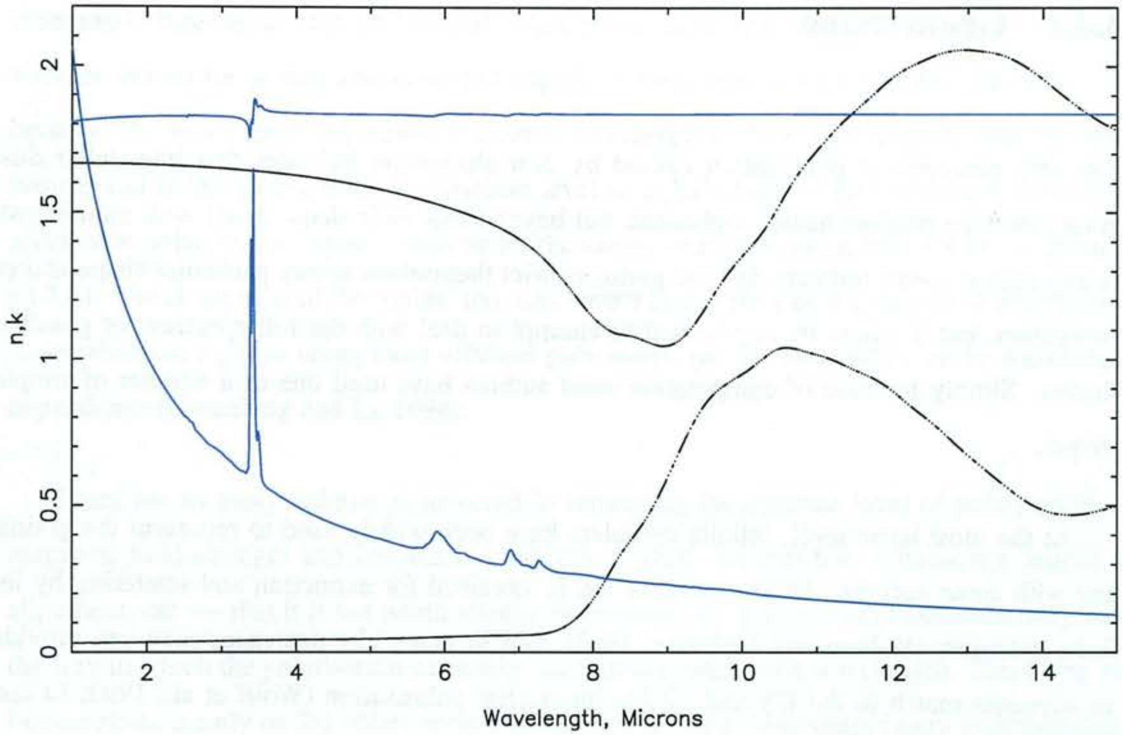

Figure 3.6: Optical constants for astronomical silicate and Li and Greenberg's organic material. Black curves: silicates, n (upper), k (lower). Blue curves: organics, n (upper), $k \times 9.0$ (lower).

on the Murchison meteorite data rather than on samples of processed ices from the EURECA satellite (Greenberg et al., 1995b). Their rationale for this is that the Murchison meteorite is a better representation of the heavily UV-processed grain mantles that should dominate in the diffuse ISM, whereas the EURECA samples are more like material freshly dispersed from a molecular cloud.

The attraction of this approach is that the 3.4μm spectrum of the Murchison meteorite bears a close resemblance to the observed feature in many diffuse ISM lines of sight and in NGC1068. The shape and strength of this band are of interest here, so this is a clear advantage. However, at longer wavelengths the similarity decreases and spectral features appear at 5-9μm which are not seen in the spectra of Galactic diffuse ISM dust (Pendleton and Allamandola, 2002). These features are weak compared to that at 3.4μm (and to the features in the EURECA sample), though, and given that I do not examine the details of polarisation and extinction at those wavelengths it is unlikely that the discrepancies will have a significant effect. I have therefore used the optical constants of Li and Greenberg (2002). The optical constants for both the silicate and hydrocarbon materials are shown in Fig. 3.6.

3.3.2 Grain shape

The very presence of polarisation caused by dust absorption indicates that interstellar dust grains must be predominantly aspherical, but beyond that their shape is not well established. In any case it seems unlikely that the grains restrict themselves to any particular shape and/or elongation, but it would be impractical to attempt to deal with the full spectrum of possible shapes. Simply for ease of computation most authors have used one of a number of simple shapes.

At the most basic level, infinite cylinders have been widely used to represent the grains, and with some success. Exact solutions can be obtained for extinction and scattering by infinite cylinders (Bohren and Huffman, 1983), and in many circumstances they can provide an adequate match to the UV and visible interstellar polarisation (Wolff et al., 1993; Li and Greenberg, 1997). However, they work less well at longer wavelengths and studies have been unable to reproduce the near-IR polarisation using infinite cylinders (Kim and Martin, 1994; Li and Greenberg, 1997). At the other end of the scale, Draine and Weingartner (1996) used an irregular composite of 13 cubes in a study of starlight torques on asymmetric grains.

Spheroidal particles can be a good compromise between the clearly unrealistic infinite cylinders and more realistic but computationally demanding shapes. Based on fits to the Trapezium silicate feature D&L find that oblate spheroids with a 2:1 axial ratio are a reasonable representation of dust grains, and are presumably more realistic than any form of cylinder. Hildebrand and Dragovan (1995) also favour oblate over prolate spheroids, and conclude that the axial ratio must be no greater than 3:1, with a best-fitting value of about 1.5:1. Greenberg and Li (1996), however, contend that the above studies use optical constants which do not well reproduce the shape of the silicate feature, and that the shape of the grains cannot reliably be deduced from that work. Their own calculations indicate that prolate grains are significantly better, and they note that prolate shapes can be explained by clumping of grains whereas oblate shapes cannot.

There is some difference in the wavelength dependence of polarisation of prolate and oblate grains (see e.g. Fig. 3.8, also D&L). Over the silicate feature, polarisation by prolate grains peaks at a slightly longer wavelength than oblate grain polarisation (using the D&L optical constants). Elsewhere, both prolate and oblate grains have a similar wavelength dependence, with the curves for prolate grains shifted slightly towards longer wavelengths. The difference between the two shapes decreases at shorter wavelengths. The main dissimilarity between prolate and oblate grains is in the absolute level of polarisation — prolate grains are half as efficient at polarising as oblate grains under the same conditions (the reason for this is given in §3.3.4). The elongation of the grains, too, can have a large effect on the degree of polarisation (more elongated grains being more efficient polarisers), but has little effect on its wavelength dependence (Greenberg and Li, 1996).

There are so many unknowns involved in estimating the absolute level of polarisation — magnetic field strength and orientation, aspects of grain composition influencing degree of alignment, etc. — that it is not worth attempting to calculate it here. I am concerned only with the way in which the polarisation caused by dust grains varies with wavelength. This being so, I concentrate mainly on 2:1 oblate spheroidal particles, using other shapes only to demonstrate that their use has a minimal effect on the results.

3.3.3 Size distribution of the cores and mantles

The wavelength dependence of absorption, polarisation and scattering all depend on the sizes of the particles involved. Clearly it would be unreasonable to expect dust grains to be of a single size, so many authors have proposed grain size distributions which, to a greater or lesser extent, fit the observations. Perhaps the best-known description of the size distribution of dust grains was put forward by MRN, who found that the extinction curve from $0.11 - 1\mu$m could be matched with graphite and silicate grains with the following power-law size distribution (the "MRN distribution"):

$$n_i(a)da = A_i n_H a^{-3.5} da,\ a(min) \leq a \leq a(max), \tag{3.25}$$

where a is the grain radius, $n_i(a)da$ the number of grains of material i with radius in the interval $a, a + da$ and A_i and n_H the abundance of material i and number density of hydrogen nuclei respectively. The best values of the limits $a(min)$ and $a(max)$ of the distribution were found to be 0.005μm and 0.25μm.

The average grain radius in the MRN distribution is governed by the limits $a(min)$ and $a(max)$:

$$< a > = \frac{\int_{a(min)}^{a(max)} a.a^{-3.5}da}{\int_{a(min)}^{a(max)} a^{-3.5}da} \tag{3.26}$$

$$= \frac{5}{3}\frac{\left(a\,(min)^{-1.5} - a\,(max)^{-1.5}\right)}{\left(a\,(min)^{-2.5} - a\,(max)^{-2.5}\right)} \tag{3.27}$$

$$\approx \frac{5}{3}\,a(min) \qquad\qquad a(min) \ll a(max). \tag{3.28}$$

In the 25 years since the original MRN paper it has become apparent that the MRN model does not explain all of the observations. For instance, it says nothing about the very small particles now widely thought necessary to explain the presence of near-IR emission bands in cool regions (§1.2). Updated size distributions for separate organic and silicate grains have been presented by Kim et al. (1994), Zubko et al. (1996) and Weingartner and Draine (2000), among others. Nevertheless, the MRN distribution has stood the test of time remarkably well and proved its worth as a rough description of the sizes of interstellar dust grains. It is relatively simple to use and manipulate and turns out to be useful when investigating the effects of varying the functional form of the size distribution, as I do in the case of NGC1068.

It is not obvious, however, that a size distribution which works for separate graphite and silicate grains will be appropriate for core-mantle-type dust. L&G favour instead a size distribution of the form

$$n(a) = n_0 \exp[-5(\frac{a - a_c}{a_i})^q] \tag{3.29}$$

in which a is the total grain radius, a_c the radius of the core and a_i a number governing the width of the distribution. I shall refer to this as the "L&G" distribution. The normalising factor $n_0 = 2\sqrt{5}/[\Gamma(\frac{1}{2})a_i]$ when $q = 2$; $\Gamma(\frac{1}{2}) = \sqrt{\pi}$. This equation implies that the size of the silicate core is held constant and the grain size varied by adding thicker and thicker mantles, which is certainly an oversimplification but one which is probably not unreasonable, especially if much of the grain volume is contained in the mantle (Chlewicki and Greenberg, 1990; Greenberg and Li, 1996).

The values of a_c and a_i needed to match the observations vary according to the grain shape and method of calculation, but for finite cylinders L&G found that $a_c = 0.070\mu\text{m}$, $a_i = 0.066$ and $q = 2$ gave the best fit to the average Galactic extinction and polarisation. The average size of the grains in the L&G distribution is given by

$$< a >= a_c + 0.2522 a_i \tag{3.30}$$

when $q = 2$.

As the L&G distribution has been optimised for core-mantle particles and can give a good fit to the observations, this is the one I have adopted for most of this work. The values of the parameters a_c, a_i, $a(min)$ and $a(max)$ in the distributions determine the relative numbers of grains of different sizes in the distributions and can be varied to improve the fit to the observations. This is something I investigate in the models and it turns out to be very important to the interpretation of the results — particularly where NGC1068 is concerned.

3.3.4 Grain alignment

For a population of elongated dust grains to polarise light at all, there must be a net alignment of their axes. A number of mechanisms have been proposed to explain this alignment, none so far entirely successful. Those which appear more relevant to the ISM as a whole are based on alignment by the Galactic magnetic field, as polarisation maps of the Galaxy trace out fairly well the magnetic field derived by other means (e.g. Hildebrand 2002). When thinking about alignment in a magnetic field, probably the most obvious process to spring to mind is the grains behaving like tiny compass needles and lining up with the field. However, it turns out that this kind of alignment is too easily destroyed to be viable in the ISM; it will be disrupted by even a modest rotational kinetic energy ($\sim kT$, Spitzer and Tukey, 1951).

More promising is the mechanism proposed by Davis and Greenstein (1951) in which the Galactic magnetic field **B** induces an internal field **M** in a paramagnetic grain. If the dust grains can be set spinning with a high enough angular velocity (by collisions with gas molecules, for example), the internal field will never be perfectly aligned with the external field. Instead it will have a component in the direction $\mathbf{M} \times \mathbf{\Omega}$, where $\mathbf{\Omega}$ is the angular velocity. The torque $\mathbf{M} \times \mathbf{B}$ removes components of $\mathbf{\Omega}$ perpendicular to **B**, so the grain's spin axis gradually comes to be parallel with the external field (more accurately, the spin axis precesses about **B**). Damping processes within the grain act to reduce the rotational kinetic energy, $J^2/(2I)$, by increasing the moment of inertia, I. This means that it is the short axis of the grain which rapidly becomes its spin axis and aligns along the magnetic field.

Unfortunately, a certain minimum magnetic flux density is required for the Davis-Greenstein mechanism to be effective, and this is about an order of magnitude greater than that observed in the Galaxy (Whittet, 1992, and references therein). Alignment can still be achieved if the grains' rotational kinetic energy can be increased or if the grains contain ferromagnetic inclusions; some combination of these effects may explain the observed grain alignment. Draine and Weingartner (1997) find that, under diffuse cloud conditions, the radiative torques produced by anisotropic starlight can efficiently align the grains with even a weak magnetic field.

Alignment by streaming of dust through gas and by anisotropic absorption of starlight is also possible. Radiation pressure, for example, can accelerate gas and grains by different degrees, causing streaming of one with respect to the other. Then collisions of grains with gas atoms will tend to align the grains with their long axes parallel to the streaming direction. The charge acquired by dust grains means that they tend only to stream effectively along magnetic field lines, with the result that the position angle of polarisation is perpendicular to the field. This mechanism seems not, therefore, to be relevant to the wider Galactic ISM, but what this means for NGC1068 is not clear. Radiation pressure can also align grains when the incident photons impart angular momentum to the dust. In regions where there is a high intensity of IR radiation, the dust and the radiation field can be at similar temperatures, and the disorientating effect of random thermal emission of photons from the grains is lessened. The cool absorbing dust in NGC1068 is thought to be heated by hotter, IR-emitting dust closer to the nucleus; perhaps this could mean that conditions there are suitable for grain alignment by anisotropic absorption of radiation.

Fortunately, the main issue here is that the grains in NGC1068 are somehow preferentially orientated in one direction, as shown by the presence of significant IR polarisation (§3.1). The next question, then, is how best to represent this alignment, striking a balance between a realistic description and computational efficiency. In the Davis-Greenstein mechanism the spin axis of the dust grains precesses about a direction parallel to the magnetic field. The angle that the spin axis makes with this alignment direction is the precession cone-angle, ζ, which can range from 0°to 90°. When calculating extinction and polarisation, a full treatment of grain alignment would involve calculations over the full range of possible ζ values, which potentially could be very time-consuming indeed. However, if it is the wavelength dependence of polarisation rather than its absolute value which is of interest, it might be imagined that the polarisation from pairs of orientations at 90°to each other will cancel, leaving only the contribution from the orientation with $\zeta = 0$. The approximation of ignoring all orientations with $\zeta \neq 0$ is known as perfect spinning alignment (PSA) and has been shown to be quite adequate if the absolute value of polarisation is not required to be known (Chlewicki and Greenberg, 1990; Greenberg and Li, 1996).

Fig. 3.7 shows the orientations of the oblate and prolate spheroids that I have considered, relative to the direction of propagation of the incident light wave. It is assumed that the magnetic field lies in the plane of the sky, that is, perpendicular to our line of sight. In terms of the DDSCAT input parameters describing target orientation, both spheroids have $\beta = 0°$, $\Theta = 0°$, $\Phi = 90°$ (§3.2.2). As I have been using the PSA approximation, the angle ζ is always zero. It can be seen from this diagram that, as the grains spin about their short axis, the cross-section that the oblate spheroid presents to the incident light beam does not change. The cross-section of the prolate grain, however, goes from being a 2:1 ellipse to a circle and back again as the grain rotates. This means that prolate grains are half as efficient at polarising as oblate grains under the same circumstances.

3.4 First steps: testing DDSCAT

Having established a framework for describing the dust grains, it is now possible to attempt some calculations. As a first check on the functioning of the code, calculations were done for the test case of a rectangular array of 192 dipoles, with size parameter $2\pi a/\lambda = 1$ and a constant refractive index $m = 1.33 + 0.01i$. The results of this calculation were the same as those given by Draine and Flatau (2000), indicating that DDSCAT was correctly installed and running.

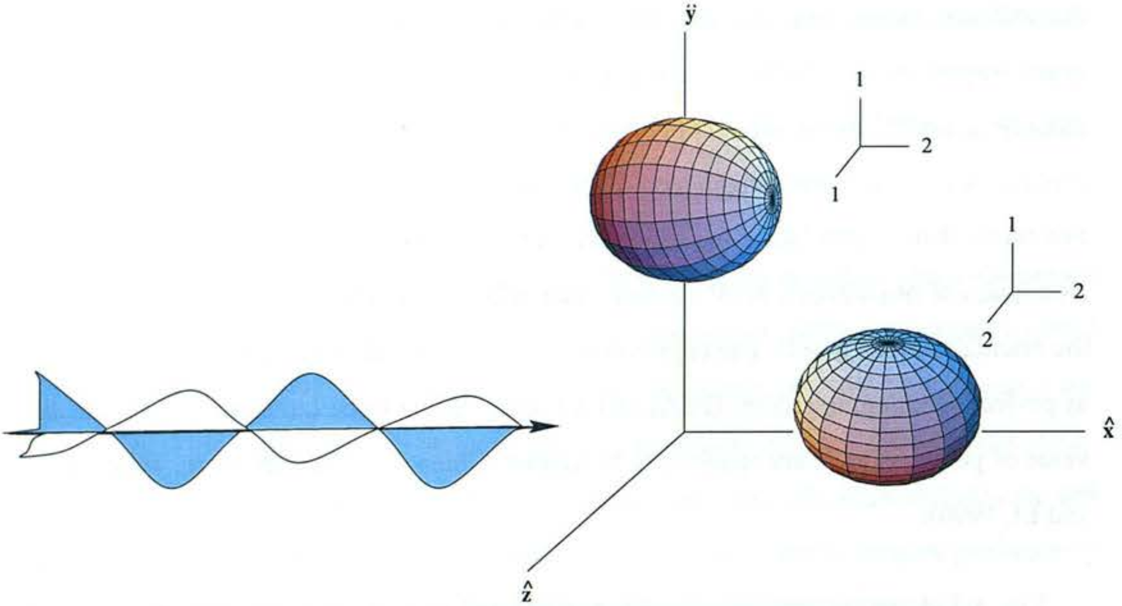

Figure 3.7: Orientation of a 2:1:1 prolate and a 2:2:1 oblate spheroid in the perfect spinning alignment approximation. In DDSCAT the two orthogonal polarisation states of the incident light are orientated along $\hat{\mathbf{y}}$ and $\hat{\mathbf{z}}$ The external magnetic field, $\mathbf{B}$, is in the $\hat{\mathbf{y}}$ direction and the grains' spin axis is parallel to this. Spheroid graphics taken from Weisstein, 2002.

The DDSCAT applicability criteria mean that the code should give reliable results for the parameters used in the models presented here. As an additional check, DDSCAT calculations for silicate spheres were compared with the exact results obtained using the Mie theory code, BHCOAT (Bohren and Huffman, 1983). The extinction efficiency, Q_{ext}, agrees to within about 2% of the exact value, as shown in Fig. 3.8. This is true even for quite small numbers of dipoles — the curves in Fig. 3.8 were calculated using only 2176 dipoles.

The correct results were obtained for spherical particles, but it also seemed sensible to check that the code was correctly set up to deal with spheroidal targets. To this end, Q_{abs} and Q_{pol} as a function of wavelength were calculated for small silicate spheroids. These curves could then be compared with the plots of Q_{abs} and Q_{pol} vs λ presented by D&L using the same optical constants. Again, very good agreement was obtained (Fig. 3.8).

The above tests were for single sizes of particle, but in the models it would also be necessary to integrate over a distribution of sizes. Simpson's rule integration over the MRN size distribution, from $a_{min} = 0.005\mu$m to $a_{max} = 0.3\mu$m gave the same values of C_{ext} as those obtained by Pendleton (1987) using BHCOAT. The step size used in the integral was also inves-

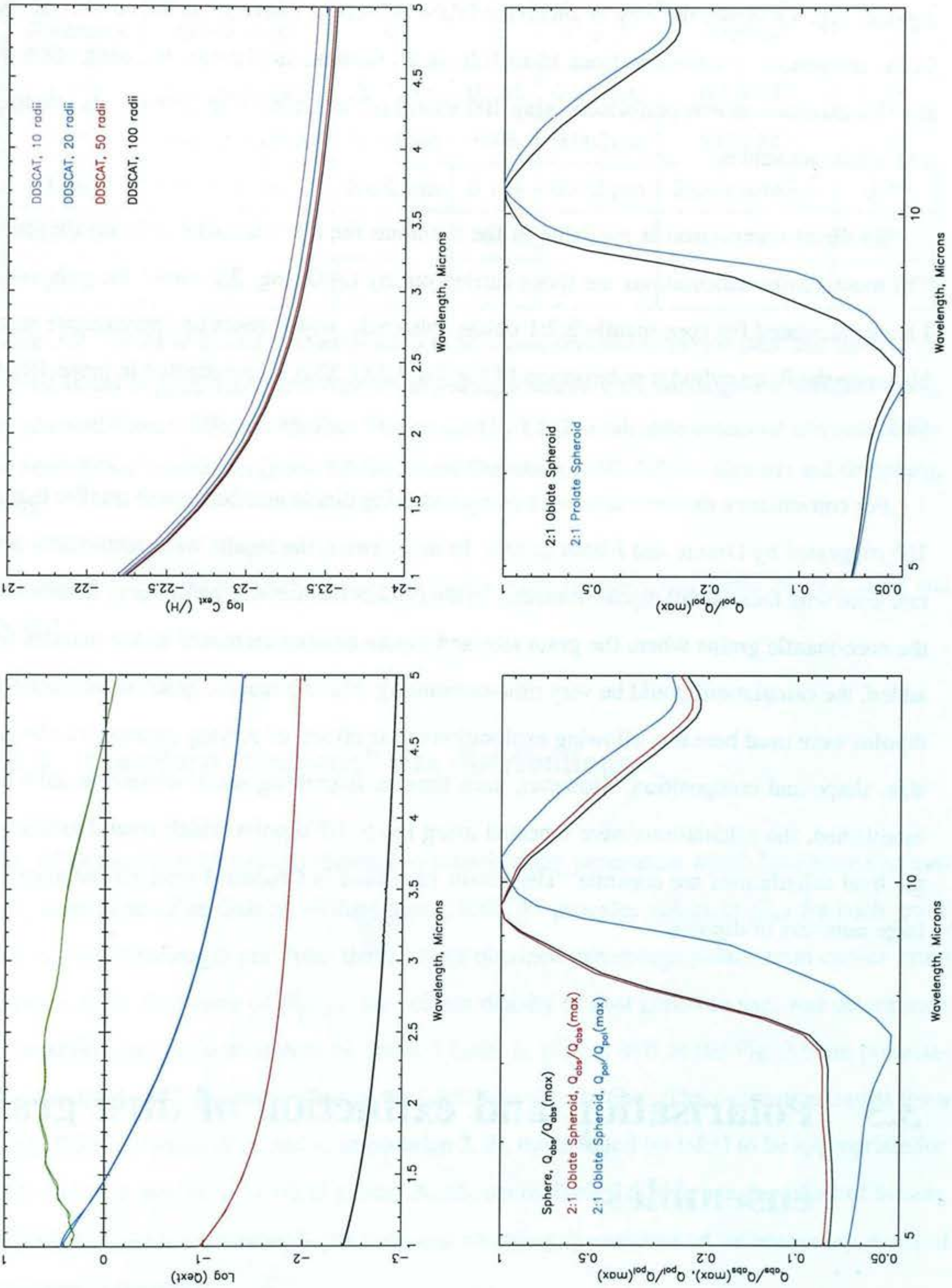

Figure 3.8: Top left panel: log of the extinction efficiency, Q_{ext}, of silicate spheres of various radii. The curves calculated using DDSCAT (discrete dipole approximation) and BHCOAT (Mie theory) agree very well. Black: 0.01μm, red: 0.1μm, blue: 0.3μm, green: 1.0μm. Top right: C_{ext}/H for silicate spheres, integrated over the MRN size distribution. The quantity C_{ext}/H was used for ease of comparison with the Mie theory results presented in Pendleton (1987); H=7.763$\times10^{24}$cm^{-2}. Lower panels: Q_{abs} and Q_{pol} for 0.1μm 2:1 oblate and prolate silicate spheroids, calculated using DDSCAT. The results are in good agreement with Figs 6a & b of D&L.

tigated. Fig. 3.8 shows the way in which the DDSCAT results converge as the number of steps in the integration is increased from 10 to 100. In all further calculations, the integration over the size distribution was performed using 100 values of the grain radius between its maximum and minimum values.

No direct comparison is available in the literature for the spheroidal core-mantle grains. The most similar calculations are those carried out by L&G. Fig. 3.9 shows the polarisation I have calculated for core-mantle 2:2:1 oblate spheroids, which bears an approximate resemblance to the finite cylinder polarisation of Fig 9 in L&G. This is investigated in more detail in §3.5.

For convenience the test cases were computed using dipole numbers much smaller than the 10^4 suggested by Draine and Flatau (2000). In many cases, the results were remarkably accurate even with these small dipole numbers. In the models themselves, particularly in the case of the core-mantle grains where the grain size and dipole number increased as the mantles were added, the calculations could be very time-consuming. For this reason, quite small numbers of dipoles were used here too, allowing exploration of the effects of varying parameters like grain size, shape and composition. However, each time an interesting result seemed to have been established, the calculations were repeated using the $> 10^4$ dipoles which should ensure that the final calculations are accurate. The results presented in Chapter 4 were all obtained with large numbers of dipoles.

3.5 Polarisation and extinction of dust grain ensembles

Having established that DDSCAT was producing reliable results, the next step was to calculate the polarisation and extinction of a realistic distribution of core-mantle grains. In this section I show that under many circumstances, core-mantle grains should indeed be expected to produce an appreciable increase in polarisation over the 3.4μm absorption, and I illustrate the effects (or lack of them) of varying the shape, elongation and size distribution of the dust grains.

Reference	Grain shape	a_c	a_i	$< a >$	Method	f_{carb}
L&G	Finite cylinder	0.07μm	0.066	0.087μm	MGEMT	0.28
L&G	Infinite cylinder	0.042μm	0.08	0.062μm	MGEMT	0.54
L&G	Infinite cylinder	0.030μm	0.104	0.056μm	Exact solution	0.76
L&G2	—	—	—	—	—	0.25
C&G	—	—	—	—	—	~ 0.90

Table 3.2: Values of a_c and a_i used by L&G to fit polarisation and extinction data, and some of the various values of f_{carb} which have been calculated/suggested for core-mantle grains. MGEMT stands for Maxwell-Garnett Effective Medium Theory, used by L&G to calculate extinction and polarisation for ensembles of coated dust grains. L&G2: Li and Greenberg, 2002. C&G: Chlewicki and Greenberg, 1990.

In Chapter 4 I go on to apply the models to the more complex real cases of NGC1068 and GCIRS 7.

3.5.1 Standard "Galactic" size distributions

Fig. 3.9 shows the polarisation predicted by models using parameters which have been successfully used to describe Galactic diffuse dust. DDSCAT provides values of Q_{pol} for each grain size at each wavelength and from these I have obtained percentage polarisation curves using equation 3.24. The value of N_{grain}, the column density of dust grains to use, was determined by requiring that the polarisation be 3% at 3.1μm. In the top half of the Fig. 3.9 are polarisation spectra from 2:1 spheroids using the L&G size distribution. The two curves result from using different values of a_c and a_i in equation 3.29, those found by L&G to be appropriate for finite and then infinite cylindrical grains. As shown in Table 3.2, this has the effect of biasing the distributions to smaller or larger sizes and changing the amount of carbonaceous material contained in the grains.

Probably the most obvious feature of the left-hand panels of Fig. 3.9 is that there is indeed a strong increase in polarisation at the wavelength of the 3.4μm band. If dust with properties like those derived for Galactic diffuse dust is sufficiently abundant, elongated and aligned to give 3% polarisation in the near-IR continuum, a polarisation excess of 2-3% should be seen

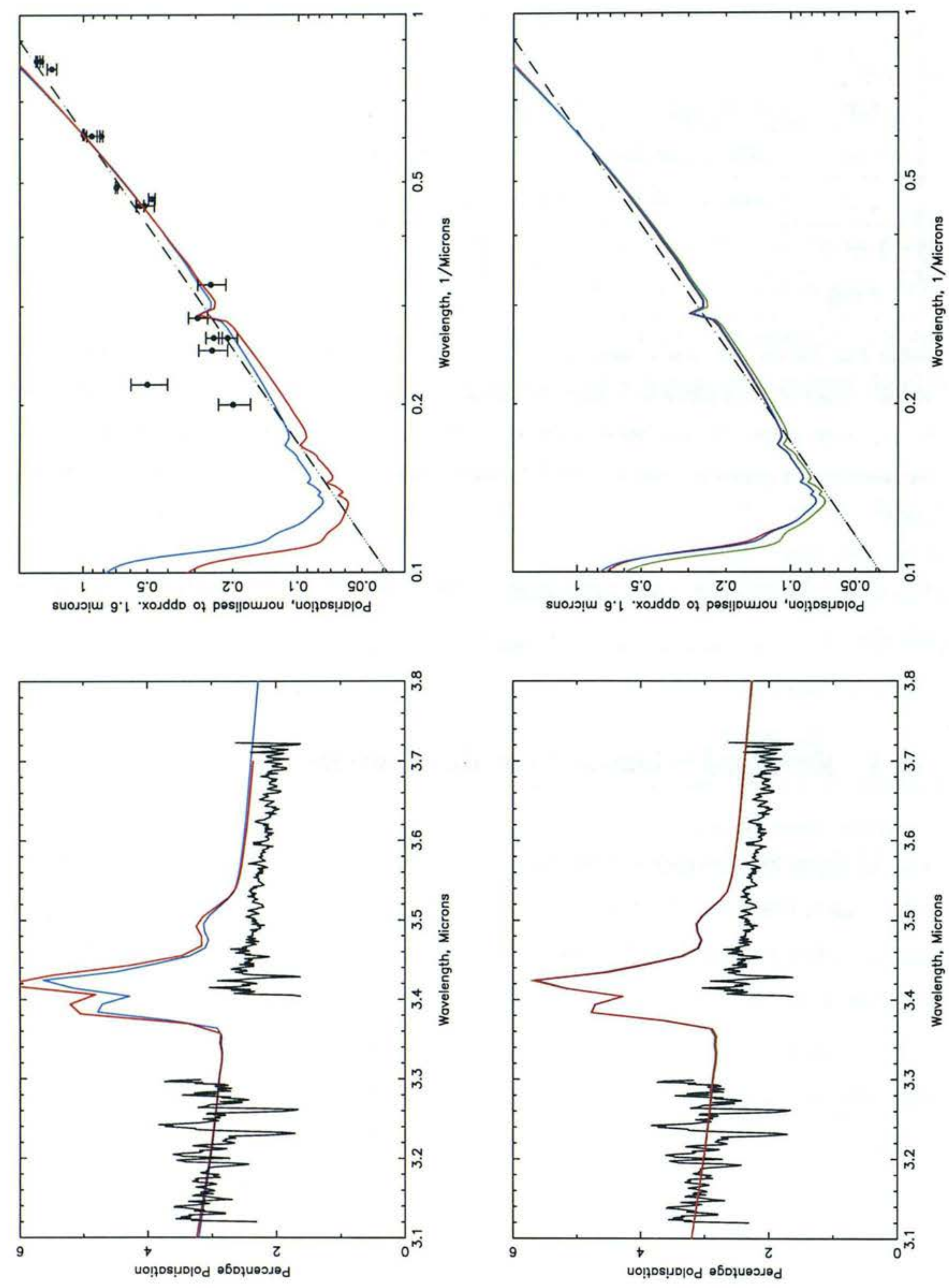

Figure 3.9: Polarisation calculated for models using "standard" Galactic parameters. Top left: blue line — L&G size distribution, $a_c = 0.07\mu\mathrm{m}, a_i = 0.066$, 2:1 oblate spheroids. Red line — same, but with $a_c = 0.042\mu\mathrm{m}, a_i = 0.08$. The observed polarisation of NGC1068 is also shown. Top right: same, but over 1-10μm and normalised to 1 in the H-band. Points show the observed polarisation of Cyg OB2 #12, the dashed line is a $\lambda^{-1.8}$ power-law, to aid comparison with L&G. Bottom left: the same L&G size distribution, but for 2:1 prolate (green) and 4:1 oblate (red) spheroids. 2:1 oblate spheroids are shown for comparison (blue). Bottom right: as left, but from 1-10μm.

across the feature. Our observations of NGC1068 are shown for comparison, and it is clear that such an increase would be plainly visible in good-quality data like these.

The main rationale for looking at two slightly different versions of the L&G distributions is that the fraction of the grains which is carbonaceous, f_{carb}, differs between the two. As part of the object of this modelling is to predict the size of any increase in polarisation over the 3.4μm C-H bond stretch, an important factor will be the amount of carbonaceous material contained in the grains. Li and Greenberg (2002) note that the mantle volume fraction, $f_{carb} = V_{carb}/(V_{carb} + V_{sil})$, can be obtained from quantities which can be deduced from observations or laboratory measurements:

$$\frac{V_{carb}}{V_{sil}} \approx \left(\frac{\tau_{3.4}}{\tau_{9.7}}\right)\left(\frac{\rho_{sil}}{\rho_{carb}}\right)\left(\frac{\kappa_{sil}^{9.7}}{\kappa_{carb}^{3.4}}\right) \tag{3.31}$$

where $\tau_{3.4}$ and $\tau_{9.7}$ are the observed optical depths, ρ_{sil} and ρ_{carb} the mass densities of the dust materials and $\kappa_{sil}^{9.7}$ and $\kappa_{carb}^{3.4}$ the mass absorption coefficients of the bond stretches. Using estimates in the literature for all of these quantities, Li and Greenberg (2002) find that $f_{carb} \approx 0.25$ (see also Tielens et al., 1996).

However, there is considerable uncertainty in the numbers used to calculate f_{carb}. An independent estimate can be found from the thickness of mantle which must be added to the silicate cores in the L&G distribution in order to match the observed extinction and polarisation. f_{carb} can be obtained by integrating over the volumes of the whole grains and the silicate cores:

$$\begin{aligned} V_{carb} &= V_{total} - V_{sil} \\ &= \int_{a_c}^{a_{max}} \frac{4}{3}\pi a^3 n\left(a\right)\, da - \frac{4}{3}\pi a_c^3 n\left(a_c\right) \\ f_{carb} &= \frac{V_{carb}}{V_{total}} \end{aligned} \tag{3.32}$$

where a stands for total grain radius, a_c for the core radius, as in equation 3.29. When $a_c = 0.07\mu$m and $a_i = 0.066$, as found by L&G for finite cylinders, it turns out that $f_{carb} = 0.28$. For infinite cylinders (MGEMT solution), though, $a_c = 0.042\mu$m and $a_i = 0.08$, giving $f_{carb} = 0.54$. Chlewicki and Greenberg (1990) give a different f_{carb} again, asserting that "about 90% of the volume of core-mantle grains is contained in the mantle". These figures are summarised in (Table 3.2).

Fig. 3.9 illustrates the difference in polarisation between using the a_c and a_i given by L&G

for finite and infinite cylinders, with their differing values of f_{carb}. This difference is reflected in the magnitude of the polarisation increase over the 3.4μm feature; the curve from grains with the smaller a_c and larger a_i shows the larger polarisation excess. However, even the grains with $f_{carb} = 0.28$, at the lower end of the range of estimated values, show a sizeable polarisation feature.

There is still a little room for caution. In calculating these polarisation spectra, I have used the values of a_c and a_i which L&G found gave the best match to the interstellar extinction and polarisation for *cylinders*. It is quite likely that these are not the most appropriate values for oblate spheroids, especially with the different optical constants and method of calculation I have used. In the top right panel of Fig. 3.9, however, I have plotted the observed polarisation of the line of sight towards the luminous star, Cyg OB2 #12 (Martin et al., 1992, and references therein). The dust in this line of sight is thought to be representative of the diffuse ISM (Whittet et al., 1997), so the calculated polarisation should follow the observed points. The curve calculated using a_c and a_i for finite cylinders is quite successful in this respect, performing about as well as L&G's own curve (see their Fig. 9). This indicates that these grains are a reasonable representation of dust in the diffuse ISM, something which will come in useful when I model the dust towards GCIRS 7. The infinite cylinder values are perhaps less successful, though the curves only really diverge at longer wavelengths where there is no observational data.

Fig. 3.9 also illustrates the effect of changing the shape of the grains. The lower panels compare 2:1 prolate and 4:1 oblate grains with the 2:1 oblate particles, all with $a_c = 0.07$ and $a_i = 0.066$. It is clear that, as discussed in §3.3.2, there is very little difference between the curves. What difference there is comes at wavelengths much longer than 3.4μm, particularly around the silicate feature. Although the assumption used in these models that all the grains are 2:1 oblate spheroids is undoubtedly an oversimplification, Fig. 3.9 suggests that it is unlikely to dramatically influence the results.

3.5.2 Changing grain size

Changing f_{carb} will clearly influence the behaviour of the polarisation, but Fig. 3.9 hints that changing the grain size will also have an effect. In the panels comparing distributions with different a_c and a_i, the slope of the polarisation differs, as well as the magnitude of the polarisation over the 3.4μm feature. This is not unexpected; Q_{ext}, and therefore Q_{pol}, are functions of grain size. In §1.3 I mentioned speculation that the size distribution of dust grains in active galaxies like NGC1068 might differ from that derived for diffuse Galactic dust, so in this section I explore the effects on extinction and polarisation of altering the size of the dust grains.

Fig. 3.10 shows polarisation curves calculated for single sizes of dust grain. As the grain size increases, a number of effects are immediately obvious. Firstly, the wavelength at which the polarisation peaks, λ_{max}, shifts to longer values. At the same time, the maximum value of Q_{pol} increases. When the polarisation is calculated over 3-4μm, though, a clear decrease in the strength of the 3.4μm polarisation excess is evident. This is because of the reduced feature-to-continuum absorption ratio in larger grains; for the same amount of continuum absorption, large grains will exhibit a weaker 3.4μm feature than small grains, and this is reflected in the polarisation of the feature. The shape of the 3.4μm band also changes. As the particles increase in size, the extinction becomes less dominated by absorption and scattering starts to play a part. Rather than the absorption and polarisation smoothly increasing over the feature, they actually dip at the short end of the band, before rising again. Fig. 3.10 shows the 3.4μm band in polarisation, but the same effect can be seen in absorption in Fig. 4.7.

The weakness of the 3.4μm polarisation excess in large grains means that caution must be applied when attempting to predict the size of this excess in an unfamiliar grain population, such as that in NGC1068. If the particles are assumed to be smaller than they in fact are, there is a risk of unfairly ruling out the core-mantle dust model on the basis that a large excess is not seen in the data. Fortunately, as we shall see in Chapter 4, the wavelength dependence of the polarisation can be used to constrain to some extent the size distribution of the dust. Equipped with some understanding of the way in which various factors can affect dust grain polarisation, we are now ready to apply these models to the real situations of NGC1068 and GCIRS 7.

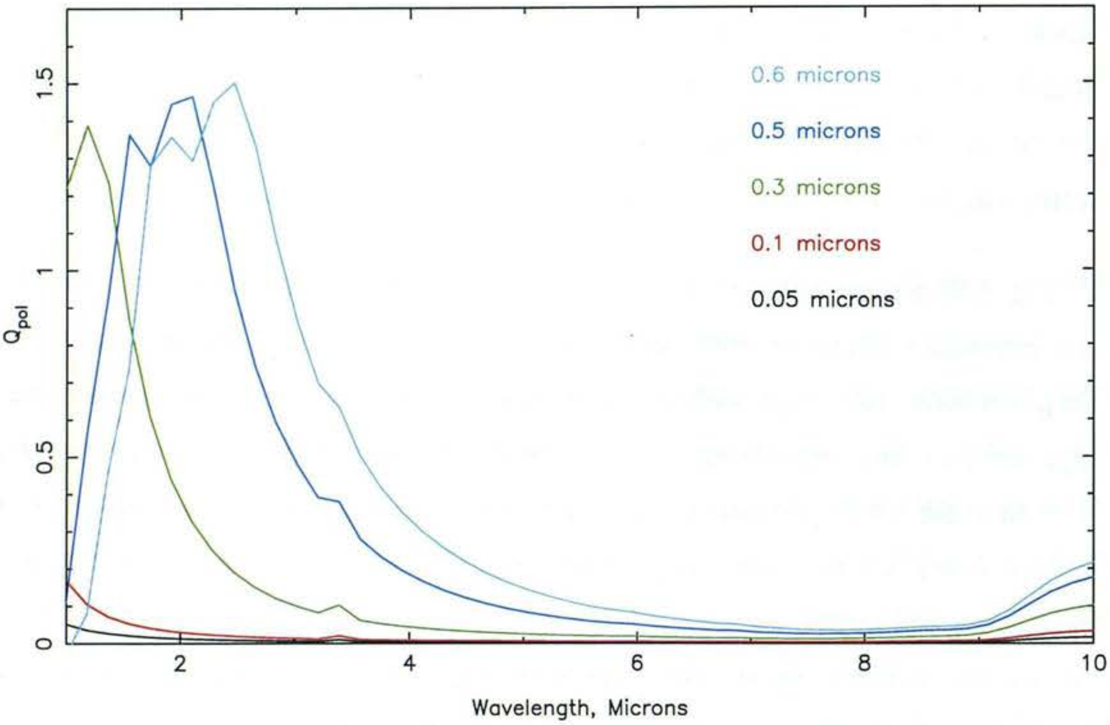

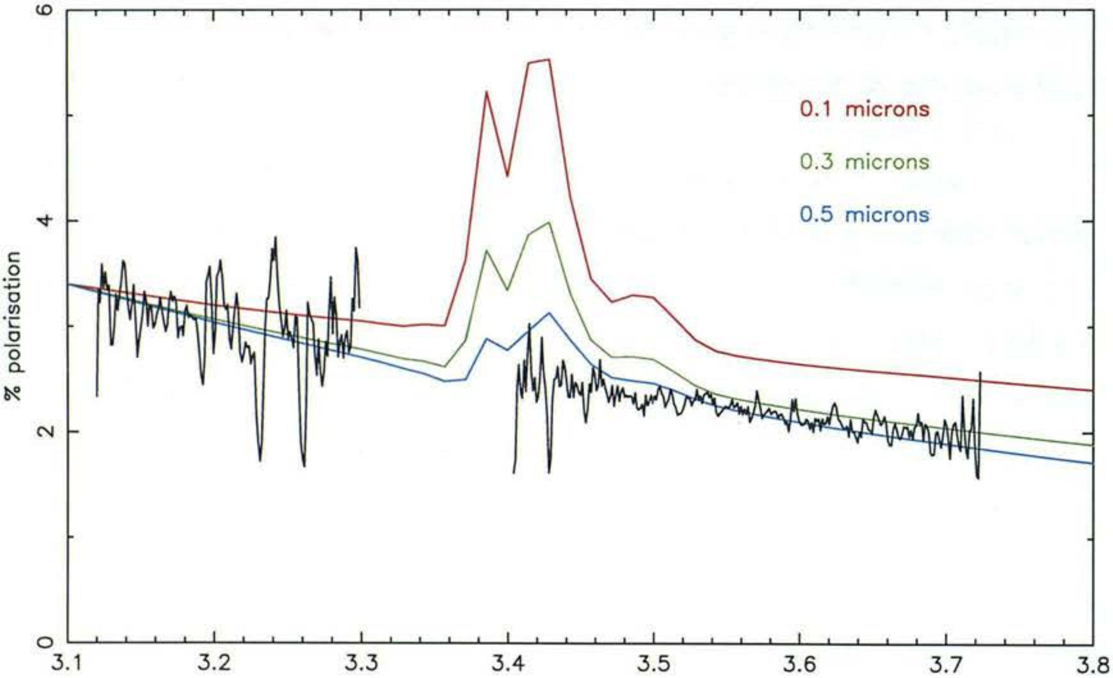

Figure 3.10: The effect of grain size on polarisation. Top: Q_{pol} at 1-10μm for single sizes of 2:1 oblate spheroids. Bottom: percentage polarisation at 3-4μm for selected single grain sizes.

CHAPTER 4

The Aligned Grains in NGC1068 and GCIRS 7

I have now established that, in many situations, a sizeable increase in polarisation over the 3.4μm feature can be expected if the core-mantle dust model is correct. However, the magnitude of this increase will be related to certain characteristics of the core-mantle grains, particularly their size. The size of the polarising dust grains has been fairly well established for grains in the Galactic diffuse ISM, but the situation in NGC1068 is much less clear. The complicated region of stars, gas and dust which is observed in this AGN means that the traditional ways of estimating dust grain sizes — extinction and polarisation curves — cannot be used in a straightforward manner, if at all. In this chapter I investigate the extent to which the available polarisation data can be used to constrain the grain sizes in NGC1068. I then examine the conclusions we can draw regarding the core-mantle model of dust grain structure. I also discuss the spectra of the 3.4μm and 9.7μm features themselves and the resemblance they bear to those observed in other, very different, lines of sight.

4.1 The size of the polarising grains in NGC1068

4.1.1 Useful data

As illustrated in §3.5, the wavelength of peak polarisation, λ_{max}, is related to the size of the polarising particles: larger grains have their peak at longer wavelengths than smaller grains. λ_{max} is known to vary in different Galactic lines of sight, with the most pronounced departures observed in lines of sight which pass through dense molecular clouds. In a dense cloud, λ_{max} can be about 0.9μm, whereas the average diffuse cloud value is closer to 0.55μm (Whittet, 1992). This increase in λ_{max} is usually interpreted as evidence for coagulation of small grains in the dense environment of the molecular cloud (e.g. Martin and Whittet, 1990). In the Magellanic clouds, conversely, λ_{max} is typically shorter than Galactic values, indicating that the polarising grains are smaller (Rodrigues et al., 1997).

The large amount of dust in the nucleus of NGC1068 means that little visible-wavelength light is transmitted, and the polarisation in the optical is caused instead by scattering off dust or electrons. Therefore if λ_{max} of the dichroic polarisation is comparable to that of Galactic dust, we cannot directly measure it and thereby determine the grain sizes. However, Fig. 3.10 shows that the slope of the infrared continuum polarisation is related to the size of the polarising grains, so in principle the wavelength dependence of the near-IR polarisation could also be used to investigate the size distribution of the dust grains. What reliable near-IR polarisation data, from dichroic absorption, do we have for NGC1068? As discussed in §3.1, the J-band data point must be discarded, as it is largely or wholly due to scattering off dust or electrons. The case of the H-band point is less clear. The polarisation measured at this wavelength is likely to be from a mixture of scattering and dichroic polarisation, but if an estimate could be made of the relative flux and polarisation of each component then the percentage polarisation from dust absorption could be established. Some figures do exist: Antonucci and Miller (1985) find that the UV and optical polarisation of NGC1068 is $\sim$16% and grey, so this figure should also be valid in the IR. After correcting the J-band polarisation of NGC1068 for dilution by starlight, I find that it is about 10-20%, depending on the method of evaluating the stellar contribution (Fig 3.3) — consistent with the 16% of Antonucci and Miller (1985). Young et al. (1995) find that the H-band flux comes in approximately equal parts from dust absorption and electron scattering, which, given the observed H-band polarisation of roughly 8% (Fig. 3.3), would suggest that the polarisation of the dichroic component is $\lesssim 6\%$. However, the uncertainties at every stage of this calculation are large enough to make this figure extremely unreliable and I do not further consider the H-band polarisation.

This leaves observations of polarisation in the K, L and M bands. As pointed out in §3.1, the polarisation at K and L should be almost wholly due to absorption by aligned dust grains. It is therefore important that the polarisation predicted by a particular model is consistent with these data. In particular, any good grain model should be able to match the L-band spectropolarimetric data. This will entail predicting the correct slope of the continuum polarisation from 3.1-3.7μm. At this stage it is worth recalling one of the simplifications used in the modelling of the polarisation. As discussed in §3.1, the temperature gradient that is likely to be present across the dust in NGC1068 will mean that short-wavelength radiation will suffer more absorption than longer-wavelength radiation. As polarisation depends on column density (Eq.3.24), more polarisation would then be observed at the short end of the L band than at the long end. This could have the effect of increasing the slope of the polarisation that we observe, independent of grain size. However, if the optical depth in the L-band is small, almost all the light at any wavelength in the band is transmitted and this effect can only be small. Extinction estimates to the hot dust source in NGC1068 range from A_V=12 to A_V=45 (see §4.3), and a standard Galactic $\lambda^{-1.75}$ extinction law therefore implies L-band extinctions of 0.5-1.75. This, and the quite slow change of Q_{pol} with wavelength in the IR (e.g. Fig. 3.8), suggests that it would be difficult to obscure shorter wavelength emission much more effectively than that at longer wavelengths. These factors, combined with the small range of wavelengths covered by the spectropolarimetry, means that this effect can probably be neglected.

The final piece of evidence, the M-band polarisation, comes after the 70°flip in position angle has been observed. It is therefore a measure of polarised dust emission and I do not attempt to find models which fit the M-band data.

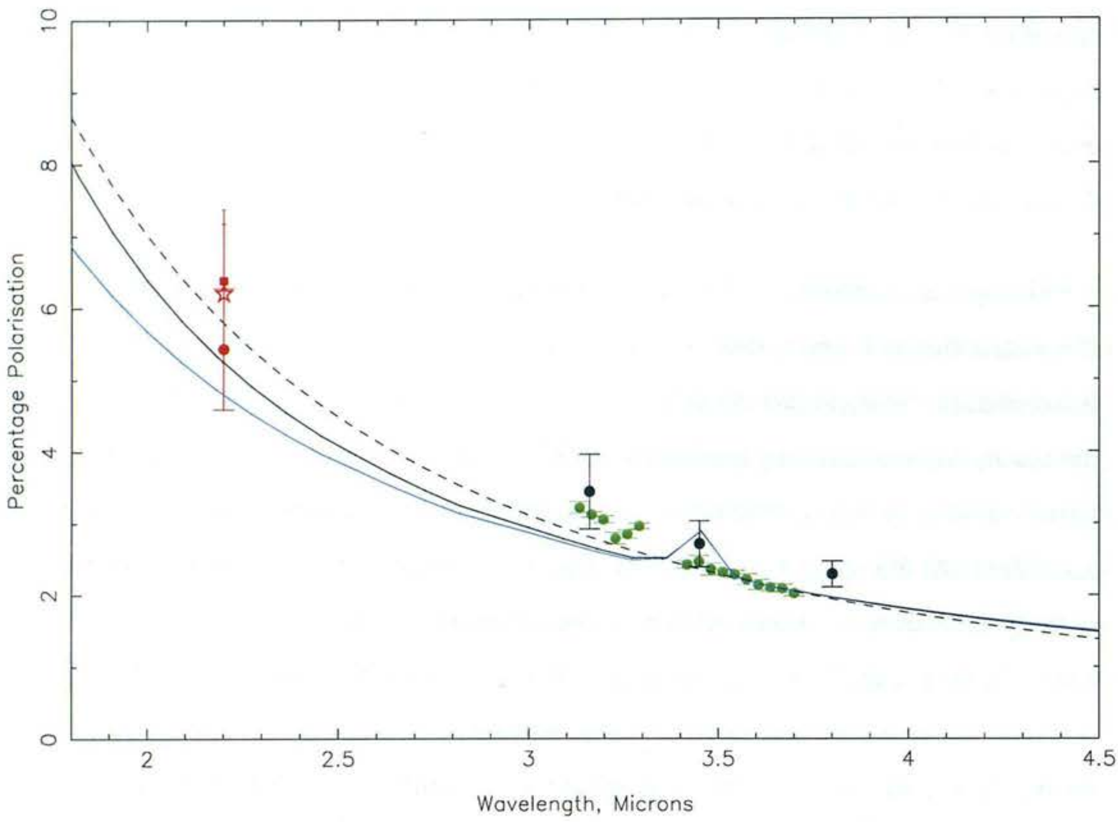

Figure 4.1: Polarisation from Galactic dust size distributions. The black line is the L&G distribution with the values of a_c and a_i that L&G used for finite cylinders. The blue line is the MRN $a^{-3.5}$ power-law distribution. Also shown is a power-law with index $\beta = 2.0$ (dashed line). All the curves have been normalised to the data point at 3.6μm, which is outside the 3.4μm feature. The L-band data are from Bailey et al. (1988) and the present work. For the K-band points, see §3.1.

4.1.2 Sizes appropriate to the Galactic diffuse ISM

Fig. 4.1 shows the polarisation calculated for grain sizes which have been found to be appropriate for dust in the Galactic diffuse ISM. The polarisation has been normalised to the 3.6μm point as the spectrum in this region is smooth and free of undivided telluric lines and the errors here are very small. The different weightings given to grains of different sizes in the distributions means that the two curves have different slopes. The MRN distribution, in which most grains are close to the minimum size, has its peak at a shorter wavelength than the L&G curve and therefore a shallower slope in the IR, where the polarisation tails off. Despite the difference in slope, both curves are consistent with the K-band point.

The curves do, however, underestimate the polarisation between 3.1 and 3.3μm. This may be an indication of the size distribution of the polarising dust grains in NGC1068. In a study of 18 reddened stars, Martin et al. (1992) find that the slope of the polarisation between the K and L bands for almost all the stars can be represented by a power-law of index $\beta < 2.0$. Only one of the lines of sight shows the 3.1μm ice absorption band and none is likely to be intrinsically polarised, which suggests that their polarisation is caused by grains in the diffuse ISM. This power-law is shown in Fig. 4.1, and it too clearly underestimates the 3.1-3.4μm polarisation. This implies that the slope of the polarisation of NGC1068 is different from that typically observed in Galactic lines of sight.

At higher spectral resolution, the L-band polarisation of Galactic objects has also been measured by Nagata et al. (1994). In their sample of five objects, two or three seem to show a fairly steep slope in polarisation at 3.1-3.7μm, though it is difficult to be certain with a spectral resolution of $\Delta\lambda/\lambda \sim 40$. Two of these, "object 16" and "object 33", have enhanced polarisation over the 3.1μm ice band, so the steep L-band slope may be simply the tail of the ice band polarisation. This was the explanation used by Ishii et al. (2002) to explain the steep gradient of the polarisation of IRAS18511, which also has an ice band. GCIRS 7, on the other hand, has both ice absorption and a very flat L-band polarisation spectrum (Adamson et al., 1999), but this object is suspected of being intrinsically polarised (Bailey et al., 1984). The evidence is rather unclear at present, but there are indications that polarisation spectra of lines of sight dominated by diffuse interstellar dust may have shallower L-band slopes than we observe in NGC1068.

If this is the case, then the difference in slope suggests that we should look for size distributions which provide a better fit to the L-band polarisation. It is worth noting that Young et al. (1995) were able to fit the H- and K-band polarisation of NGC1068 reasonably well using a dichroic component with $\lambda_{max} = 0.55\mu$m, the average Galactic value. However, they did not have these new spectropolarimetric data with which to further test their fit. Moreover, studies of Galactic lines of sight show no correlation between the slope of the 1-5μm polarisation and the value of λ_{max} (Martin et al., 1992) — it seems that the large end of the grain size distribution is relatively unaffected by environmental factors that can induce major changes in the smaller grains (coagulation, for example). For these reasons, I shall now go on to explore whether other dust grain size distributions can provide a better match to the observed polarisation of NGC1068.

L&G or MRN?	a_c or $a(min)$	a_i or $a(max)$	$< a >$	f_{carb}	Fig.
L&G	0.07μm	0.066	0.087μm	0.28	4.1
MRN ($a^{-3.5}$)	0.005μm	0.3μm	0.008μm	0.50	4.1
L&G	0.45μm	0.42	0.56μm	0.28	4.2
MRN ($a^{-3.5}$)	0.45μm	0.74μm	—	0.32	4.2
MRN ($a^{-2.5}$)	0.45μm	0.74μm	—	0.35	4.2
L&G	0.5μm	0.6	0.65μm	0.34	4.2
L&G	0.35μm	0.45	0.46μm	1.0	4.4
L&G	0.45μm	0.55μm	0.59μm	0.0	4.4

Table 4.1: The values of a_c, a_i , $a(min)$ and $a(max)$ characterising the grain size distributions investigated in this chapter. a_c and a_i apply to the L&G distribution, $a(min)$ and $a(max)$ to the MRN distribution (§3.3.3). No $< a >$ is quoted when the limits of the power-law distributions are close together.

The values of a_c, a_i, $a(min)$, $a(max)$ and $< a >$ which describe these and all other distributions investigated in this section are summarised in Table 4.1.

4.1.3 Larger grains

In view of the poor small-grain fit to the L-band data, suggestions that the dust grains in AGN may be larger than those encountered in the Galactic diffuse ISM and molecular clouds, and the effect that large grains would have on the 3.4μm polarisation, I have also calculated the polarisation that would be produced by grains larger than those used to fit Galactic extinction and polarisation.

I have attempted to find a distribution which would closely reproduce the slope of the L-band polarisation while simultaneously being consistent with the K-band data. This was initially done by generating and inspecting polarisation curves for various single grain sizes, to establish very roughly what size of grains would feature heavily in the distribution. For instance, 0.1μm or 0.8μm grains clearly would not give anything like the correct slope, but 0.55μm grains gave a much better result. Once a radius was chosen, it was treated as the

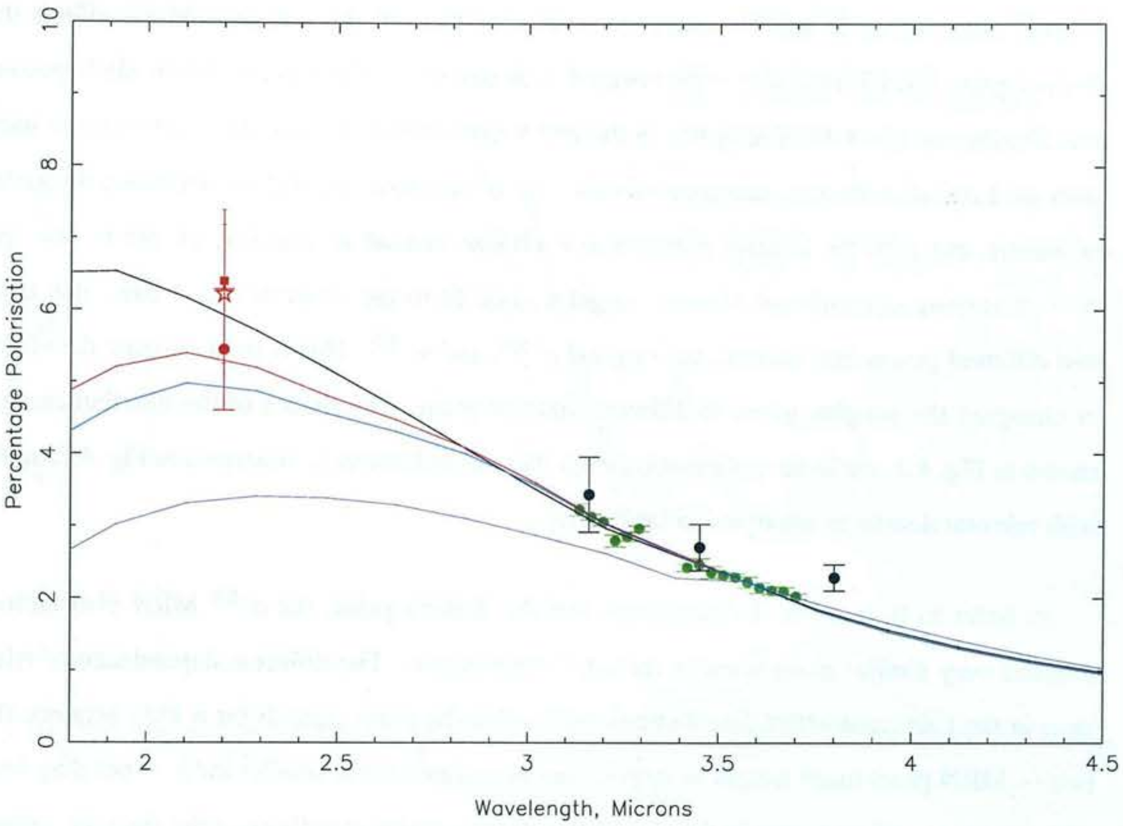

Figure 4.2: Polarisation from size distributions which predict the correct slope through the L-band. Black line — L&G distribution. Red line — MRN distribution, $a^{-3.5}$. Blue line — MRN, $a^{-2.5}$. Also shown is a distribution of larger grains which fails to fit the data (purple line). Observational data and normalisation as for Fig. 4.1.

average-size grain in the distribution (equation 3.30), and the values of a_c and a_i then varied to explore the effects of introducing grains of different sizes.

Fig. 4.2 shows (in black) a L&G distribution of core-mantle grains which gives the observed wavelength dependence of polarisation in the L-band. This distribution is also consistent with the K-band data. It is clear from Table 4.1 that, to fit the L-band data, the minimum and average grain effective radii must be quite large: 0.45 and 0.56μm, respectively. For the 2:2:1 oblate spheroids considered here, these effective radii correspond to axis lengths of 0.57, 0.57 and 0.28μm and 0.73, 0.73 and 0.37μm, as opposed to radii of 0.07 and 0.09μm for the cylinders in the original L&G distribution.

One concern may be that the functional form of the L&G size distribution is not appropriate to the dust in NGC1068, leading to an incorrect estimate of the sizes of the aligned grains. This is quite possible, so to test the extent to which the form of the size distribution affects the derived grain sizes I have also experimented with describing these grains by an MRN power-law distribution (§3.3.3). The grains in the MRN distribution here are the same as those used with the L&G distribution, namely a silicate core of constant size and an increasing thickness of mantle, but with the relative numbers at each size instead specified by an power law. As well as varying $a(min)$ and $a(max)$ to get a good fit to the observations, I have also tried two different power-law indices, the original $a^{-3.5}$, and $a^{-2.5}$. This is to investigate the effect of changing the weights given to different sizes of grain. The shapes of the distributions are shown in Fig. 4.3, while the polarisation from these distributions is illustrated in Fig. 4.2, again with relevant details summarised in table 4.1.

In order to fit both the L-band slope and the K-band point, the $a^{-3.5}$ MRN distribution requires very similar grain sizes to the L&G distribution. The different dependence of $n(a)$ on a in the L&G and MRN distributions means that the grain sizes differ a little between the two — MRN gives more weight to larger sizes so is truncated at smaller radii — but they both still require an enhancement in the size of the aligned grains over those in the Galactic diffuse ISM. The MRN distribution with $a^{-2.5}$ can also fit the slope of the polarisation with the same $a(min)$ and $a(max)$, but the heavier weights given to larger grains in this distribution mean that λ_{max} of the polarisation moves towards slightly longer wavelengths, and P_{max} becomes smaller. This warns against using grains much larger than these — P_{max} will eventually become inconsistent with the observed K-band polarisation. In fact, Fig. 4.2 also shows that, by the time the average grain size in the L&G distribution reaches 0.65μm, not only is the K-band polarisation underestimated, but the slope in the L-band is not at all well matched.

The influence of grain composition is also an issue worth investigating. The curves in Fig. 4.2 were calculated for core-mantle grains, but of course part of the aim of this work is to determine whether the grains do actually take this form in NGC1068. For this reason I have calculated polarisation curves for both pure silicate and wholly-organic grains, with the results shown in Fig. 4.4. Some small differences now start to appear, as illustrated in table 4.1. For the pure silicate grains, the average size of the grains is increased from 0.55 to 0.59μm. The carbonaceous grains require that the population include a slightly smaller component, with a minimum size of about 0.35μm. This is presumably to do with the relative refractive indices of the materials. Greenberg (1978) points out that the polarisation curve is roughly a function

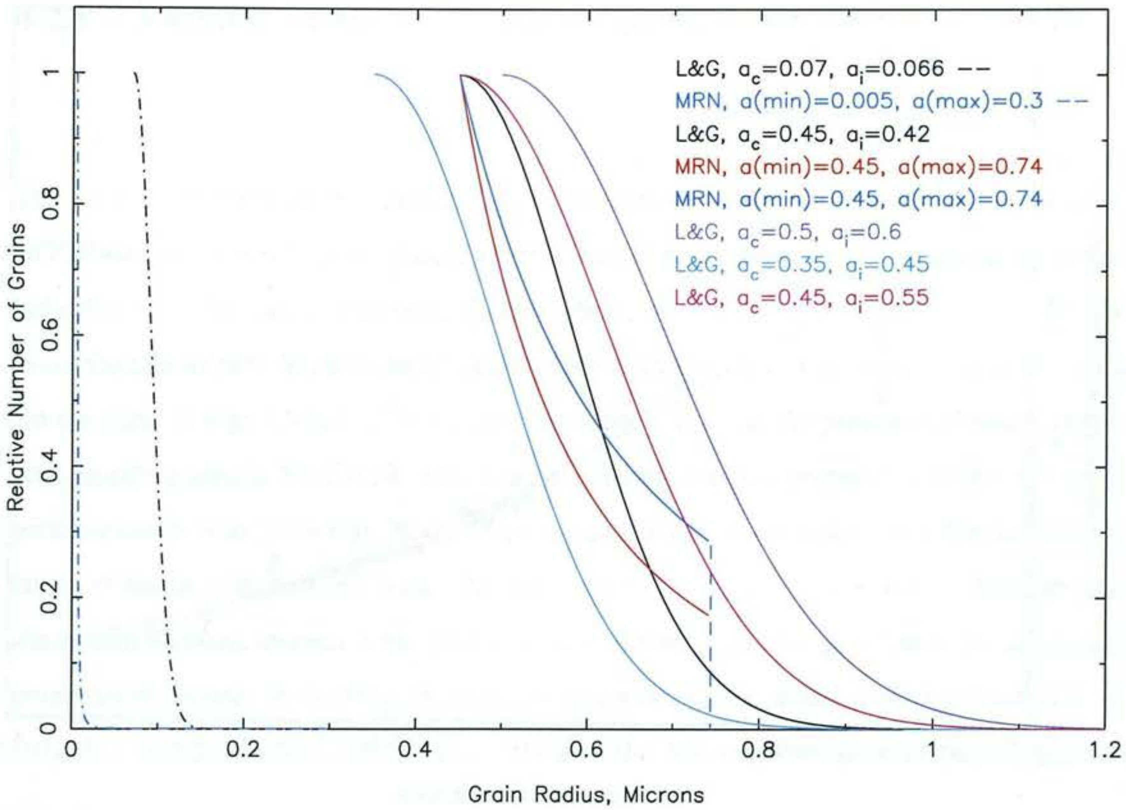

Figure 4.3: N(a) vs a for the distributions I consider in this section.

of $x\,(m-1)$, and therefore that increasing m will mean that smaller grains can achieve higher polarisations at longer wavelengths. This is borne out by the optical constants of the silicate and carbonaceous grain components — the organic material has higher values of n and k in the near-IR and will not need as many large grains to reproduce the observed polarisation. It is clear, though, that the conclusion that "Galactic-size" grains give a poor fit to the observational data will be unaffected by any such changes in the composition of the dust grains.

It is interesting to note that each of the distributions I have examined, with their various compositions and functional forms, predicts different values of P_{max} and λ_{max}. This suggests that if reliable shorter-wavelength data were available, more stringent constraints could be put on the composition and size of the polarising dust in NGC1068. In Chapter 5 I outline observations that might help to constrain the level of dichroic polarisation in the H-band in that galaxy. At the present time, though, what can be said is that to reproduce the K- and particularly L-band polarisation of NGC1068, the aligned grains in that galaxy must be somewhat larger than those observed in the Galactic diffuse ISM. As the L&G size distribution of dust grains with $a_c = 0.45\mu$m and $a_i = 0.42$ is successful at accounting for the gradient of the L-band

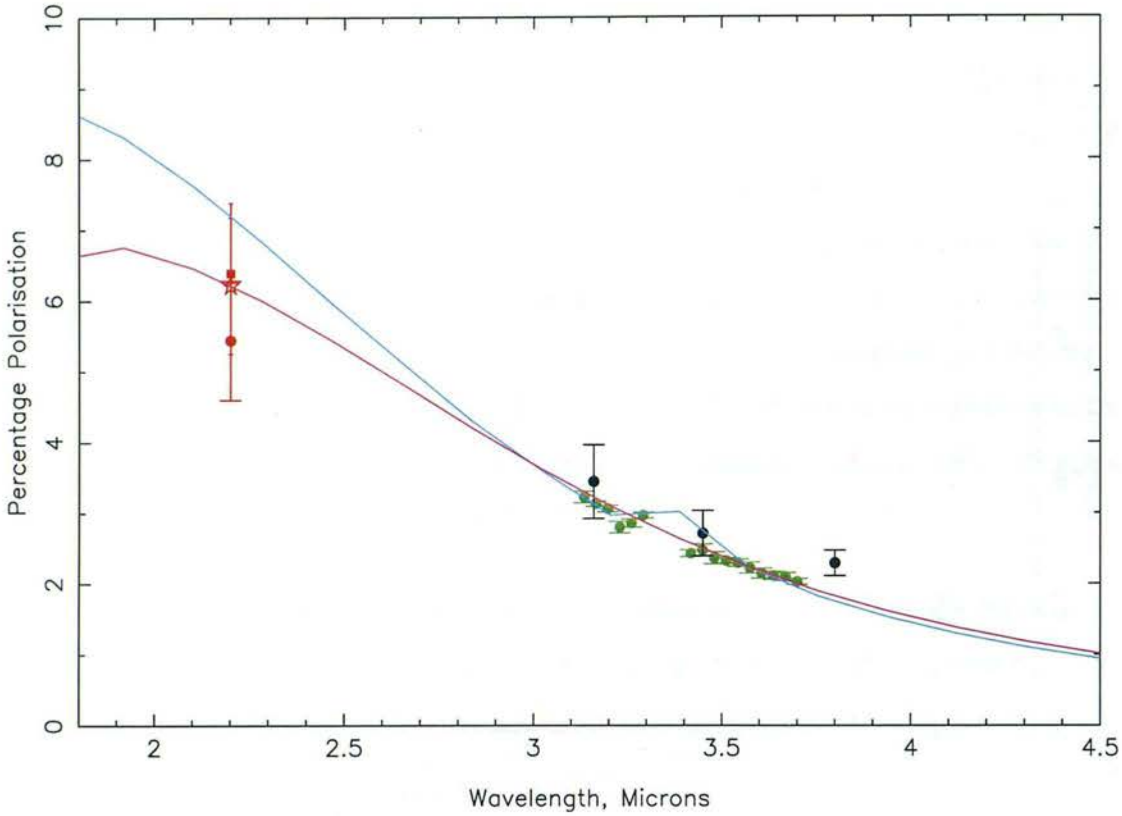

Figure 4.4: Separate silicate and carbonaceous grains. Both compositions require approximately the same size distributions as core-mantle grains to fit the observations.

polarisation of NGC1068, this is the distribution I use in the remaining sections concerning NGC1068, except where otherwise stated.

4.2 The structure of the grains in NGC1068

Although before this work there had been suggestions that dust grains in active galaxies may differ in size from those in our own, nothing has been said about the form the grains may take in other galaxies, whether core-mantle, porous aggregates or something else entirely. In conjunction with our observations of the 3-4μm polarisation and 3.4μm optical depth of NGC1068, the models presented in this thesis allow us finally to probe the actual structure of the aligned grains in that galaxy.

4.2.1 3-4μm polarisation of larger grains

The original objective of this project was to determine whether or not the aligned grains in NGC1068 have a core-mantle structure. This was to be accomplished by measuring the polarisation over the 3.4μm absorption feature where, as I established in Chapter 3, grains like those thought to exist in the Galactic diffuse ISM would cause a large increase in polarisation. On the basis of Figs 3.9 and 3.10, we can immediately rule out the presence of small, aligned core-mantle grains in NGC1068. However, our finding that the grains responsible for the IR polarisation in NGC1068 may be quite large, turns out to have implications for the interpretation of the polarisation spectrum. As discussed in §3.5, large grains have relatively small absorption features, so even if the grains are coated they might not give rise to an appreciable polarisation feature. In order to determine whether or not we should expect a detectable polarisation increase in NGC1068 I have calculated the 3-4μm polarisation of these larger dust grains.

The observed 3-4μm polarisation spectrum of NGC1068 is shown in Fig. 4.5, together with polarisation curves calculated for large grains of three different compositions. These are core-mantle grains in both the L&G and MRN distributions; silicate grains; and grains made wholly of the Li and Greenberg (2002) organic material (see table 4.1). This last was intended to reveal the maximum size of any polarisation increase which could ever be expected from this grain population, in the limit where the grains contain only carbonaceous material.

Immediately evident in both the observed and calculated spectra in Fig. 4.5 is the absence of the pronounced polarisation feature which was clearly visible in Fig. 3.9. A feature is certainly visible in the calculated curves, but at a level which would be barely identifiable above the noise in the unbinned observational data. Binning the data to lower resolution improves matters somewhat. The completely organic grains, with the largest polarisation increase, are not consistent with the data; they would cause an increase in polarisation that should be clearly visible in the data in Fig. 4.5. It is doubtful that such grains make a major contribution to the polarisation in NGC1068. The core-mantle grains also produce polarisation features which lie outside the 1σ error bars shown on the data. The pure silicate grains, on the contrary, provide a very good match to the observations.

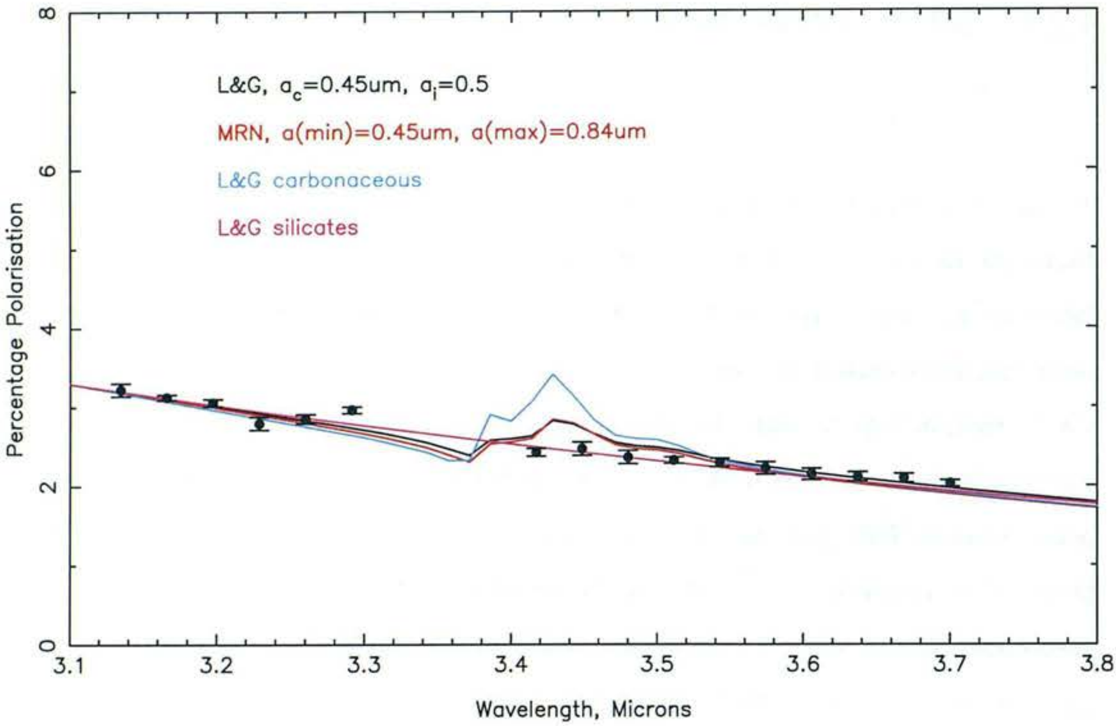

Figure 4.5: The observed and calculated $3 - 4\mu$m polarisation of NGC1068. The observational data have been binned to improve the signal-to-noise ratio.

The core-mantle grains in Fig 4.5 have $f_{carb} = 0.28 - 0.32$, depending on the distribution (L&G or MRN). Clearly, if f_{carb} increases from this fairly low value, the magnitude of the increase in polarisation over the feature will also increase. This effect will be exacerbated by the larger fraction of carbonaceous material, which allows smaller grains to be included in the distribution (§4.1.3). Decreasing f_{carb} would have the opposite effect, and at some point it would become impossible to discriminate between core-mantle and other grain models using these spectropolarimetric data. The discrepancy between the expected and observed polarisations is quite small, but Fig. 4.5 suggests that the aligned dust grains in NGC1068 do not take the form of silicate cores with organic mantles. In the following sections I go on to uncover further evidence in support of this interpretation.

4.2.2 Constraints from column densities

The column densities of dust necessary to cause the observed polarisation and extinction can also provide information about the form of the dust grains in NGC1068. By fitting a suitable continuum to the observed spectrum (as in §2.6) we can quite accurately measure $\tau_{3.4}$, the optical depth in NGC1068's 3.4μm feature, and then equation 3.23 provides the means to calculate the column density of dust which would be required to give that observed $\tau_{3.4}$. Having calculated the polarisation efficiency Q_{pol} of the grains, the column density required to produce the correct degree of polarisation can be found directly from equation 3.24. If the grain model is a good description of the dust, the column densities required to match both the polarisation and $\tau_{3.4}$ will be consistent with each other.

For grains the size of those that may exist in NGC1068, a dust column density of $4.9\times10^{6}\mathrm{cm}^{-2}$ is needed to cause the observed polarisation. To give rise to $\tau_{3.4} = 0.09$, though, $7.7\times10^{7}\mathrm{cm}^{-2}$ is required. At first sight this would suggest that if there were enough core-mantle grains present to produce the observed $\tau_{3.4}$ the polarisation would be much greater than is observed. However, this all depends on the degree to which the grains are aligned. If grain alignment is inefficient in NGC1068 then the degree of polarisation will be reduced; $4.9\times10^{7}\mathrm{cm}^{-2}$ is a lower limit to the number of grains needed to give the observed polarisation. The degree of grain alignment in NGC1068 remains to be seen.

4.2.3 Large grains and the 3.4μm feature

A further piece of evidence against the polarising grains in NGC1068 being coated is in the shape of the 3.4μm absorption band itself. As discussed in §3.5.2, as the size of a particle increases, its absorption bands become progressively more and more distorted. In order to determine whether the observed 3.4μm band in NGC1068 could be caused by mantles on the aligned grains, I have calculated the 3.1 - 3.8μm extinction which would be expected from such a grain population. In a similar manner to the polarisation, the extinction was calculated from equation 3.23 and the dust column density fixed so that the correct value of $\tau_{3.4}$ was obtained. Fig. 4.6 compares the observed and calculated spectra.

The shape of the calculated feature for the larger core-mantle grains bears little resemblance to that of the observed feature — there is a strong absorption minimum around 3.36μm which is not observed in NGC1068. A possibility is that the optical constants used in these models, which were derived for Galactic dust, are not appropriate for NGC1068. However, the

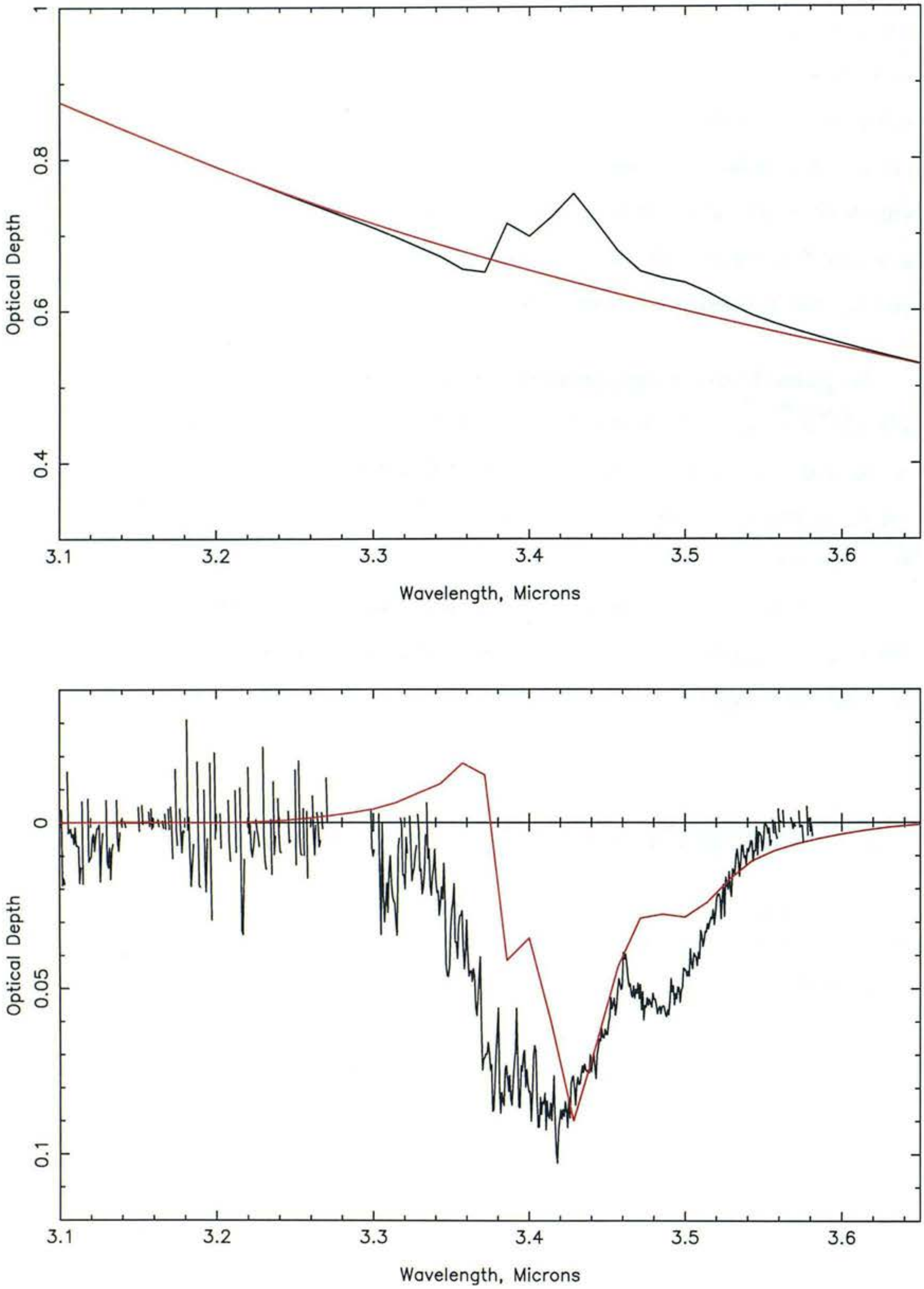

Figure 4.6: Top: 3.1 - 3.8μm optical depth calculated for the large L&G distribution of core-mantle grains which fit the IR polarisation in NGC1068. The column density of grains is chosen so that the derived $\tau_{3.4}$ matches the observed value. The red curve is a spline fit to the continuum extinction from 3.1-3.2 and 3.7-3.8μm. Bottom: observed and calculated optical depth in the 3.4μm feature. The calculated spectrum (red line) is found by taking the difference between the calculated extinction and the continuum fit.

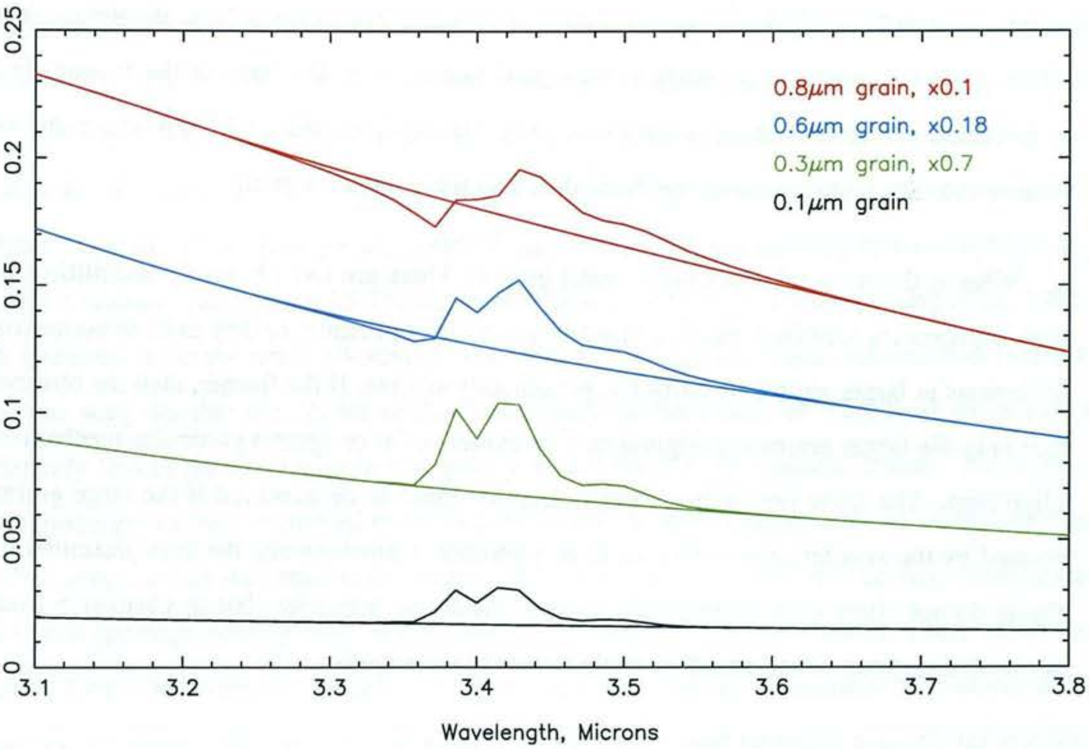

Figure 4.7: Extinction efficiencies and continuum fits for various sizes of core-mantle grains. These grains are all 2:1 oblate spheroids with $f_{carb} = 0.5$.

similarity of the general shape of the feature in NGC1068 to that observed in many Galactic lines of sight indicates that the composition of the carbonaceous material is very similar to that in Galactic dust (§4.3.2). This implies that the odd shape of the calculated feature is not due to the optical constants and rather to the size of the grains.

To further illustrate this point, Fig. 4.7 shows extinction calculated for some single particle sizes. When the grain radius is 0.1μm, its feature appears very much like that of a small particle, showing none of the asymmetry associated with larger particles. By the time the grain's effective radius reaches 0.6μm, however, approximately the average size of the aligned grains in the large L&G distribution, a minimum begins to appear in the extinction at the short-wavelength edge of the feature, something which is not observed in NGC1068. The feature produced by the 0.8μm grain, of which there are a few in the large L&G distribution, is altogether wrong. Large grains produce a 3.4μm feature which does not resemble that observed in NGC1068.

We can conclude from this observation that the aligned grains which give rise to the IR polarisation in NGC1068 are *not* the same grains which create the 3.4μm absorption feature. These grains cannot have a mantle of any great thickness or the shape of the feature (in both polarisation and in extinction) would be visibly altered. The grains which produce the 3.4μm feature must be predominantly much smaller than the polarising grains.

What is the form taken by these small grains? There are two obvious possibilities: either they are some form of free, small, nonpolarising grain population, or they exist as nonpolarising inclusions in larger aggregate particles, presumably silicate. If the former, then the observation that only the larger grains are aligned may be evidence for or against particular mechanisms of alignment. The latter possibility, though, may be more to be expected if the large grains are formed by the smaller grains sticking to one another. Unfortunately, the data presented in this thesis do not allow us to distinguish between these two scenarios, but in Chapter 5 I outline some observations which could be made to clarify the situation.

4.3 Aliphatic hydrocarbons in NGC1068

Beyond the size and structure of the dust grains, the 3.4μm feature allows direct comparisons to be made between the hydrocarbon-containing dust in NGC1068, our Galaxy, and other extragalactic environments.

4.3.1 The contribution of the carrier of the 3.4μm band to the extinction

The ratio $A_V/\tau_{3.4}$ can be used to probe the contribution of the carrier of the 3.4μm band to the total visual extinction in a line of sight. In local Galactic lines of sight, determinations of $A_V/\tau_{3.4}$ range from $\sim$ 250 (Pendleton et al., 1994; Sandford et al., 1995) to $\sim$ 340 (Rawlings et al., 2003). This is much higher than towards the Galactic centre, where $A_V/\tau_{3.4} \sim$ 150 (Pendleton et al., 1994; Sandford et al., 1995), indicating that hydrocarbons make a relatively larger contribution to extinction in the Galactic centre than locally. For the hydrocarbons in the dust in NGC1068 to be as important to the extinction in the nucleus of that galaxy as they are in the Galactic centre would require $A_V = (0.09\times \sim 150) \sim 13.5$. To achieve $A_V/\tau_{3.4} \sim 250$, on the other hand, would necessitate $A_V \sim 23$, and $A_V/\tau_{3.4} \sim 340$, A_V ~31mag. The extinction towards the hot dust thought to be the source of NGC1068's infrared flux has been calculated by a number of groups using various means (Bailey et al., 1988; Efstathiou et al., 1995; Young et al., 1995; Rouan et al., 1998, discounting figures based on $\tau_{3.4}$ itself). Estimates range from 15-25mag (Bailey et al., 1988) to ~ 45mag (Young et al., 1995), but a number lie in the range 20-30mag. The values of A_V are uncertain and model-dependent, but this suggests that the carrier of the 3.4μm band in the centre of NGC1068 gives rise to relatively less of the extinction in that galaxy than it does in the Galactic centre. The carbon-containing grains behave instead more like the dust in the solar neighbourhood. Adamson et al. (1990) propose that this reflects the degree of hydrogenation of the band carrier. Unsaturated materials (perhaps bearing some resemblance to graphite with a few H atoms attached) absorb visible light effectively, but absorb only poorly at 3.4μm, but as the number of H atoms in the material increases, this situation gradually reverses. This could naturally account for differing $A_V/\tau_{3.4}$ ratios in different environments.

4.3.2 Comparisons with the 3.4μm band in other environments

As mentioned in §1.4, the profile of the 3.4μm band contains much information on the nature of the carbonaceous material in the dust. Figs. 4.8 and 4.9 compare the feature in NGC1068 to the Galactic sources, GCIRS 6E, GCIRS 7 and CRL618, and to the ultraluminous galaxy, IRAS 08572+3915[1]. GCIRS 7 is a Galactic centre M1I supergiant lying behind about 37 mag of extinction (Rieke et al., 1989), with its 3.4μm band arising in the diffuse ISM component of this (McFadzean et al., 1989; Sandford et al., 1991). GCIRS 6E is one of two sources making up the Galactic centre object, GCIRS 6, and is now known to be a Wolf-Rayet star (Krabbe et al., 1995). As with GCIRS 7, the 3.4μm feature is thought to come from the diffuse medium between us and GCIRS 6E. The 3.4μm band in CRL618, on the other hand, is thought to be produced in the outflow of this carbon-rich evolved star (Chiar et al., 1998). At a redshift of 0.058, IRAS 08572 exhibits an extremely strong 9.7μm silicate absorption, as well as the deepest 3.4μm feature yet observed (Wright et al., 1996; Dudley and Wynn-Williams, 1997).

---

[1] Thanks to Yvonne Pendleton and Jean Chiar for providing the spectra used in these figures

Dudley and Wynn-Williams (1997) find that the major power source in IRAS 08572 is a deeply obscured AGN, which could mean that its 3.4μm feature arises, like NGC1068's, in dust close to the active nucleus. However, unlike NGC1068, which is clearly a face-on spiral galaxy, optical and infrared images of IRAS 08572 show that its morphology is unclear (Scoville et al., 2000; Soifer et al., 2000). As well as this, the appreciable distance of IRAS 08572 means that the aperture used to measure the 3.4μm band covers more of the galaxy than just the nuclear regions. Therefore it is quite likely that the 3.4μm band in that galaxy is caused by a combination of both diffuse-medium-like and circumnuclear dust.

Probably the most striking aspect of Figs 4.8 and 4.9 is the close resemblance that the 3.4μm feature in NGC1068 bears to that observed in all of the other objects presented here. The 3.4μm absorption in NGC1068 clearly exhibits the same subpeaks as are observed in the feature elsewhere: the 3.38μm -CH_3 asymmetric stretch, 3.42μm -CH_2- asymmetric stretch and 3.48μm -CH_3 symmetric stretch. As in the other spectra, the 3.50μm -CH_2- symmetric stretch band is not clearly present, an observation interpreted by Sandford et al. (1991) as signalling the presence of electron-withdrawing groups attached to the hydrocarbon chains which give rise to the feature. Not only are the peak wavelengths good matches, but the relative strengths of the subfeatures are also very similar between NGC1068 and the other objects. This indicates that the relative numbers of -CH_3 and -CH_2- groups, and therefore the average lengths of the hydrocarbon chains, are very similar in all the lines of sight. It is also conceivable that the band strengths of the carbonaceous material have changed along with the relative numbers of -CH_3 and -CH_2- groups, in such a way that the overall feature shape remains the same, but this seems like a much less plausible explanation. The carriers of the 3.4μm band in NGC1068 and in other, diverse, environments look chemically very similar.

One possible explanation for the similarity of the 3.4μm feature in different environments could be simply that the spectra of many different hydrocarbon-containing substances might average out to the observed spectrum. This is undoubtedly true to a certain extent, as it would be naïve to expect that every dust grain would contain the exact same chemical moieties. It seems less plausible, though, that systematic differences between the carrier of the 3.4μm band in different environments could be masked in this way. If, say, newly-formed dust contained a higher fraction of longer hydrocarbon chains than old, processed dust, this would be expected to show up as an enhancement in the subpeaks corresponding to -CH_2- groups. Laboratory

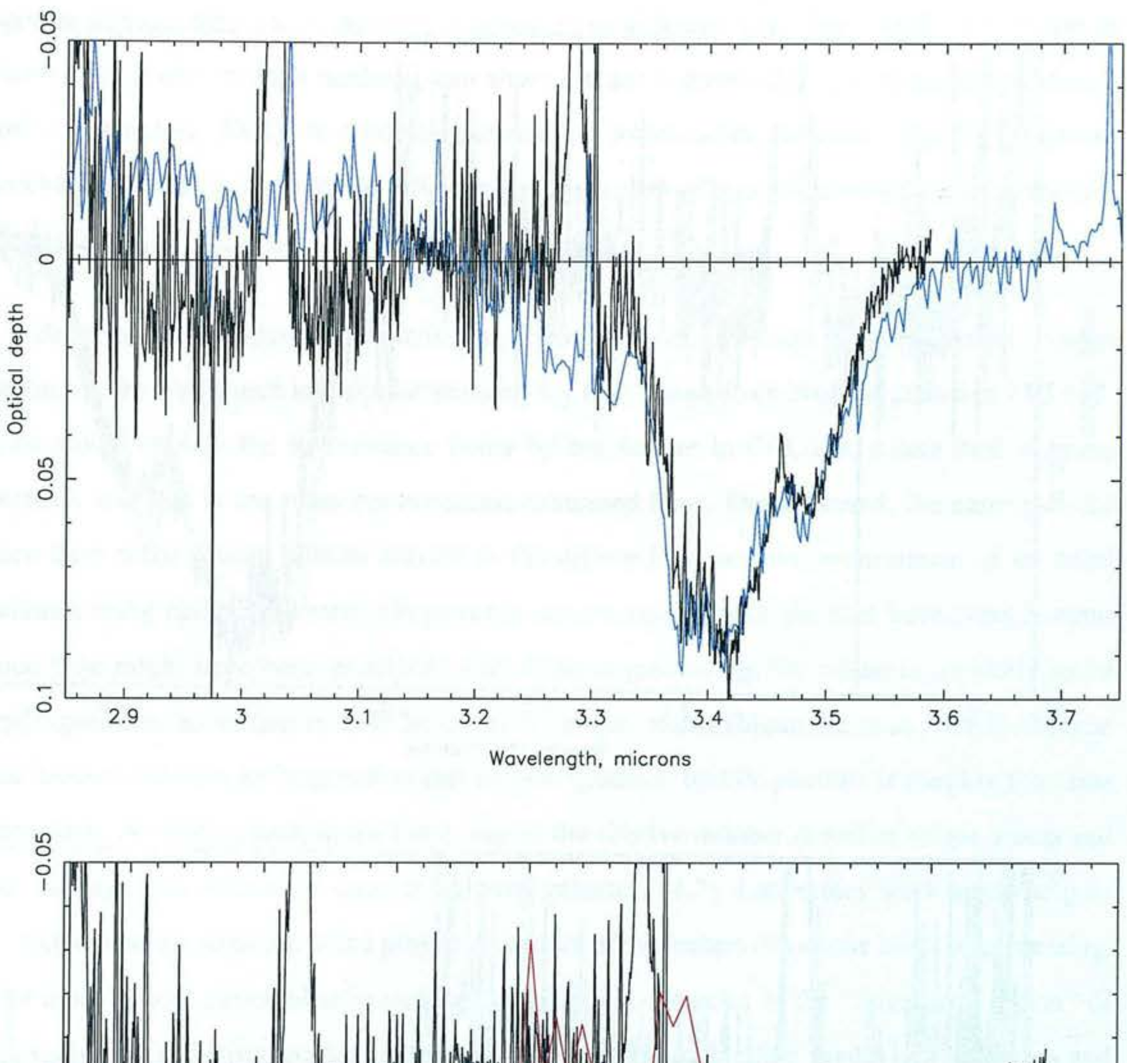

Figure 4.8: Upper panel: The 3.4μm feature in NGC1068 (black), compared with that observed towards GCIRS 6E (Chiar et al., 2002, blue). Lower panel: NGC1068's 3.4μm feature compared with GCIRS 7 (Sandford et al., 1995, red - lower resolution; blue - higher resolution). The spectra have been multiplied by a constant in order to have the same peak optical depth as NGC1068.

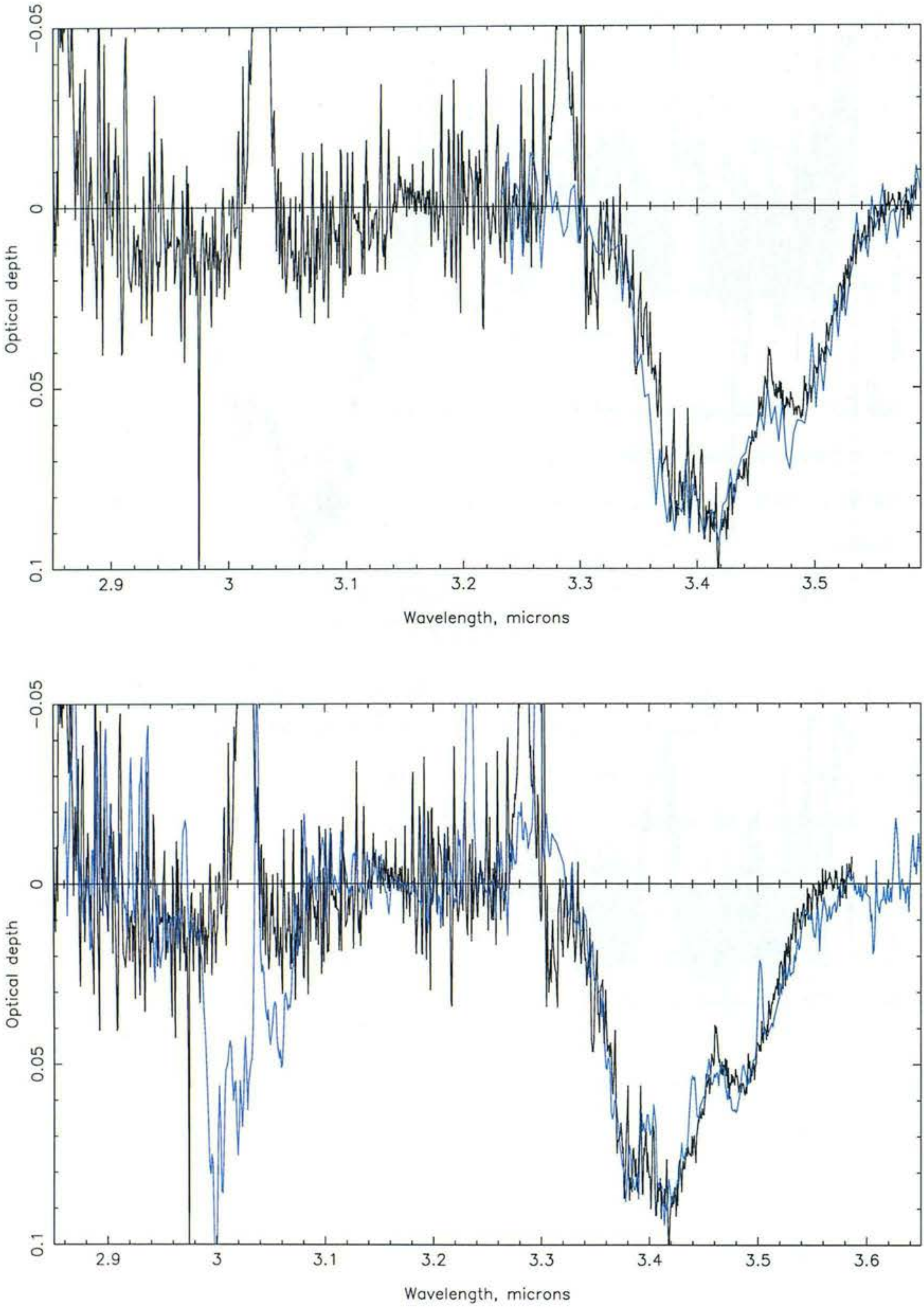

Figure 4.9: Upper panel: The 3.4μm feature in NGC1068 (black) compared with that observed in the ultraluminous IR galaxy, IRAS 08572+3915 (Wright et al., 1996, blue). Lower panel: CRL618's 3.4μm feature (Chiar et al., 1998, blue).The spectra have been multiplied by a constant so that they have the same peak optical depth as NGC1068.

spectra support this view — substances produced in different ways, from irradiation of ices to electric discharge through methane, can show distinctly different 3.4μm features (Pendleton and Allamandola, 2002). It would be surprising if hydrocarbon material formed by different mechanisms and/or subjected to different environmental effects did not also exhibit such differences.

Perhaps a more plausible scenario, then, would be one in which the carrier of the 3.4μm feature is always formed in a similar manner, say in outflows from evolved stars like CRL618. This would explain the resemblance borne by the feature in CRL618, where dust is being formed, and that in the other environments examined here. Once formed, the carrier would then have to be robust, able to survive in the diffuse ISM and the environment of an AGN without being radically altered. Or, possibly the environments of the dust have more in common than might have been expected. One form of processing, for example, is likely to be hydrogenation, saturation of C-H bonds by hydrogen atoms (Mennella et al., 2002). Maybe the balance between hydrogenation and dehydrogenation by UV photons is roughly the same regardless of environment, in the same way as the relative number densities of gas atoms and cosmic rays may remain the same in starburst galaxies (§1.3). Laboratory work might help us to understand the response of the proposed carriers of the feature to various kinds of processing. The most helpful pieces of information, though, will be spectra of the "fingerprint region" of the spectrum, at 5-9μm, containing bands corresponding to bending modes of C-H bonds and to modes of the carbon skeleton, together strong discriminators between materials of different composition and origin.

Some differences are apparent in the spectra, however. Definitely *not* apparent in the spectrum of NGC1068 is the prominent absorption band centred at 3.0μm, visible in CRL618. This band has been identified by Chiar et al. (1998) as being a blend of HCN and C_2H_2 rovibrational lines in the outflow from this AGB star. Acetylene is an important constituent of models describing dust formation in circumstellar envelopes (e.g. Frenklach and Feigelson, 1989; Schnaiter et al., 1999), and indeed Goto et al. (2003) have recently observed that HCN and C_2H_2 are only evident in the very central regions of the proto-planetary nebula, IRAS 22272+5435, suggesting that these molecules are rapidly incorporated into the nascent dust grains. An intriguing suggestion put forward by Elvis et al. (2002) is that dust could be formed in outflows from quasars, and if that is the case, the same process might also be expected to be apparent in Seyfert galaxies. The absence of the HCN and C_2H_2 absorptions in NGC1068, though, implies that ongoing dust formation is not occurring in the nucleus of this nearby Seyfert galaxy, at least.

An interesting aspect of the spectrum of GCIRS 6E in Fig.4.8 is an absorption on the wing of the 3.4μm band, at around 3.3μm. The wavelength of the band is about that of a C-H bond stretch where the carbon atom forms a double bond to another atom, possibly as part of an aromatic ring. However, the band appears much wider than typical PAH bands (100cm^{-1} vs $\sim$ 30cm^{-1}), so its identification remains uncertain (Chiar et al., 2002). Although not apparent in the spectra of the other objects, Chiar et al. (2002) note that the continua used to derive the optical depths would have removed the 3.3μm absorption. Could this be the case with our CGS4 and UIST spectra of NGC1068? Unfortunately this is very difficult to check. The instrumental hydrocarbon absorption in the CGS4 spectrum mean that this region of the spectrum cannot be seen, and the hydrogen emission lines arising in the standard star obscure this region in the UIST spectrum. The spectrum of Marco and Brooks (2003) is no help; they do not specify the shape of the continuum fit to their data. The presence or absence of this unidentified feature in NGC1068 remains unproven.

4.4 Silicates in NGC1068

The primary aim of obtaining an N-band spectrum of the nucleus of NGC1068 was to relate the polarisation across the feature to its optical depth, and thereby estimate the degree of polarisation to be expected over the 3.4μm absorption feature. Although the N-band spectropolarimetry was not successful, the flux spectrum we have measured still represents a considerable improvement on the data in the literature (Roche et al., 1984; Tomono et al., 2001). In this section I suggest ways in which this spectrum may be used to investigate the nature of the silicate dust in NGC1068.

Absorption spectra of diffuse cloud silicates differ somewhat from those of molecular cloud silicates. Bowey et al. (1998) attempted to fit silicate spectra of dense and diffuse clouds with the emissivities of silicates in the Trapezium molecular cloud and circumstellar silicates in

μ Cephei. Whereas spectra sampling dense cloud lines of sight were better fit by the Trapezium emissivity, silicates in the diffuse ISM were noticeably better fit by μ Cephei. The difference between the two types of spectra is essentially that the molecular cloud grains produce excess absorption in the long-wavelength wing of the band, relative to the diffuse cloud grains; diffuse ISM/circumstellar silicates tend to have narrower features than dense cloud silicates. The interpretation of this difference in width is unclear, but Bowey et al. (1998) cite grain size, mantling and silicate composition as possible factors. These factors have also been found to affect the peak wavelength of the silicate feature in laboratory silicates (Bowey et al., 1998, and references therein).

On the basis of their classification of the emission spectra of AGB and red supergiant stars, Speck et al. (2000) propose an evolutionary sequence for circumstellar silicates. In both types of object, several classes of broad feature are seen, and one "classical" silicate feature. The broad features differ between the AGB stars and the supergiants, but the narrower, classical silicate features are always very similar. Speck et al. (2000) suggest that the dust in these environments undergoes different evolution and processing, but ultimately acquires approximately the same composition.

It should in principle be possible, then, to compare the 10μm spectrum of NGC1068 with those presented in the above studies, in order to investigate where in the evolutionary sequence of Speck et al. (2000) the dust might lie, or whether it bears more resemblance to Galactic diffuse, dense or circumstellar dust. On first inspection, the FWHM of NGC1068's silicate feature (approximately 2.0-2.4μm depending on whether a first- or second-order continuum is used) seems to be closer to that measured by Bowey et al. (1998) for diffuse ISM grains than to dense cloud grains. The shape and peak wavelength, too, may be more like Speck et al.'s classical silicates than their purportedly newly-formed dust. However, the reliability of the conclusions drawn from these comparisons will depend very much on the continuum used to extract the optical depth spectrum, and the degree to which the telluric O_3 feature can be cancelled. Before proceeding, it would be sensible to attempt to derive the continuum under the feature in a manner consistent with that of Bowey et al. (1998) and Speck et al. (2000). It would also be possible to experiment with the spectra of NGC1068 and the standard star to optimise the cancellation of the ozone feature (as a close inspection of the profile of the silicate feature was not the main objective of this programme, this was not attempted during the data reduction presented here). Then — and bearing in mind that the silicate feature in NGC1068 may be a mixture of absorption and emission — it may be possible to perform the first detailed comparison of the 9.7μm silicate feature in another galaxy with those observed in our own.

4.5 GCIRS 7 revisited

In Chapter 3 I established that grains like those thought to exist in the Galactic diffuse ISM are capable of causing a distinctive rise in polarisation over the 3.4μm C-H bond stretch. This conclusion depends only on the continuum polarisation around the feature and on the assumed properties of the dust in the line of sight. It does not require any knowledge of the behaviour of the polarisation over the 9.7μm Si-O bond stretch, something which has hampered previous observational studies of the core-mantle dust model. This suggests that in the case of GCIRS 7, where the continuum polarisation has been well determined and a firm upper limit placed on any rise in polarisation over the 3.4μm feature, the techniques developed in this thesis could be applied to good effect.

In principle, calculating polarisation curves for GCIRS 7 should be a straightforward case of using the grain parameters discussed in Ch. 3, with a size distribution appropriate for Galactic diffuse dust. There are, however, one or two complications. Firstly, about 20 of the 34 or so magnitudes of extinction towards GCIRS 7 arises in diffuse clouds, but the presence of ice features in the spectrum of the Galactic Centre suggest that ~ 10 mag may come from dense cloud dust (Henry et al., 1984; McFadzean et al., 1989; Whittet et al., 1997). Dust in dense molecular clouds differs from diffuse cloud dust in several respects: it is thought to contain fewer small grains (§4.1), is coated in ices, and, most seriously, can be polarising but appears not to contain the carrier of the 3.4μm feature (Allamandola et al., 1992).

Secondly, GCIRS 7 is suspected of possessing circumstellar material which causes polarisation by scattering (Bailey et al., 1984). The presence of this material is inferred from the magnitude and wavelength dependence of the infrared polarisation, which differ from other Galactic centre sources. By determining the interstellar polarisation towards the Galactic centre from sources which have unremarkable polarisation characteristics, Bailey et al. (1984)

were able to establish the contribution of GCIRS 7's intrinsic component in the J, H and K bands. However, no observations were made at longer wavelengths, and (as mentioned in §4.1) the form taken by the interstellar polarisation past the K band is uncertain. This means that it is difficult to reliably determine the how much of the polarisation towards GCIRS 7 arises in the circumstellar shell.

Fortunately, these problems are surmountable. The presence of 3.4μm absorption indicates that there is diffuse dust in the line of sight. As described in Ch. 3, L&G have constructed a population of core-mantle grains which quite well reproduces the observed diffuse ISM IR polarisation, and I have used their results to calculate in detail the polarisation that grains like these would cause over the 3.4μm feature. Fig. 3.9 shows that the dust may be expected to give rise to approximately a doubling in polarisation over the feature. This seems large, given that A99 estimated an increase of only 0.4% (about 30%) over the feature in GCIRS 7, but an independent estimate gives the same figure. D&L calculate that spheroids of their astronomical silicate would give approximately 15 times as much polarisation in the 9.7μm silicate feature as in the continuum at 5μm. Li & Greenberg (2002) confirm that $(\Delta p/\tau)_{3.4} \approx (\Delta p/\tau)_{9.7}$, and observations show that the strengths of the 3.4 and 9.7μm bands are correlated, with $\tau_{3.4}/\tau_{9.7} \approx 1/18$ in the Galactic diffuse ISM (Sandford et al., 1995). This also implies approximately a twofold increase in polarisation over the 3.4μm feature.

This being the case, if all of the 1.5% polarisation towards GCIRS 7 arose in the diffuse ISM, we could expect to observe polarisation of about 3% in the feature. In fact, A99 were able to place an upper limit on the 3.4μm polarisation of only 0.08% above the continuum. If the grains in the diffuse ISM are mantled, then only about one thirtieth of the polarisation, 0.05%, can come from grains in the diffuse ISM. The same analysis can be applied to the spectropolarimetry of Ishii et al. (2002), who find that the luminous embedded YSO, IRAS 18511+0146, is about 1.5% polarised with an increase of no more than about 0.1% across its 3.4μm band.

This could suggest that either the core-mantle grains are spherical or that the grain alignment mechanism fails almost completely in both of these lines of sight. As far as GCIRS 7, at least, is concerned, this seems a little unlikely. Magnetic alignment is thought to be strong across the Galactic centre (Aitken et al., 1998), and plenty of other Galactic centre sources are polarised by dust (e.g. Aitken et al., 1986), so this would have to be a very local effect. The other obvious possibility is that core-mantle grains do not in fact exist in this line of sight. Observations of the polarisation of the silicate absorption feature in GCIRS 7 and the C–H absorption in GCIRS 3 (which is known to have excess silicate polarisation) will help to clarify matters, and we intend to carry out these measurements later this year. Another, ideal, candidate for polarisation measurements would be the line of sight towards Cyg OB2 #12, which is thought to intersect neither a circumstellar shell nor molecular cloud dust (Whittet et al., 1997). There, the polarisation over the silicate and organic dust absorption features will be a severe test of the core-mantle dust model. Precise observations of the polarisation of this source will be feasible when, for example, Gpol becomes available on Gemini North.

CHAPTER 5

Conclusions

For some years now, various authors have suggested that dust grains in AGN may differ from those in more familiar Galactic environments. Studies of the extinction, colours and emission properties of such galaxies have hinted that their dust grains grow to be larger than those in most parts of the Galaxy (Laor and Draine, 1993; Imanishi, 2001; Maiolino et al., 2001a,b). On the other hand, some of this evidence has been disputed (Weingartner and Murray, 2002), and other studies have suggested a preponderance of small grains (Crenshaw et al., 2001). Given that dust is such an important constituent of galaxies at all redshifts, a resolution to this problem has been overdue.

In this thesis I have presented new evidence that the polarising dust grains surrounding the nucleus of an active galaxy are indeed somewhat larger than the dust grains in either the Galactic diffuse ISM or in molecular clouds. In fact, a good fit to the observational data can be achieved if the average effective radius of the aligned grains in NGC1068 is approximately 0.6μm. To put this in perspective, diffuse cloud dust is characterised by grains which are predominantly $\lesssim 0.1\mu$m in size (Mathis et al., 1977; Li and Greenberg, 1997).

Although the dust grains in NGC1068 may be different in size from those in the Galactic diffuse ISM, the spectrum of the 3.4μm feature presented in Chapter 4 suggests that one grain component, at least, is chemically very like its Galactic counterpart. In fact, the carrier of the 3.4μm band appears uncannily similar in several, very different, environments. The reason for this is not yet clear, but I speculate that it could suggest that the formation mechanism of the band carrier varies little, and that the carrier is robust enough to remain almost unchanged when subjected to many different environmental influences. Alternatively, the environments in which the dust exists may be more similar than we have previously suspected.

A longer-running debate also exists over the form taken by interstellar dust grains, whether in our own galaxy or in others. In this thesis I have followed up some work designed to test whether grains take the form of silicate cores with carbonaceous mantles, a model which has gained widespread support. I conclude that the grains in the nucleus of NGC1068 are *not* coated silicates — the first time extragalactic grains have been scrutinised in such detail. In addition, my calculations show that the dust in the line of sight towards the Galactic centre source, GCIRS 7 can only be coated if it somehow produces virtually no polarisation signature at all.

In this chapter I speculate about possible causes of an increase in grain size in NGC1068 and briefly discuss the practical ramifications of the presence of large grains. I also suggest some further work which would help clarify the nature of the nonpolarising dust grains in NGC1068, and of the dust in active galaxies in general.

5.1 Grain growth in NGC1068

The density of the circumnuclear material in NGC1068 is thought to be high, and dense environments are known to encourage coagulation of dust grains. For instance, in novae ejecta, where the number density of ejecta can reach $5 \times 10^{11}\,\mathrm{cm}^{-3}$, dust grains are observed to reach sizes of a few tenths of a micron on timescales of just a few months (Shore et al., 1994; Rawlings, 1998). This in itself may be enough to bias the grain size distribution in an active galaxy towards larger sizes. The dust in NGC1068 is not just dense, though — it is warm, too. At first sight this may seem likely to make grain growth less probable, by increasing the speeds at which the grains collide. Above a certain critical velocity, colliding grains will tend to bounce apart or shatter rather than coalesce (Chokshi et al., 1993). However, some recent work by Kouchi et al. (2002) shows that the situation can be rather different when the carbonaceous fraction of dust grains is taken into account. In experiments involving various analogues of interstellar organic material, they found that the sticking probability of two grains actually increased as the temperature was increased, reaching a maximum at about 250K. This is because, as the temperature is raised, the organic material begins to behave less like a solid and more like a very thick, viscous liquid, able to dissipate kinetic energy on collision. Kouchi et al. (2002) used this finding to explain the rapid growth of asteroids in the early solar system; it does not seen unreasonable to expect that a similar mechanism may be in operation in the dust in NGC1068.

5.2 Suggestions for future work

Whatever the catalyst for the formation of large grains in NGC1068, their likely presence shows that the dust in this AGN is responding to the nature of the environment in which it exists. If NGC1068 is typical of active galaxies, this could have implications for our understanding of galaxies in general.

5.2.1 Large grains, small grains and the extinction curve

Although I have shown that grains the size of those in the Galactic ISM do not produce a satisfactory fit to the polarimetric data on NGC1068, the lack of useful data at wavelengths shorter than the K-band limits the constraints that can be placed on the sizes of the grains. However, there may exist a solution to part of this problem. In the H-band, there are two major uncertainties - the dilution by unpolarised starlight, and the fractions of the polarised flux contributed by scattering and dichroism. As shown by Lumsden et al. (1999), scattering becomes less significant in smaller apertures. Therefore, if H-band imaging polarimetry was performed using decreasing aperture sizes, a trend towards increasing polarisation would enable a lower limit to be placed on the polarisation caused by dichroism. Conversely, decreasing polarisation in smaller apertures would help set an upper limit. Of course, the stellar dilution also becomes less significant in smaller apertures, but the aperture-dependent values of Thatte et al. (1997) could be used to quantify and remove this effect. Given the uncertainties in the calculation of the nonstellar fraction, this technique may not give unambiguous results, but NGC1068 is a bright source and observing time requirements would be small enough for the attempt to be worthwhile.

As discussed in §1.2, the interstellar extinction curve reflects the size distribution of dust grains in the ISM. It is well known that a flatter extinction curve is observed in dense molecular clouds, where $R_V = A_V/E_{B-V}$, the ratio of total to selective visual extinction, moves to higher values. I have calculated extinction coefficients for some fairly large grains, and Fig. 5.1 shows that for dust grains of this size, the extinction curve can be very flat. This is potentially an important effect for any study that assumes a form for extinction in AGN. For example, Marco and Alloin (2000) find observationally that $L - M = 1.6 \pm 0.4$ for NGC1068, corresponding to a dust temperature of 480K. Correcting for extinction, they determine an intrinsic colour of $L - M = 0.8 \pm 0.4$, or a dust temperature of 700K. The derived $L - M$ colour, and therefore dust temperature, depend on the wavelength dependence used for the dust extinction.

Clearly it would be very helpful to know the form taken by the extinction in AGN, but the extinction curve shown in Fig. 5.1 may not be a good representation of the actual extinction in NGC1068. For simplicity, it is based on spherical silicate particles, where the real grains are aspherical and may contain material other than silicates (this is why the curve for NGC1068 does not show the prominent bump seen in the others). More seriously, the polarimetric techniques I have used to probe dust grain sizes in this work are sensitive only to aligned grains, and it is quite possible that an additional population of smaller, nonpolarising grains exists alongside these larger grains (§4.2.3). If that is the case, their presence will alter the shape of the extinction curve. Rather than attempting to calculate the wavelength dependence of extinction, it may instead be possible to take advantage of the intrinsic nuclear spectrum of NGC1068 presented by Pier et al. (1994). Using small-aperture polarimetric data they were able to observe the nuclear continuum in scattered light, free from host galaxy contamination and dust absorption. The "true" extinction curve in NGC1068 could then be derived from the difference between the intrinsic spectrum and the observed spectrum, and comparison between this curve and that presented in Fig. 5.1 would confirm the presence or absence of an additional small grain population in NGC1068.

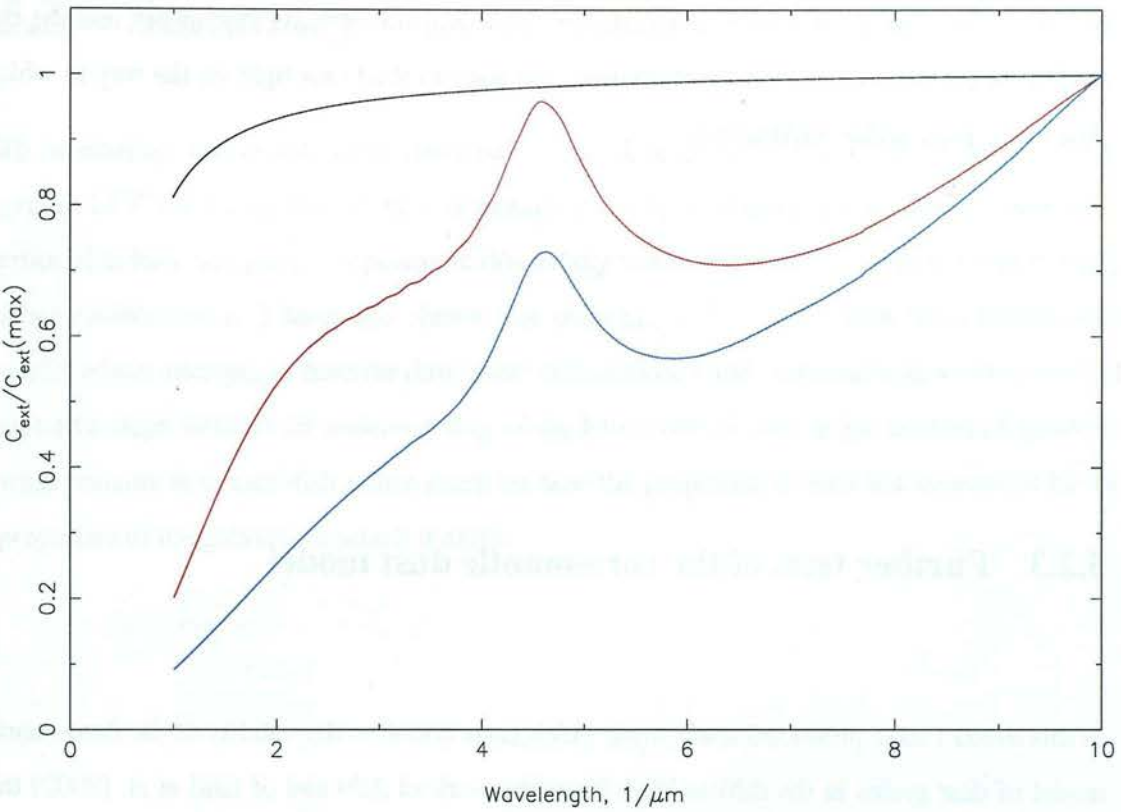

Figure 5.1: Comparison of extinction cross-sections calculated for grains in different environments. Blue curve: $R_V = 3.1$, representative of the Galactic diffuse ISM (Draine and Weingartner, 2001). Red curve: $R_V = 5.5$, appropriate for e.g. θ^1 Ori C in the Orion nebula (Mathis and Wallenhorst, 1981; Draine and Weingartner, 2001). Black curve: extinction for an $a^{-3.5}$ distribution of silicate spheres with $a(min) = 0.45\mu$m and $a(max) = 1.0\mu$m, calculated using the BHMIE programme (Bohren and Huffman, 1983). To approximate the large grain population in NGC1068.

5.2.2 The 3.4μm band in other galaxies

In Chapter 4 I presented observations showing that the carrier of the 3.4μm band in NGC1068 is chemically very similar to that observed in many other environments. The profile of the 3.4μm feature in familiar laboratory chemicals is very variable, as are the profiles of some of the materials which have been suggested as analogues of the carbonaceous dust — Fig. 7 of Sandford et al. (1991) clearly illustrates this point, see also Alpert et al. (1973) — so it seems remarkable that interstellar dust would be so uniform. To further investigate the carbonaceous dust in a range of extragalactic environments, and in particular to search for correlations between dust and galaxy properties, my collaborators and I have embarked on a survey of the 3.4μm dust absorption in Seyfert II galaxies. By illuminating correlations, or a lack of them, between galaxy properties such as metallicity, dust temperatures and luminosity and the behaviour of the carbonaceous dust component, we hope to shed new light on the way in which dust reacts to its wider environment.

5.2.3 Further tests of the core-mantle dust model

In this thesis I have presented some work which casts doubt on the validity of the core-mantle model of dust grains in the diffuse ISM. From the work of A99 and of Ishii et al. (2002) this was already suspected — though controversial — in the case of dust in two Galactic lines of sight. As for NGC1068, the grains there seem very likely to have grown by coagulation over very long periods of time, so perhaps it is not surprising that, if they ever had any core-mantle character, they no longer do.

As I mentioned in §4.5, further observations of GCIRS 7, GCIRS 3 and new studies of Cyg OB2 #12 are likely to help determine whether core-mantle grains exist in the Galactic diffuse ISM. A further, intriguing, opportunity to test this model in yet another environment may be afforded by the ultraluminous galaxy, IRAS 08572+3915. This galaxy is exceptionally dusty, with a 3.4μm absorption feature several times stronger than that seen in any other line of sight, yet the profile of the feature is almost identical to that seen in Galactic diffuse cloud lines of sight (Wright et al., 1996). The lack of a 3.1μm ice feature in the spectrum of this galaxy also seems to indicate that the dust is predominantly in the galaxy's diffuse medium, with little contamination from dense cloud material. The strength of the 3.4μm band, $\tau \approx 1.0$, means that if an increase in polarisation over the absorption is seen anywhere, it should be detected here. With polarimetric capability now becoming available on 10-m class telescopes, measurements of the polarisation of both the 3.4 and 9.7μm features in IRAS 08572+3915 are now within our reach.

5.3 Summary

To summarise, I have now established that, while dust grains in the centre of the Seyfert II galaxy, NGC1068, may react to environmental factors by increasing in size, the chemical properties of at least one grain component in this galaxy remain startlingly similar to those in many other environments. I have also shown that there are serious difficulties for a widely-used model which attempts to describe dust in the diffuse ISM. I and others have now taken the first tentative steps towards an understanding of the behaviour of dust in the centres of galaxies; what remains is to establish a firm grasp on how the properties of dust are influenced by the properties of the galaxies in which it exists.

Bibliography

Adamson, A. J. and Whittet, D. C. B.: 1990, *A&A* **232**, 27

Adamson, A. J., Whittet, D. C. B., Chrysostomou, A., Hough, J. H., Aitken, D. K., Wright, G. S., and Roche, P. F.: 1999, *ApJ* **512**, 224

Adamson, A. J., Whittet, D. C. B., and Duley, W. W.: 1990, *MNRAS* **243**, 400

Aitken, D. K.: 1989, in *Infrared Spectroscopy in Astronomy*, pp 99–107

Aitken, D. K., Briggs, G., Bailey, J. A., Roche, P. F., and Hough, J. H.: 1984, *Natur* **310**, 660

Aitken, D. K., Briggs, G. P., Roche, P. F., Bailey, J. A., and Hough, J. H.: 1986, *MNRAS* **218**, 363

Aitken, D. K. and Hough, J. H.: 2001, *PASP* **113**, 1300

Aitken, D. K., Smith, C. H., James, S. D., Roche, P. F., and Hough, J. H.: 1988, *MNRAS* **230**, 629

Aitken, D. K., Smith, C. H., Moore, T. J. T., and Roche, P. F.: 1998, *MNRAS* **299**, 743

Aitken, D. K., Smith, C. H., and Roche, P. F.: 1989, *MNRAS* **236**, 919

Allamandola, L. J., Sandford, S. A., Tielens, A. G. G. M., and Herbst, T. M.: 1992, *ApJ* **399**, 134

Alloin, D., Pantin, E., Lagage, P. O., and Granato, G. L.: 2000, *A&AP* **363**, 926

Alonso-Herrero, A., Engelbracht, C. W., Rieke, M. J., Rieke, G. H., and Quillen, A. C.: 2001a, *ApJ* **546**, 952

Alonso-Herrero, A., Quillen, A. C., Simpson, C., Efstathiou, A., and Ward, M. J.: 2001b, *AJ* **121**, 1369

Alpert, N. L., Keiser, W. E., and Szymanski, H. A.: 1973, *IR. Theory and practice of infrared spectroscopy*, New York: Plenum Press, 1973, 2nd ed.

Antonucci, R.: 1993, *ARA&A* **31**, 473

Antonucci, R. R. J. and Miller, J. S.: 1985, *ApJ* **297**, 621

Asano, S. and Yamamoto, G.: 1975, *Appl. Opt.* **14**, 29

Atkins, P. W.: 1994, *Physical Chemistry*, Oxford University Press, 1994, 5th Ed

Bailey, J., Axon, D. J., Hough, J. H., Ward, M. J., McLean, I., and Heathcote, S. R.: 1988, *MNRAS* **234**, 899

Bailey, J., Hough, J. H., and Axon, D. J.: 1984, *MNRAS* **208**, 661

Barford, N. C.: 1967, *Experimental Measurements: Precision, Error and Truth*, Addison-Wesley Publishing Company, Inc.

Barlow, M. J. and Cohen, M.: 1977, *ApJ* **213**, 737

Bianchi, L., Clayton, G. C., Bohlin, R. C., Hutchings, J. B., and Massey, P.: 1996, *ApJ* **471**, 203

Bock, J. J., Neugebauer, G., Matthews, K., Soifer, B. T., Becklin, E. E., Ressler, M., Marsh, K., Werner, M. W., Egami, E., and Blandford, R.: 2000, *AJ* **120**, 2904

Bohren, C. F. and Huffman, D. R.: 1983, *Absorption and scattering of light by small particles*, New York: Wiley, 1983

Bowey, J. E., Adamson, A. J., and Whittet, D. C. B.: 1998, *MNRAS* **298**, 131

Bridger, A., Wright, G. S., and Geballe, T. R.: 1994, in *ASSL Vol. 190: Astronomy with Arrays, The Next Generation*, p. 537

Brooke, T. Y., Sellgren, K., and Geballe, T. R.: 1999, *ApJ* **517**, 883

Brooke, T. Y., Sellgren, K., and Smith, R. G.: 1996, *ApJ* **459**, 209

Calzetti, D., Kinney, A. L., and Storchi-Bergmann, T.: 1994, *ApJ* **429**, 582

Cameron, M., Storey, J. W. V., Rotaciuc, V., Genzel, R., Verstraete, L., Drapatz, S., Siebenmorgen, R., and Lee, T. J.: 1993, *ApJ* **419**, 136

Cardelli, J. A.: 1994, *Science* **265**, 209

Cardelli, J. A., Clayton, G. C., and Mathis, J. S.: 1989, *ApJ* **345**, 245

Cardelli, J. A., Meyer, D. M., Jura, M., and Savage, B. D.: 1996, *ApJ* **467**, 334

Chiar, J. E., Adamson, A. J., Pendleton, Y. J., Whittet, D. C. B., Caldwell, D. A., and Gibb, E. L.: 2002, *ApJ* **570**, 198

Chiar, J. E., Pendleton, Y. J., Geballe, T. R., and Tielens, A. G. G. M.: 1998, *ApJ* **507**, 281

Chlewicki, G. and Greenberg, J. M.: 1990, *ApJ* **365**, 230

Chokshi, A., Tielens, A. G. G. M., and Hollenbach, D.: 1993, *ApJ* **407**, 806

Clayton, G. C. and Martin, P. G.: 1981, *AJ* **86**, 1518

Clough, S. A., Kneizys, F. X., Rothman, L. S., and Gallery, W. O.: 1981, in *Atmospheric transmission; Proceedings of the Meeting, Washington, DC.*, pp 152–166

Comport, A., Pressigout, M., Marchand, E., and Chaumette, F.: 2003, in *IEEE Int. Conf. on Intelligent Robots and Systems*

Crenshaw, D. M., Kraemer, S. B., Bruhweiler, F. C., and Ruiz, J. R.: 2001, *ApJ* **555**, 633

Davies, R. I., Sugai, H., and Ward, M. J.: 1998, *MNRAS* **300**, 388

Davis, L. J. and Greenstein, J. L.: 1951, *ApJ* **114**, 206

Dolan, J. F. and Tapia, S.: 1986, *PASP* **98**, 792

Draine, B.: 1989, in *IAU Symp. 135: Interstellar Dust*, Vol. 135, p. 313

Draine, B. T.: 1985, *ApJS* **57**, 587

Draine, B. T.: 1988, *ApJ* **333**, 848

Draine, B. T.: 1990, in *ASP Conf. Ser. 12: The Evolution of the Interstellar Medium*, pp 193–205

Draine, B. T.: 1995, *Ap&SS* **233**, 111

Draine, B. T. and Flatau, J.: 1994, *J. Opt. Soc Am.* **11**, 1491

Draine, B. T. and Flatau, P. J.: 2000, *User Guide for the Discrete Dipole Approximation Code DDSCAT (Version 5a10)*, astro-ph/0008151v3

Draine, B. T. and Goodman, J.: 1993, *ApJ* **405**, 685

Draine, B. T. and Lee, H. M.: 1984, *ApJ* **285**, 89

Draine, B. T. and Weingartner, J. C.: 1996, *ApJ* **470**, 551

Draine, B. T. and Weingartner, J. C.: 1997, *ApJ* **480**, 633

Dudley, C. C. and Wynn-Williams, C. G.: 1997, *ApJ* **488**, 720

Duley, W. W.: 1984, *QJRAS* **25**, 109

Dyson, J. E. and Williams, D. A.: 1997, *The physics of the interstellar medium*, The physics of the interstellar medium. Edition: 2nd ed. Publisher: Bristol: Institute of Physics Publishing, 1997.

Efstathiou, A., Hough, J. H., and Young, S.: 1995, *MNRAS* **277**, 1134

Ehrenfreund, P., Cami, J., Jiménez-Vicente, J., Foing, B. H., Kaper, L., van der Meer, A., Cox, N., d'Hendecourt, L., Maier, J. P., Salama, F., Sarre, P. J., Snow, T. P., and Sonnentrucker, P.: 2002, *ApJL* **576**, L117

Ehrenfreund, P. and Charnley, S. B.: 2000, *ARAA* **38**, 427

Elvis, M., Marengo, M., and Karovska, M.: 2002, *ApJL* **567**, L107

Frenklach, M. and Feigelson, E. D.: 1989, *ApJ* **341**, 372

Galliano, E., Alloin, D., G., G., and M., V.: 2003, astro-ph/0304293v1

Gallimore, J. F., Baum, S. A., and O'Dea, C. P.: 1996, *ApJ* **464**, 198

Geballe, T. R., Baas, F., and Wade, R.: 1989, *A&A* **208**, 255

Gies, D. R. and Lambert, D. L.: 1992, *ApJ* **387**, 673

Glass, I. S.: 1999, *Handbook of infrared astronomy*, Handbook of infrared astronomy / I.S. Glass. Cambridge ; New York : Cambridge University Press, 1999.

Gordon, K. D. and Clayton, G. C.: 1998, *ApJ* **500**, 816

Goto, M., Gaessler, W., Yutaka, H., Iye, M., Kamata, Y., Kanzawa, T., Kobayashi, N., Minowa, Y., Saint-Jacques, D., Takami, H., Takato, N., and Terada, H.: 2003, astro-ph/0301311

Granato, G. L. and Danese, L.: 1994, *MNRAS* **268**, 235

Greenberg, J. M.: 1978, in *Cosmic Dust*, pp 187–294

Greenberg, J. M.: 1984, *Origins of Life* **14**, 25

Greenberg, J. M. and Li, A.: 1996, *A&A* **309**, 258

Greenberg, J. M., Li, A., Mendoza-Gomez, C. X., Schutte, W. A., Gerakines, P. A., and de Groot, M.: 1995a, *ApJL* **455**, L177

Greenberg, J. M., Li, A., Mendoza-Gomez, C. X., Schutte, W. A., Gerakines, P. A., and de Groot, M.: 1995b, *ApJL* **455**, L177+

Guertler, J., Henning, T., and Dorschner, J.: 1989, *Astronomische Nachrichten* **310**, 319

Gwinn, C. R., Danen, R. M., Tran, T. K., Middleditch, J., and Ozernoy, L. M.: 1991, *ApJL* **381**, L43

Hecht, E. and Zajac, A.: 1974, *Optics*, Addison-Wesley Series in Physics, Reading, Mass.: Addison-Wesley, 1974

Heckman, T. M. and Lehnert, M. D.: 2000, *ApJ* **537**, 690

Henning, T., Il'In, V. B., Krivova, N. A., Michel, B., and Voshchinnikov, N. V.: 1999, *A&AS* **136**, 405

Henry, J. P., Depoy, D. L., and Becklin, E. E.: 1984, *ApJL* **285**, L27

Herbig, G. H.: 1977, in *IAU Symp. 75: Star Formation*, Vol. 75, p. 283

Herbig, G. H.: 1995, *ARA&A* **33**, 19

Hildebrand, R. H.: 2002, in *Astrophysical Spectropolarimetry*, p. 265

Hildebrand, R. H. and Dragovan, M.: 1995, *ApJ* **450**, 663

Horne, K.: 1986, *PASP* **98**, 609

Houck, J. R., Schneider, D. P., Danielson, G. E., Neugebauer, G., Soifer, B. T., Beichman, C. A., and Lonsdale, C. J.: 1985, *ApJL* **290**, L5

Houck, J. R., Soifer, B. T., Neugebauer, G., Beichman, C. A., Aumann, H. H., Clegg, P. E., Gillett, F. C., Habing, H. J., Hauser, M. G., Low, F. J., Miley, G., Rowan-Robinson, M., and Walker, R. G.: 1984, *ApJL* **278**, L63

Hoyle, F. and Wickramasinghe, N. C.: 1984, *From grains to bacteria*, Cardiff : University College Cardiff Press, 1984.

Hoyle, F. and Wickramasinghe, N. C.: 1999a, *Ap&SS* **268**, 249

Hoyle, F. and Wickramasinghe, N. C.: 1999b, *Ap&SS* **268**, 191

Huchra, J. P., Vogeley, M. S., and Geller, M. J.: 1999, *ApJS* **121**, 287

Imanishi, M.: 2000a, *MNRAS* **313**, 165

Imanishi, M.: 2000b, *MNRAS* **319**, 331

Imanishi, M.: 2001, *AJ* **121**, 1927

Imanishi, M. and Dudley, C. C.: 2000, *ApJ* **545**, 701

Imanishi, M., Dudley, C. C., and Maloney, P. R.: 2001, *ApJL* **558**, L93

Imanishi, M., Terada, H., Goto, M., and Maihara, T.: 1998, *PASJ* **50**, 399

Imanishi, M., Terada, H., Sugiyama, K., Motohara, K., Goto, M., and Maihara, T.: 1997, *PASJ* **49**, 69

Imanishi, M. and Ueno, S.: 2000, *ApJ* **535**, 626

Ishii, M., Nagata, T., Chrysostomou, A., and Hough, J. H.: 2002, *AJ* **124**, 2790

Jackson, J. D.: 1975, *Classical Electrodynamics*, New York ; Chichester : Wiley

Jones, A. P., Tielens, A. G. G. M., Hollenbach, D. J., and McKee, C. F.: 1994, *ApJ* **433**, 797

Jura, M.: 1987, in *ASSL Vol. 134: Interstellar Processes*, pp 3–90

Kim, S. and Martin, P. G.: 1994, *ApJ* **431**, 783

Kim, S., Martin, P. G., and Hendry, P. D.: 1994, *ApJ* **422**, 164

Kleinmann, D. E., Gillett, F. C., and Wright, E. L.: 1976, *ApJ* **208**, 42

Knacke, R. F. and Capps, R. W.: 1974, *ApJL* **192**, L19+

Kouchi, A., Kudo, T., Nakano, H., Arakawa, M., Watanabe, N., Sirono, S., Higa, M., and Maeno, N.: 2002, *ApJL* **566**, L121

Krabbe, A., Genzel, R., Eckart, A., Najarro, F., Lutz, D., Cameron, M., Kroker, H., Tacconi-Garman, L. E., Thatte, N., Weitzel, L., Drapatz, S., Geballe, T., Sternberg, A., and Kudritzki, R.: 1995, *ApJL* **447**, L95+

Laor, A. and Draine, B. T.: 1993, *ApJ* **402**, 441

Lazarian, A., Goodman, A. A., and Myers, P. C.: 1997, *ApJ* **490**, 273

Lebofsky, M. J., Kemp, J. C., and Rieke, G. H.: 1978, *ApJ* **222**, 95

Li, A. and Greenberg, J. M.: 1997, *A&A* **323**, 566

Li, A. and Greenberg, J. M.: 2002, *ApJ* **577**, 789

Loska, Z., Czerny, B., and Szczerba, R.: 1993, *Acta Astronomica* **43**, 193

Lumsden, S. L., Moore, T. J. T., Smith, C., Fujiyoshi, T., Bland-Hawthorn, J., and Ward, M. J.: 1999, *MNRAS* **303**, 209

Macchetto, F., Capetti, A., Sparks, W. B., Axon, D. J., and Boksenberg, A.: 1994, *ApJL* **435**, L15

Madau, P., Pozzetti, L., and Dickinson, M.: 1998, *ApJ* **498**, 106

Maiolino, R., Marconi, A., and Oliva, E.: 2001a, *A&A* **365**, 37

Maiolino, R., Marconi, A., Salvati, M., Risaliti, G., Severgnini, P., Oliva, E., La Franca, F., and Vanzi, L.: 2001b, *A&A* **365**, 28

Maiolino, R. and Natta, A.: 2002, *Ap&SS* **281**, 233

Malkan, M. A. and Filippenko, A. V.: 1983, *ApJ* **275**, 477

Maloney, P. R.: 1999, *Ap&SS* **266**, 207

Manners, J.: 2002, *Ph.D. thesis*, University of Edinburgh

Marco, O. and Alloin, D.: 2000, *A&A* **353**, 465

Marco, O. and Brooks, K. J.: 2003, *A&A* **398**, 101

Martin, P. G., Adamson, A. J., Whittet, D. C. B., Hough, J. H., Bailey, J. A., Kim, S.-H., Sato, S., Tamura, M., and Yamashita, T.: 1992, *ApJ* **392**, 691

Martin, P. G. and Whittet, D. C. B.: 1990, *ApJ* **357**, 113

Mathis, J. S.: 1979, *ApJ* **232**, 747

Mathis, J. S.: 1996, *ApJ* **472**, 643

Mathis, J. S., Rumpl, W., and Nordsieck, K. H.: 1977, *ApJ* **217**, 425

Mathis, J. S. and Wallenhorst, S. G.: 1981, *ApJ* **244**, 483

McCarthy, D. W., Low, F. J., Kleinmann, S. G., and Gillett, F. C.: 1982, *ApJL* **257**, L7

McFadzean, A. D., Whittet, D. C. B., Bode, M. F., Adamson, A. J., and Longmore, A. J.: 1989, *MNRAS* **241**, 873

McKee, C.: 1989, in *IAU Symp. 135: Interstellar Dust*, Vol. 135, p. 431

Mennella, V., Brucato, J. R., Colangeli, L., and Palumbo, P.: 2002, *ApJ* **569**, 531

Nagata, T., Kobayashi, N., and Sato, S.: 1994, *ApJL* **423**, L113+

Omont, A., Cox, P., Bertoldi, F., McMahon, R. G., Carilli, C., and Isaak, K. G.: 2001, *A&A* **374**, 371

Origlia, L., Moorwood, A. F. M., and Oliva, E.: 1993, *A&A* **280**, 536

Ossenkopf, V.: 1993, *A&Ap* **280**, 617

Packham, C., Young, S., Hough, J. H., Axon, D. J., and Bailey, J. A.: 1997, *MNRAS* **288**, 375

Padovani, P.: 1989, in F. Giovannelli and G. Mannocchi (eds.), *Vulcano workshop 1988 : frontier objects in astrophysics and particle physics : Vulcano, 23-27 May 1988*, Bologna, Italy : Italian Physical Society.

Pendleton, Y. J.: 1987, *Ph.D. Thesis*

Pendleton, Y. J. and Allamandola, L. J.: 2002, *ApJS* **138**, 75

Pendleton, Y. J., Sandford, S. A., Allamandola, L. J., Tielens, A. G. G. M., and Sellgren, K.: 1994, *ApJ* **437**, 683

Pier, E. A., Antonucci, R., Hurt, T., Kriss, G., and Krolik, J.: 1994, *ApJ* **428**, 124

Popescu, C. C. and Tuffs, R. J.: 2002, *MNRAS* **335**, L41

Priddey, R. S. and McMahon, R. G.: 2001, *MNRAS* **324**, L17

Purcell, E. M. and Pennypacker, C. R.: 1973, *ApJ* **186**, 705

Rawlings, J. M. C.: 1998, in *The Molecular Astrophysics of Stars and Galaxies*, p. 393

Rawlings, M. G., Adamson, A. J., and Whittet, D. C. B.: 2003, astro-ph/0302060

Rieke, G. H.: 1978, *ApJ* **226**, 550

Rieke, G. H. and Lebofsky, M. J.: 1978, *ApJL* **220**, L37

Rieke, G. H. and Low, F. J.: 1972, *ApJL* **176**, L95+

Rieke, G. H. and Low, F. J.: 1975, *ApJL* **199**, L13

Rieke, G. H., Rieke, M. J., and Paul, A. E.: 1989, *ApJ* **336**, 752

Roche, P. F. and Aitken, D. K.: 1985, *MNRAS* **215**, 425

Roche, P. F., Aitken, D. K., Smith, C. H., and Ward, M. J.: 1991, *MNRAS* **248**, 606

Roche, P. F., Whitmore, B., Aitken, D. K., and Phillips, M. M.: 1984, *MNRAS* **207**, 35

Rodrigues, C. V., Magalhaes, A. M., Coyne, G. V., and Piirola, V.: 1997, *ApJ* **485**, 618

Rouan, D., Rigaut, F., Alloin, D., Doyon, R., Lai, O., Crampton, D., Gendron, E., and Arsenault, R.: 1998, *A&A* **339**, 687

Sandford, S. A., Allamandola, L. J., Tielens, A. G. G. M., Sellgren, K., Tapia, M., and Pendleton, Y.: 1991, *ApJ* **371**, 607

Sandford, S. A., Pendleton, Y. J., and Allamandola, L. J.: 1995, *ApJ* **440**, 697

Savage, B. D. and Mathis, J. S.: 1979, *ARA&A* **17**, 73

Schnaiter, M., Henning, T., Mutschke, H., Kohn, B., Ehbrecht, M., and Huisken, F.: 1999, *ApJ* **519**, 687

Scoville, N. Z., Evans, A. S., Thompson, R., Rieke, M., Hines, D. C., Low, F. J., Dinshaw, N., Surace, J. A., and Armus, L.: 2000, *AJ* **119**, 991

Seab, C. G.: 1988, in *Dust in the Universe*, pp 303–326

Seab, C. G. and Shull, J. M.: 1983, *ApJ* **275**, 652

Sellgren, K.: 1984, *ApJ* **277**, 623

Seyfert, C. K.: 1943, *ApJ* **97**, 28

Shore, S. N., Starrfield, S., Gonzalez-Riestra, R., Hauschildt, P. H., and Sonneborn, G.: 1994, *Natur* **369**, 539

Simon, T. and Dyck, H. M.: 1975, *Natur* **253**, 101

Simpson, J. P., Colgan, S. W. J., Erickson, E. F., Hines, D. C., Schultz, A. S. B., and Trammell, S. R.: 2002, *ApJ* **574**, 95

Snow, T. P. and Witt, A. N.: 1996, *ApJL* **468**, L65

Sofia, U. J., Cardelli, J. A., and Savage, B. D.: 1994, *ApJ* **430**, 650

Sofia, U. J. and Meyer, D. M.: 2001, *ApJL* **554**, L221

Soifer, B. T., Neugebauer, G., Matthews, K., Egami, E., Becklin, E. E., Weinberger, A. J., Ressler, M., Werner, M. W., Evans, A. S., Scoville, N. Z., Surace, J. A., and Condon, J. J.: 2000, *AJ* **119**, 509

Sparks, W. B. and Axon, D. J.: 1999, *PASP* **111**, 1298

Speck, A. K., Barlow, M. J., Sylvester, R. J., and Hofmeister, A. M.: 2000, *A&AS* **146**, 437

Spitzer, L. J. and Tukey, J. W.: 1951, *ApJ* **114**, 187

Struve, W.: 1847, *Etudes d'astronomie stellaire.*, St.-Petersbourg, Impr. de l'Academie imperiale des sciences, 1847.

Tacconi, L. J., Genzel, R., Blietz, M., Cameron, M., Harris, A. I., and Madden, S.: 1994, *ApJL* **426**, L77+

Taniguchi, Y. and Murayama, T.: 1998, *ApJL* **501**, L25+

Telesco, C. M., Becklin, E. E., Wynn-Williams, C. G., and Harper, D. A.: 1984, *ApJ* **282**, 427

Thatte, N., Quirrenbach, A., Genzel, R., Maiolino, R., and Tecza, M.: 1997, *ApJ* **490**, 238

Tielens, A. G. G. M., Wooden, D. H., Allamandola, L. J., Bregman, J., and Witteborn, F. C.: 1996, *ApJ* **461**, 210

Tinbergen, J.: 1996, *Astronomical polarimetry*, Cambridge, New York: Cambridge University Press

Tomono, D., Doi, Y., Usuda, T., and Nishimura, T.: 2001, *ApJ* **557**, 637

Trumpler, R. J.: 1930, *PASP* **42**, 214

Wang, J., Heckman, T. M., and Lehnert, M. D.: 1998, *ApJ* **509**, 93

Weingartner, J. C. and Draine, B. T.: 2001, *ApJ* **548**, 296

Weingartner, J. C. and Murray, N.: 2002, *ApJ* **580**, 88

Weisstein, E. W.: 2002, http://mathworld.wolfram.com

Whittet, D. C. B.: 1992, *Dust in the galactic environment*, The Graduate Series in Astronomy, Bristol: Institute of Physics (IOP) Publishing, 1992

Whittet, D. C. B., Adamson, A. J., Duley, W. W., Geballe, T. R., and McFadzean, A. D.: 1989, *MNRAS* **241**, 707

Whittet, D. C. B., Boogert, A. C. A., Gerakines, P. A., Schutte, W., Tielens, A. G. G. M., de Graauw, T., Prusti, T., van Dishoeck, E. F., Wesselius, P. R., and Wright, C. M.: 1997, *ApJ* **490**, 729

Whittet, D. C. B., Gerakines, P. A., Hough, J. H., and Shenoy, S. S.: 2001, *ApJ* **547**, 872

Wickramasinghe, N. C.: 1993, in A. Mampaso, M. Prieto, and F. Sanchez (eds.), *4th Canary Island Winter School of Astrophysics*

Wolff, M. J., Clayton, G. C., and Meade, M. R.: 1993, *ApJ* **403**, 722

Wright, G. S., Bridger, A., Geballe, T. R., and Pendleton, Y.: 1996, in *ASSL Vol. 209: New Extragalactic Perspectives in the New South Africa*

Young, S., Hough, J. H., Axon, D. J., Bailey, J. A., and Ward, M. J.: 1995, *MNRAS* **272**, 513

Young, S., Hough, J. H., Efstathiou, A., Wills, B. J., Bailey, J. A., Ward, M. J., and Axon, D. J.: 1996, *MNRAS* **281**, 1206

Zubko, V. G., Krelowski, J., and Wegner, W.: 1996, *MNRAS* **283**, 577